




8-2020

## **Cracking and Earing Phenomenon in Deep-Drawn Stainless Steel Alloys: Role of Transformation Kinetics, Microstructure, and Texture**

Peijun Hou  
phou1@vols.utk.edu

Follow this and additional works at: [https://trace.tennessee.edu/utk\\_graddiss](https://trace.tennessee.edu/utk_graddiss)

 Part of the [Applied Mechanics Commons](#), [Metallurgy Commons](#), and the [Structural Materials Commons](#)

---

### **Recommended Citation**

Hou, Peijun, "Cracking and Earing Phenomenon in Deep-Drawn Stainless Steel Alloys: Role of Transformation Kinetics, Microstructure, and Texture. " PhD diss., University of Tennessee, 2020.  
[https://trace.tennessee.edu/utk\\_graddiss/6846](https://trace.tennessee.edu/utk_graddiss/6846)

This Dissertation is brought to you for free and open access by the Graduate School at TRACE: Tennessee Research and Creative Exchange. It has been accepted for inclusion in Doctoral Dissertations by an authorized administrator of TRACE: Tennessee Research and Creative Exchange. For more information, please contact [trace@utk.edu](mailto:trace@utk.edu).

To the Graduate Council:

I am submitting herewith a dissertation written by Peijun Hou entitled "Cracking and Earing Phenomenon in Deep-Drawn Stainless Steel Alloys: Role of Transformation Kinetics, Microstructure, and Texture." I have examined the final electronic copy of this dissertation for form and content and recommend that it be accepted in partial fulfillment of the requirements for the degree of Doctor of Philosophy, with a major in Materials Science and Engineering.

Hahn Choo, Major Professor

We have read this dissertation and recommend its acceptance:

Yanfei Gao, Peter K. Liaw, Zhili Feng

Accepted for the Council:

Dixie L. Thompson

Vice Provost and Dean of the Graduate School

(Original signatures are on file with official student records.)

**Cracking and Earing Phenomenon in Deep-Drawn  
Stainless Steel Alloys: Role of Transformation  
Kinetics, Microstructure, and Texture**

A Dissertation Presented for the

Doctor of Philosophy

Degree

The University of Tennessee, Knoxville

Peijun Hou

August 2020

Copyright © 2020 by Peijun Hou.  
All rights reserved.

## **Dedication**

This doctoral dissertation is dedicated to my parents, my beloved wife, and my parents-in-law for their sincere love, encouragement, full support, and unconditional trust in all my pursuits, and all beloved ones who have unconditionally loved and supported me.

## **ACKNOWLEDGEMENTS**

I would like to present my sincere gratitude to all those people who helped and supported me through my Ph.D. study. First and foremost, I would like to give my greatest appreciation to my advisor, Professor Hahn Choo for his continuous academical support of my Ph.D. study and related research, as well as for his guidance on my professional career development. It is a great honor to have him as my advisor, who is knowledgeable and professional, and always providing thought-provoking discussions and suggestions on my works. I would also like to thank my thesis committee members, Professors Yanfei Gao, Peter K. Liaw, and Zhili Feng, for their kind agreement to be on my Doctoral Committee, and their insightful comments and guidance for my dissertation work.

I am glad to work with Dr. Dongchul Chae at POSCO Corp. on this interesting project. I would like to present my great gratitude to Dr. Dongchul Chae for his inspiring guidance on my research. I am thankful to Dr. Ke An at Oak Ridge National Laboratory, and Dr. Yang Ren and Dr. Jun-Sang Park at Argonne National Laboratory for their help and guidance on my research during my Ph.D. study. I would also like to thank our group members, Dr. Ercan Cakmak, Dr. Yi Wang, Dr. Yuan Li, Dr. Kin-Ling Sham, Mr. Rakesh Kamath, Mr. Hyojin Park, and Mr. Logan White. I am grateful to them for their constant help and patience and for the happiness we shared together.

## ABSTRACT

The enhancement of formability of advanced high-strength TRIP-assisted steel alloys is a challenging assignment for industrial application due to the cracking phenomenon. The critical factor governing the cracking behavior is residual-stress concentration resulting from the inhomogeneous plastic deformation and microstructural evolution during the forming processes. Martensitic phase transformation kinetics, constituent phases, and crystallographic texture in TRIP-assisted steel alloys are correlated to the microstructure evolution, resulting in phase-specific stress concentration. In the current study, we are aiming at understanding the fundamental mechanisms responsible for the cracking phenomenon and thus improving the formability of TRIP-assisted steel alloys. Four stainless steel (SS) alloys were used in the current study to provide the variables in stability in austenite phase and constituent phases. There are two main objectives: (1) the constitutive behavior of the SS alloy plates during tensile loading, and to provide a basic understanding of the SS alloy behavior, and (2) the correlation of microstructure and its evolution to the cracking behavior in deep-drawn SS alloy cups and formability of the SS alloys during deep-drawing process.

Firstly, the effect of phase transformation kinetics, constituent phases, and crystallographic texture on the phase-specific stress partitioning and plastic anisotropy was investigated in SS alloy plates subjected to uniaxial tension using synchrotron x-ray diffraction (S-XRD) and in-situ neutron diffraction. Secondly, the correlation of microstructure and its evolution to the cracking phenomenon and

formability of TRIP-assisted steel alloy during deep-drawing process was studied using S-XRD. The results show that the phase-specific stress partitioning behavior is significantly affected by the martensitic phase transformation and constituent phases, resulting in the residual stress concentrating in  $\alpha'$ -martensite responsible for the cracking phenomenon in TRIP steel. However, the residual stresses in  $\alpha'$ -martensite could be reduced in the duplex TRIP steel due to the local stress partitioning between ferrite and  $\alpha'$ -martensite, leading to a better formability in duplex TRIP steel. The textures are correlated to the transformation kinetics, thus influencing the martensite phase fraction and cracking behavior in the TRIP-assisted steel alloys. This study provides the basic idea to improve the formability of high-strength TRIP-assisted steel alloys by manipulating the microstructure to tailor the stress partitioning behavior and plastic anisotropy.



## TABLE OF CONTENTS

Chapter 1 Introduction .....	1
1.1 Background and motivation .....	1
1.2 Key factors influencing the formability of TRIP-assisted steel alloys and scientific issues .....	3
1.2.1 Martensitic phase transformation and constituent phases .....	3
1.2.2 Crystallographic texture .....	4
1.2.3 Objectives .....	5
Chapter 2 Literature Review .....	8
2.1 Alloying and microstructure in stainless steel alloy .....	8
2.1.1 Effect of alloying elements on microstructure .....	8
2.1.2 Effect of temperature on phase balance .....	14
2.2 Martensitic Phase Transformation .....	19
2.2.1 Mechanism of the martensitic phase transformation .....	19
2.2.2 Orientation relationship .....	31
2.2.3 Stacking fault energy .....	33
2.2.4 Factors affecting the martensitic phase transformation .....	35
2.2.5 Effect of $\alpha'$ martensite on mechanical properties .....	40
2.3 Crystallographic texture .....	43
2.3.1 Rolling texture in face centered cubic (FCC) metals .....	45
2.3.2 Rolling texture in body centered cubic (BCC) metals .....	46
2.3.3 Fiber texture .....	46
2.3.4 Factors influencing texture development .....	48
2.4 Deep drawing and the formability of high-strength steel alloy .....	49

Chapter 3 Effects of Phase Transformation Kinetics, Constituent Phases, Crystallographic Texture on Phase-Specific Tensile Stress Partitioning In Alloy Plates.....	51
3.1 Introduction .....	51
3.2 Experimental .....	55
3.2.1 Alloy design and processing .....	55
3.2.2 Microstructure and tensile behavior of alloy plates .....	57
3.2.3 Phase fraction and texture measurements using S-XRD.....	57
3.2.4 Lattice strain measurements using in-situ ND tensile testing.....	58
3.3 Results .....	60
3.3.1 Microstructure and constituent phases .....	60
3.3.2 Tensile behavior of alloy plates.....	63
3.3.3 Martensitic phase transformation .....	66
3.3.4 Texture evolution .....	68
3.3.4 Lattice strain and residual-lattice strain evolutions.....	76
3.4 Discussion .....	83
3.4.1 Stress partitioning and its effect on the residual-stress concentration	83
3.4.2 Texture evolution and its effect on the martensitic phase transformation and plastic anisotropy .....	93
3.5 Conclusions.....	98
Chapter 4 Phase-Specific Residual Stress Partitioning and Cracking Behavior In Deep-Drawn Alloy Cups.....	101
4.1 Introduction .....	101
4.2 Experimental .....	107

4.2.1 Deep-drawing process .....	107
4.2.2 Phase fraction, texture, and microscopic residual stress measurements in deep-drawn SS cups using S-XRD .....	108
4.3 Results .....	111
4.3.1 Cracking behavior in deep-drawn stainless steel alloys .....	111
4.3.2 Constituent phases and strain-induced $\alpha'$ -martensite phase fraction in the deep-drawn stainless steel alloys .....	113
4.3.3 Textures in the deep-drawn stainless steel cups .....	117
4.3.4 Microscopic residual stresses in deep-drawn stainless steel cups ...	124
4.4 Discussion .....	129
4.4.1 Effect of martensitic phase transformation and constituent phases on phase-specific stress concentration in deep-drawn stainless steel alloys..	129
4.4.2 Texture evolution and its effect on the martensitic phase transformation and plastic anisotropy in deep-drawn stainless steel alloys .....	134
4.5 Conclusions.....	140
Chapter 5 Summary and Conclusions .....	144
List of References .....	148
Vita.....	165

## LIST OF TABLES

- Table 3.1. Chemical compositions (wt.%) of stainless steel alloys manufactured for the current study. The TRIP SS (TRIP) consists of an initially single-phase metastable austenitic SS that will go through martensitic phase transformation with applied strain. The austenitic SS (A-SS) is a stable counterpart to the TRIP alloy. The lean duplex TRIP SS (D-TRIP) consists of metastable austenite and ferrite phases, where the austenite phase will provide the TRIP effect. Finally, the lean duplex SS (D-SS) is a stable counterpart of the D-TRIP alloy. 56
- Table 3.2. Tensile properties and Lanford coefficients:  $E$  is the Young's modulus,  $\sigma_y$  is the 0.2% proof stress,  $UTS$  is the tensile strength,  $\epsilon_u$  is the total elongation, and  $\epsilon_t$  is the total elongation. 65
- Table 3.3. Ideal components of FCC and BCC textures with their orientation relations with respect to the sample axes. The plane normal of  $\{hkl\}$  is parallel to the normal direction (ND), and the  $\langle uvw \rangle$  is parallel to the rolling direction (RD) of the alloy plate. 69
- Table 3.4. Diffraction moduli,  $E_{311}$  for austenite and  $E_{211}$  for ferrite, and Poisson's ratios,  $\nu_{311}$  for austenite and  $\nu_{211}$  for ferrite, following the Kröner model. 90
- Table 4.1. The formability of SS alloys examined using deep-drawing process as a function of drawing ratio at ambient temperature in terms of cracking phenomenon. 112

Table 4.2. Ideal components of fcc texture with their orientations relations with respect to the sample axes. The plane normal of  $\{hkl\}$  is parallel to the normal direction (ND), and the  $\langle uvw \rangle$  is parallel to the rolling direction (RD) of the alloy plate.

121

## LIST OF FIGURES

Figure 2.1 Concentration profiles in the ternary Fe-Cr-Ni constitution diagram at 70% and 60% Fe [43]. .....	11
Figure 2.2 Observation summary of carbides, ferrite, and sigma in Type 316 steel [60]......	15
Figure 2.3 TTT diagrams of duplex stainless steels derived by optical metallography between 600 and 1050°C and hardness measurements between 300 and 600°C. ....	17
Figure 2.4 Schematic representation of a martensite nucleus [63]. ....	21
Figure 2.5 Zener's model of the generation of two-atom-thick martensite by a half-twinning shear [63]......	23
Figure 2.6 Venables' model for the $\gamma \rightarrow \varepsilon' \rightarrow \alpha'$ transformation in stainless steel. ....	24
Figure 2.7 Dislocation-assisted martensite transformation in a physically deformed 17%Cr-8%Ni stainless steel [63]......	25
Figure 2.8 Mn-Cr-Ni steel quenched to 196°C showing a number of large $\varepsilon$ -bands (B) containing $\alpha$ -martensite laths. The positions of these laths are indicated by the large arrows and projected width of the $\alpha$ -martensite habit plane interface is visible at A [68]. ....	27
Figure 2.9 Schematic model for bcc structure formation from an hcp structure [63]. ....	28

Figure 2.10 Characteristic pole figures after 10% strain at $T = -60\text{ }^{\circ}\text{C}$ and corresponding to: (a) experimental $\gamma$ grain orientations belonging to the Cube component $\{1\ 0\ 0\}\langle 1\ 0\ 0\rangle$ , (b) experimental $\alpha'$ martensitic orientations formed in those $\gamma$ grains, (c) $\alpha'$ martensitic orientations simulated without variant selection from those $\gamma$ grains, (d) $\alpha'$ martensitic orientations simulated with variant selection from those $\gamma$ grains. ....	39
Figure 3.1. Optical micrographs of (a) TRIP, (b) A-SS, (c) D-TRIP, and (d) D-SS alloys on the RD-TD surface. 3D optical micrographs of the RD, TD, and ND surfaces of (e) TRIP, (f) A-SS, (g) D-TRIP and (h) D-SS alloys. ....	61
Figure 3.2. Neutron diffraction patterns of as-rolled plates measured with the scattering vector along RD for: (a) TRIP, (b) A-SS, (c) D-TRIP, and (d) D-SS. ....	62
Figure 3.3. Tensile stress-strain curves of (a) TRIP, (b) A-SS, (c) D-TRIP, and (d) D-SS alloys measured as a function of the LD with respect to RD. (e) A comparison between tensile stress-strain curves of all four alloys with the LD parallel to RD. (f) R-values as a function of the angle with respect to RD for all four alloys. ....	64
Figure 3.4. Evolution of strain-induced HCP $\epsilon$ - and BCC $\alpha'$ -martensite phase fractions in TRIP D- TRIP alloys measured as a function of the applied strain at three different LDs. ....	67
Figure 3.5. Two orientation distribution function (ODF) sections ( $\varphi_2 = 0^{\circ}$ ) and ( $\varphi_2 = 45^{\circ}$ ) showing the initial texture of the austenite phase in the as-rolled plates of (a) TRIP, (b) A-SS, (c) D-TRIP, and (d) D-SS alloys. ....	70

Figure 3.6. (111), (220), and (200) pole figures (PFs) of the FCC austenite phase in the as-received and tensile samples deformed (26% engineering strain) along three different LDs in (a) TRIP, (b) A-SS, (c) D-TRIP, and (d) D-SS alloys.....	71
Figure 3.7. An ODF section ( $\varphi_2 = 45^\circ$ ) showing the initial texture of the ferrite phase in the as-received plates of (a) D-TRIP and (b) D-SS alloys. ....	72
Figure 3.8. (222), (110), and (200) PFs of the BCC phases in the as-received and tensile samples deformed (26% engineering strain) along three different LDs. (a) Ferrite and $\alpha'$ -martensite phases in D-TRIP, and (b) ferrite phase in D-SS. ....	74
Figure 3.9. (222), (110), and (200) PFs of the strain-induced $\alpha'$ -martensite phase in TRIP alloy deformed (26% engineering strain) along three different LDs.	75
Figure 3.10. Evolutions of elastic lattice strain and residual lattice strain of (111), (200), (220), and (311) in FCC phase and (110), (200), and (211) in BCC phases measured using in-situ neutron diffraction. Elastic lattice strains as a function of the applied stress. Austenite phase in (a) TRIP and A-SS, (c) D-TRIP and D-SS, and (d) ferrite and $\alpha'$ -martensite phases in D-TRIP and ferrite phase D-SS. Residual lattice strains as a function of the strain. Austenite phase in (b) TRIP and A-SS, (e) D-TRIP and D-SS, and (f) ferrite and $\alpha'$ -martensite phases in D-TRIP and ferrite phase D-SS. ....	77
Figure 3.11. Evolutions of elastic lattice strain and residual lattice strain of (111), (200), (220), and (311) in FCC phase and (110), (200), and (211) in BCC phases measured using in-situ neutron diffraction. Elastic lattice strains as a	



function of the applied stress. Austenite phase in (a) TRIP and A-SS, (c) D-TRIP and D-SS, and (d) ferrite and $\alpha'$ -martensite phases in D-TRIP and ferrite phase D-SS. Residual lattice strains as a function of the strain. Austenite phase in (b) TRIP and A-SS, (e) D-TRIP and D-SS, and (f) ferrite and $\alpha'$ -martensite phases in D-TRIP and ferrite phase D-SS. ....	79
Figure 3.12. The evolutions of interplanar distance, e.g. $d_{011}$ of strain-induced $\varepsilon$ -martensite phase and $d_{211}$ of strain-induced $\alpha'$ -martensite phase in TRIP alloy, as a function of applied stress. ....	84
Figure 3.13. Evolutions of phase-specific residual stress measured using in-situ neutron diffraction. (a) residual stress evolutions of the austenite and $\alpha'$ -martensite phases as a function of the applied strain in TRIP and A-SS alloys, and (b) residual stress evolutions of the austenite, ferrite, and $\alpha'$ -martensite phases as a function of the applied strain in D-TRIP and D-SS.....	92
Figure 3.14. ODF section ( $\varphi_2 = 45^\circ$ ) showing (a) the Taylor factors of oriented grains in BCC crystals based on the octahedral slip, i.e. $\{110\}\langle 111 \rangle$ slip system, and the initial texture of the ferrite phase with the normal of $\{hkl\}$ and the $\langle uvw \rangle$ of the lattice plane parallel to the normal direction (ND) and LD in D-SS. (b) LD parallel to RD, (c) to $45^\circ$ with respect with RD, and (d) to TD. ....	97
Figure 4.1. Images of deep-drawn TRIP and D-TRIP alloys at DR=2.1, showing the cracking phenomenon in deep-drawn TRIP alloy. ....	104
Figure 4.2. Tensile stress-strain curves of TRIP and D-TRIP alloy with the loading direction parallel to RD.....	104

Figure 4.3. The schematics of the transmission geometry setup at 1-ID-C, APS, ANL and area mapped in deep-drawn SS cups for hoop and axial residual stress measurements using S-XRD.....	110
Figure 4.4. Evolution of selected crack length located at deep-drawn TRIP alloy at DR = 2.1 with respect to RD as a function of the incubation time after deep-drawing process.....	112
Figure 4.5. Synchrotron x-ray diffraction patterns measured at the outside surface of tip of deep-drawn SS cups wall (DR =2.0): (a) TRIP, (b) A-SS, (c) D-TRIP, and (d) D-SS.....	114
Figure 4.6. Evolutions of strain-induced $\alpha'$ -martensite phase fraction measured at the outside surface of tip of deep-drawn TRIP and D-TRIP cups wall (DR = 2.0) using S-XRD as a function of orientation with respect to RD.....	116
Figure 4.7. (111), (220), and (200) pole figures of fcc austenite phase measured at the outside surface of tip of deep-drawn SS cups wall (DR = 2.0) using S-XRD as a function of orientation with respect to RD: (a) TRIP, (b) A-SS, (c) D-TRIP, and (d) D-SS. Ideal components of fcc texture with their orientation relations with respect to the alloy plate axes. The plane normal of {hkl} is parallel to the normal direction (ND), and the $\langle uvw \rangle$ is parallel to the rolling direction (RD) of the alloy plate.....	118
Figure 4.8. (222), (110), and (200) pole figures of the strain-induced $\alpha'$ -martensite phase measured at the outside surface of tip of deep-drawn TRIP cup wall (DR = 2.0) using S-XRD as a function of orientation with respect to RD. ..	119

Figure 4.9. (222), (110), and (200) pole figures of bcc phases (ferrite phase and strain-induced  $\alpha'$ -martensite phase in D-TRIP; ferrite phase in D-SS) measured at the outside surface of tip of deep-drawn SS cup wall (DR = 2.0) using S-XRD as a function of orientation with respect to RD: (a) D-TRIP and (b) D-SS.....120

Figure 4.10. Evolutions of phase-specific hoop residual stress measured using S-XRD. (a) Hoop residual stress evolutions of the austenite and strain-induced  $\alpha'$ -martensite phases as a function of deep-drawn cup wall height and thickness in deep-drawn TRIP alloy, (b) hoop residual stress evolutions of the austenite phase as a function of deep-drawn cup wall height and thickness in deep-drawn A-SS alloy, (c) hoop residual stress evolutions of the austenite phase and bcc phases consisting of ferrite and strain-induced  $\alpha'$ -martensite phases as a function of deep-drawn cup wall height and thickness in deep-drawn D-TRIP alloy, and (d) hoop residual stress evolutions of the austenite and ferrite phases as a function of deep-drawn cup wall height and thickness in deep-drawn D-SS alloy. ....125

Figure 4.11. Evolutions of phase-specific axial residual stress measured using S-XRD. (a) Axial residual stress evolutions of the austenite and strain-induced  $\alpha'$ -martensite phases as a function of deep-drawn cup wall height and thickness in deep-drawn TRIP alloy, (b) axial residual stress evolutions of the austenite phase as a function of deep-drawn cup wall height and thickness in deep-drawn A-SS alloy, (c) axial residual stress evolutions of the austenite phase and bcc phases consisting of ferrite and strain-induced  $\alpha'$ -martensite

phases as a function of deep-drawn cup wall height and thickness in deep-drawn D-TRIP alloy, and (d) axial residual stress evolutions of the austenite and ferrite phases as a function of deep-drawn cup wall height and thickness in deep-drawn D-SS alloy. ....	126
Figure 4.12. Inverse pole figures along the hoop direction in deep-drawn TRIP alloy (DR = 2.0) showing the deformation textures in the strain-induced $\alpha'$ -martensite phase and the austenite phase. ....	136
Figure 4.13. A comparison between the strain-induced $\alpha'$ -martensite phase fraction measured in deep-drawn TRIP and D-TRIP alloys and the initial (200) texture intensity in austenite phase in the as-received TRIP and D-TRIP alloy plates. ....	138

## **CHAPTER 1 Introduction**

### **1.1 Background and motivation**

It is well known that the initiation of strain localization is critical to the analysis of formability of sheet metal alloys during sheet-metal forming processes [1-3]. The strain generated during the heterogeneous sheet-metal forming processing localizes into the deformation bands [4, 5]. When the localized strain reaches a critical value, i.e. the limit strain, during a forming process, cracks can be generated, worsening the formability of metal alloys. Thus, according to the limit strain in sheet-metal forming processes, the forming limit curve has been developed as a strain-based failure criterion to evaluate the formability of sheet metal alloys [6-11]. Mechanistic works have been extensively reported to study the formability of sheet metals regarding the forming limit curve, showing that the limit strain is strongly correlated to the strain rate and strain-hardening rate as well as uniform elongation, and it could be effectively improved by increasing the strain-hardening rate, leading to the delayed onset of necking [12-14]. The approach for enhancing the formability of sheet metals has been employed through improving the strain-hardening rate in a number of studies on alloy design. For example, Srivastava et al. [15] used an optimal heat treatment on the transformation-induced plasticity (TRIP) steel alloy to enhance the strain-hardening rate, showing that the heat-treated steel sample exhibits high tensile elongation, high limit strain, and thus good formability.

The TRIP-assisted steel alloys as a third-generation advanced high-strength steel alloy have been developed based on the strain-based failure criterion to meet the requirement of improvement in formability for broad structural applications [16-19]. As the martensitic phase transformation results in the increase in the strain-hardening rate during plastic deformation, the onset of necking is delayed and thereby the tensile elongation and strength are enhanced. However, it has also been reported that the TRIP steel alloys frequently present a cracking phenomenon during the sheet-metal forming process at ambient temperature, despite its high tensile elongation [20-22]. In general, the inhomogeneous plastic deformation generated from the sheet-metal forming process can lead to the changes in microstructure, which, in turn, can cause microscopic strain or stress localization, resulting in cracking. In the literature [23, 24], it has been acknowledged that the cracking phenomenon in TRIP steel alloys observed during sheet-metal forming process is strongly correlated to the microstructure and its evolution. Therefore, the strain-based failure criterion considering the limit strain is not sufficient to understand the underlying mechanism responsible for the formability of TRIP or TRIP-assisted steel alloys. Detailed metallurgical investigation on the microstructure-processing relationship is necessary and the experimental results would provide a fundamental understanding of the formability and thereby enhancing the broad application of the advanced high-strength TRIP alloys.

## **1.2 Key factors influencing the formability of TRIP-assisted steel alloys and scientific issues**

### ***1.2.1 Martensitic phase transformation and constituent phases***

Martensitic phase transformation in TRIP-assisted steel alloys consisting of metastable austenite phase is promoted during plastic deformation, resulting in the transformation of metastable austenite phase into the strain-induced hcp  $\epsilon$ - and/or bcc/bct  $\alpha'$ -martensite phases [16, 25]. In the TRIP-assisted steel alloys, the phase-specific stress partitioning is expected to occur during plastic deformation because of the difference in the phase-specific mechanical properties. As a result, the residual stress concentration could be generated from the stress partitioning between constituent phases when the applied stress is unloaded. Furthermore, the changes in the stress or strain in metastable austenite phase caused by the phase-specific stress partitioning, in turn, could affect the martensitic phase transformation kinetics [26].

Prior works are mostly focused on the effect of martensitic phase transformation on the hydrogen embrittlement associated with macroscopic residual stress concentration [27-30]. It is due to the fact that the martensitic phase transformation resulting in the bcc/bct  $\alpha'$ -martensite phase provides a diffusion path for hydrogen atoms because of the higher hydrogen releasing rate in bcc/bct structure and thereby facilitates the hydrogen embrittlement [31, 32]. However, it has been reported that the cracking phenomenon is not suppressed accordingly in TRIP-assisted steel alloy processed by the deep-drawing process when the content of

hydrogen is extremely limited [33, 34]. Therefore, the hydrogen embrittlement is not supposed to be the only key factor for cracking problem and formability of TRIP-assisted steel alloy.

Furthermore, in a recent study on the formability of a lean duplex TRIP steel alloy consisting of metastable austenite phase and ferrite phase, the macroscopic residual stress measured using the split ring test showed a reduction in the stress in the lean duplex TRIP steel alloy as compared to its TRIP counterpart processed using the deep-drawing operation at an identical drawing ratio [34]. It suggests that the change in constituent phases is significantly correlated to the improvement in formability of TRIP-assisted steel alloys. The ferrite phase interplaying with metastable austenite phase and strain-induced martensite phases could contribute to the phase-specific stress partitioning and thus influence on the phase-specific residual stress concentration [35, 36]. As described earlier, varying the stress partitioning between constituent phases also could result in the change in stress in austenite phase and thereby martensitic phase transformation kinetics.

### ***1.2.2 Crystallographic texture***

In general, the amount of strain-induced martensite phase affects the mechanical properties of TRIP-assisted steel alloys as well as the failure mechanism [20]. Also, the phase-specific stress portioning behavior is correlated to the strain-induced martensite phase fraction controlled by the martensitic phase transformation kinetics due to the changes in the proportion of constituent phases. It is well known that the change in martensitic phase transformation kinetics following



crystallographic variant selection is controlled by the texture in austenite phase, thus resulting in the different amount of strain-induced martensite phase [16, 19, 37].

Furthermore, the crystallographic texture plays an important role in the plastic anisotropy, which could further the heterogeneous plastic deformation during sheet-metal forming process. Also, the development of textures in constituent phases is generally influenced by the constraint effect between phases and phase transformation owing to the orientation relationship and the selective phase transformation mechanism [37]. Therefore, the plastic anisotropy is generated not only from the crystallographic texture but also from the phase transformation kinetics. Subsequently, the macroscopic stress localization, caused by the heterogeneous plastic deformation due to plastic anisotropy, could be associated with the phase-specific stress concentration, resulting in cracking and worsening of the formability.

### ***1.2.3 Objectives***

In the current study, we are aiming at investigating the correlation of the microstructure and its evolution to the cracking phenomenon and formability of TRIP-assisted steel alloys. The complicated interplay of martensitic phase transformation kinetics, constituent phases, and crystallographic texture is studied and connected to the phase-specific stress partitioning behavior as well as the phase-specific residual stress concentration, which is considered as the key factor contributing on the cracking phenomenon. Four stainless steel (SS) alloys were

used in this study to provide the variables in stability in austenite phase and constituent phases, i.e. (1) a TRIP SS, (2) a stable austenitic SS (stable counterpart of (1)), (3) a lean duplex TRIP SS, and (4) a lean duplex stable SS (stable counterpart of (3)).

The main objectives are as follows:

1. On the effects of microstructure, including transformation kinetics, constituent phases, and crystallographic texture, on phase-specific tensile stress partitioning in SS alloy plates:

(1) To study the macroscopic tensile behaviors and plastic anisotropy of all SS alloys using uniaxial tension at ambient temperature.

(2) To analyze the lattice strain evolution to study the micromechanical tensile behavior and phase-specific stress partitioning during uniaxial tension, and understand the effect of martensitic phase transformation and constituent phases on this phase-specific stress partitioning behavior and thereby on the phase-specific residual stress concentration.

(3) To understand the effect of crystallographic texture and its evolution on plastic anisotropy and martensitic phase transformation kinetics, and to investigate the correlation of plastic anisotropy and martensitic phase transformation kinetics to the phase-specific residual stress concentration in alloy plates.

2. On the phase-specific residual stress partitioning and cracking behavior in deep-drawn SS alloy cups

(1) To study the formability of all SS alloys using deep-drawing process at ambient temperature.

(2) To analyze the distribution of strain-induced martensite phase fraction and texture developed in the deep-drawn SS alloy cups, and to correlate them to the phase-specific residual stresses generated in the deep-drawn SS alloy cups.

(3) To understand the effect of martensitic phase transformation kinetics, constituent phases, and texture on the phase-specific residual stress partitioning behavior in deep-drawn SS alloy cups.

The current study provides a basic understanding of underlying mechanisms responsible for cracking phenomenon and formability in TRIP-assisted steel alloys during sheet-metal forming processes. Therefore, this work could further enhance the possibilities to improve the formability of high-strength TRIP-assisted steel alloys and facilitate their broad industry applications.

## **CHAPTER 2 Literature Review**

### **2.1 Alloying and microstructure in stainless steel alloy**

#### ***2.1.1 Effect of alloying elements on microstructure***

Stainless steel alloys are the most extensively used structural materials based on the development of iron-chromium (Fe-Cr) alloy system. Ferrite, austenite, and martensite are primary microstructures in stainless steel alloys. The austenitic stainless steel can be generated using the austenite stabilizers, such as Ni, C, and N. Moreover, the stainless steel alloys always contain at least 10.5 wt.% Cr to improve the corrosion resistance through forming a thin film consisting of chromium oxide. There has been extensive efforts to develop the austenitic stainless steel alloys for the requirements of high strength and good ductility in steel alloys using optimal heat treatment process and alloying elements. For example, the transformation-induced plasticity (TRIP) stainless steel alloys have been developed by introducing Mn and lowering Ni as the stacking fault energy decreases. In general, TRIP stainless steel alloys exhibit high strength and good ductility due to the strain-induced martensite phase generated from martensitic phase transformation prevents dislocation movement and delays the onset of necking. Therefore, TRIP stainless steel alloys associated with high-energy absorption become the good candidate in sheet-metal forming process for the application of automotive industry.

Another important modern stainless steel alloy is duplex stainless steel alloy consisting of austenite phase and ferrite phase. This alloy shows a good

mechanical properties and corrosion resistance due to the combinational benefits of austenite phase and ferrite phase. Therefore, the increase attention has been paid on the development of duplex stainless steel alloys by balancing the alloying elements for broad structural applications. For example, the lean duplex TRIP stainless steel alloys have been developed to reduce the cost of austenitic stainless steel alloy using cheaper alloying elements instead of expensive Ni. It has been reported that the lean duplex TRIP stainless steel alloy is a good candidate to replace some austenitic stainless steel alloys, such as 304L and 304L austenitic stainless steel alloys, because of its comparable mechanical properties and lower price as compared to austenitic stainless steel alloys.

In general, the equilibrium phase diagram based on the ternary Cr-Fe-Ni system is mostly used as a criterion to design the phase and microstructure in stainless steel alloys [38, 39]. However, other alloying elements, such as C, N, Mn, Mo, Si, Cu, etc., are usually involved in stainless steel alloys and contribute on the development of phase and microstructure [40]. To identify the effect of other alloying elements on the phase and microstructure, empirical equations, based on nickel and chromium equivalents, have been developed, in Equation 2.1 and accordingly the Cr-Fe-Ni equilibrium diagram has been created, as shown in Figure 2.1 [41, 42].

$$\begin{aligned}
 \text{Ni equivalent (wt. \%)} = \%Ni + \%Co + 0.5\%Mn + 30\%C \\
 + 0.3\%Cu + 25\%N
 \end{aligned}
 \tag{2.1}$$

$$\begin{aligned}
 Cr \text{ equivalent (wt. \%)} = \%Cr + 2.0\%Si + 1.5\%Mo + 5\%V + 5.5\%Al \\
 + 1.75\%Nb + 1.5\%Ti + 0.75\%W
 \end{aligned}
 \tag{2.2}$$

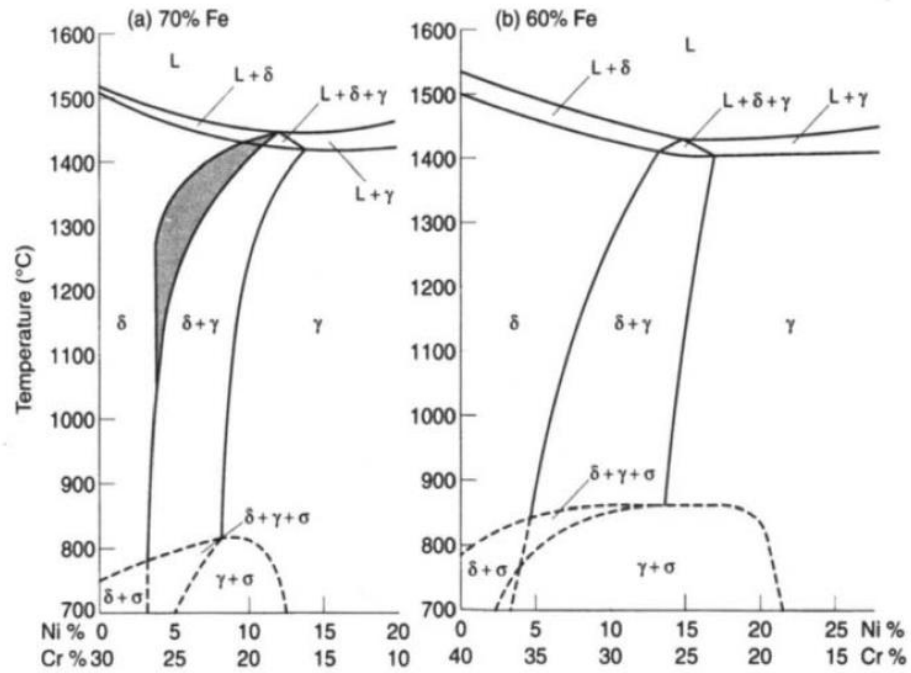


Figure 2.1 Concentration profiles in the ternary Fe-Cr-Ni constitution diagram at 70% and 60% Fe [43].

In the view of the Cr-Fe-Ni equilibrium diagram and the formulae of those two equivalent numbers, those alloying additions act as different roles for phase balancing in stainless steels. The main reason, as mentioned above, of adding Cr to steel is to form a passive oxy-hydroxide film with the concentration of Cr for a good resistance to general corrosion. Usually, the content of Cr in stainless steel is in the range of 16 wt.% to 26 wt.% since the formation of intermetallic phase, such as sigma phase (FeCr), is enhanced by higher level of Cr [44]. This intermetallic phase is harmful for mechanical properties by reducing the ductility and corrosion resistance. In addition, Cr is a stabilizer for ferrite phase ( $\alpha$ - $\delta$  Fe), but not for austenite phase ( $\gamma$  Fe) as Cr dissolves to bcc iron as all proportions to form a stable bcc solid solution [45].

As opposite role of Cr for stabilizing ferrite, Ni is to prefer to dissolve in fcc iron, so that Ni is a main element to maintain the austenite phase. For instance, 316L austenitic stainless steel contains 10.0 to 12.0 wt.% to balance the effect of Cr on phase for maintaining the fully austenite phase [46]. While in order to maintain a comparable amount of ferrite phase, for example, 5.5 to 8.5 wt.% of Ni need to be added in the S32404 lean duplex stainless steel, which is composed of austenite and ferrite [47]. Moreover, excessive content of Ni in stainless steels leads to the enrichment of Cr and Mo in ferrite phase, therefore enhancing the formation of brittle intermetallic compound, such as sigma phase [48].

To improve the pitting and corrosion resistance of stainless steel with respect to chloride solutions, Mo needs to be added in stainless steels [49]. From the Eq. 2.2,



it can be found that Mo has a similar effect on ferrite stability as Cr. The range of addition of Mo is between 3.0 wt.% to about 4.0 wt.%. Higher level of Mo can promote the formation of sigma phase during hot working (above 1000 °C) and the reduction of the solid solubility of carbon to enhance the precipitation of carbide [47].

The effect of Mn on phase stability is still in conflict [50]. In most cases of stainless steels, Mn is treated as an austenite stabilizer, as shown in Eq. 2.1, while there have been some evidences that Mn enhances the formation and stability of ferrite [51]. However, Hull et al. [52] proposed that the influence of Mn on phase stability varies as its content. In high content of Mn, it behaves as ferrite stabilizer, while in low content of Mn, it tends to stabilize austenite phase. Nevertheless, the effect of Mn is little on balancing phase, as studied by Onozuka et al. [53]. The advantage of Mn addition is to improve wear and pitting resistance and tensile properties since the solid solubility of N is increased by adding Mn [43].

C and N are austenite stabilizer and encourage the formation of austenite [40]. The introduction of C and N also strengthens austenite and ferrite due to solid solution strengthening by dissolving C and N atoms at interstitial sites [54]. The content of C may contain up to 0.15 wt.% and 0.03 wt.% in austenitic stainless steels and duplex stainless steels, respectively. The limitations are considered to prevent the formation of carbide precipitations, such as  $M_{23}C_6$  and  $M_7C_3$ , which reduce the intergranular corrosion resistance and ductility by acting as initiation sites of cracking [55]. On the other hand, by introducing N, the improvement of pitting and

corrosion resistances is achieved [56]. Furthermore, N is good at suppressing the formation of intermetallic phases in stainless steels by reducing the segregation of Cr. Despite this, much N can enhance the nitride precipitation, such as  $\text{Cr}_2\text{N}$ . For instance, the content of N in 300 series grade austenitic stainless steels is less than 0.15 wt.% [43].

Silicon (Si) is beneficial for pitting and stress corrosion resistances, but if it is added more than 1.0 wt.%, it is deleterious due to enhance sigma phase formation [57, 58]. The addition of Cu also improves corrosion resistance, while higher content of Cu can lead to the reduction of ductility by forming Cu-rich precipitation [59].

### ***2.1.2 Effect of temperature on phase balance***

The microstructure of a stainless steel, beside the influence of chemical composition, is also controlled by the annealing temperature. Hence, wrought austenitic and duplex stainless steels usually are subjected to isothermal or anisothermal resolution heat treatment to optimize the following microstructure. For instance, the effects of annealing temperature (600 °C to 850 °C) and time (upon 900 hours) on microstructure in 316 austenitic stainless steel were investigated by White and Le May [60]. The results are summarized in Figure 2.2. They proposed that carbide formation was promoted in relative low temperature and preceded the formation of ferrite and sigma. At the temperature range between 600 °C and 850 °C with annealing for 900 hours, the ferrite became stable. Additionally, the single austenite phase was obtained when the annealing

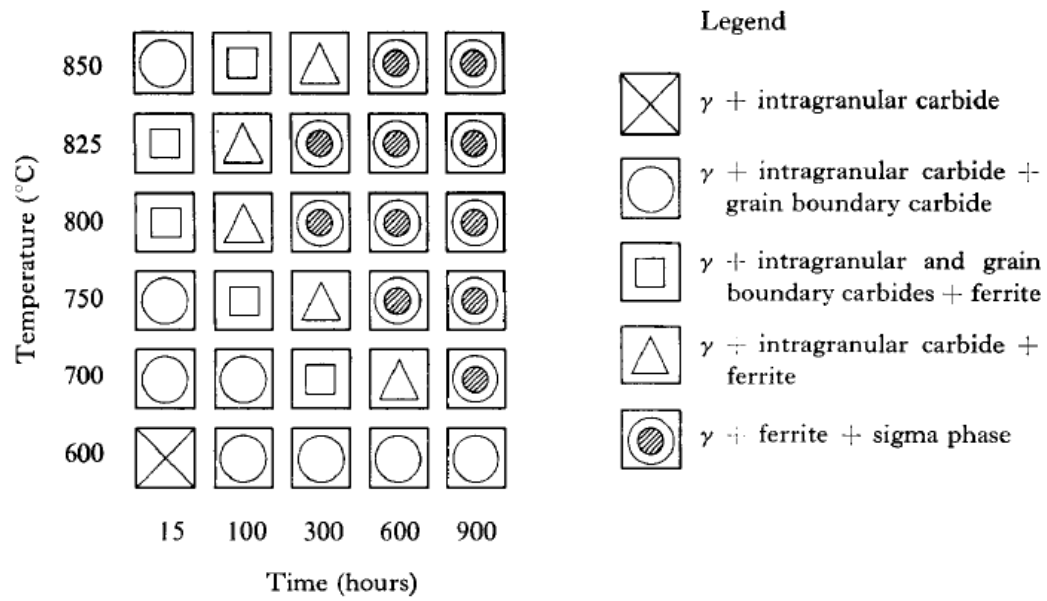


Figure 2.2 Observation summary of carbides, ferrite, and sigma in Type 316 steel [60].

temperature upon 950 °C for at last 350 hours. And the sigma phase was encouraged to form in the temperature range of 750 °C to 850 °C. Figure 2.3 presents a time-temperature transformation (TTT) diagram of variant duplex stainless steels as a function of the annealing temperature range from 0 °C to 1050 °C associated with time variation of 0 to 100 hours [43]. As shown in Figure 2.3, different duplex stainless steels classified by different mechanical properties can be predicted through the controls of temperature and time for annealing. For instance, to prevent the formation of intermetallic phase in S32304 duplex stainless steel, it required a solution annealing temperature of 1000 °C because the precipitation is observed at temperature below 900 °C for 10 hours.

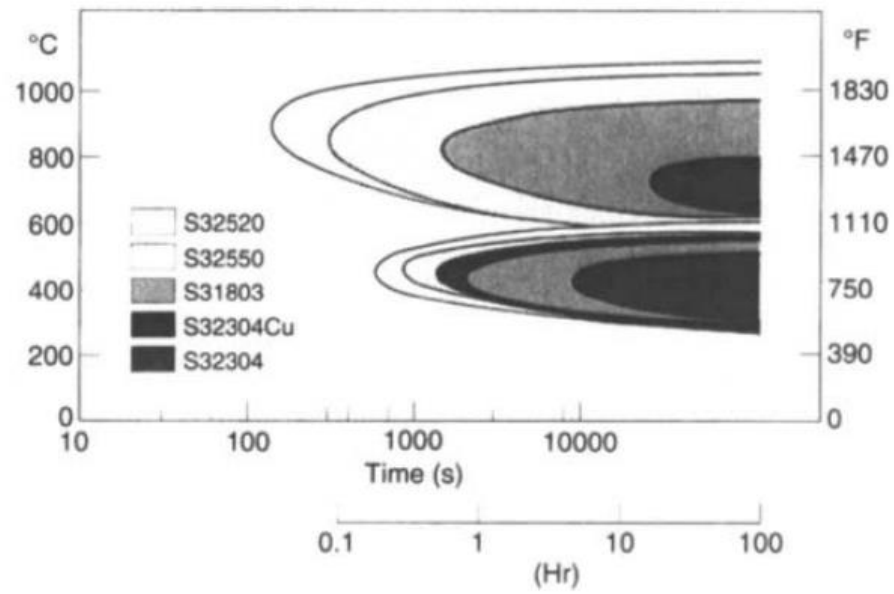


Figure 2.3 TTT diagrams of duplex stainless steels derived by optical metallography between 600 and 1050°C and hardness measurements between 300 and 600°C.

In addition to TTT diagram for the prediction of microstructure and phase balance, the ferrite potential (FP) and ferrite factor (FF), which was proposed by Wolf et al. [61] and Kaltenhauser [62], are often used to describe the amount of austenite and ferrite after solidification. The FP is calculated based on the Cr-Fe-Ni equilibrium diagram using nickel and chromium equivalents, as the following equations.

$$PF = 5.26 \left( 0.74 - \frac{Ni_{equivalent}}{Cr_{equivalent}} \right) \quad (2.3)$$

$$Ni_{equivalent} = \%Ni + 0.31\%Mn + 22\%C + 14.2\%N + \%Cu \quad (2.4)$$

$$Cr_{equivalent} = \%Cr + 1.5\%Si + 1.4\%Mo + 3\%Ti + 2\%Nb \quad (2.5)$$

The lower PF (less than 3.5) usually promotes the formation of austenite phase and suppresses grain growth of ferrite phase so that stainless steel has a fine grain microstructure, subsequently, higher strength. The FF, which is defined by the Eq.2.6, is used to evaluate the amount of austenite phase at high temperatures.

$$FF = Cr + 6\%Si + 8\%Ti + 4\%Mo + 2\%Al + 4\%Nb \\ - 40\%(C + N) - 2\%Mn - 4\%Ni \quad (2.6)$$

High values of FF indicate more austenite could be present at high temperature. In addition, both the FP and the FF are employed to assess the susceptibility of cracking in ingots.

## 2.2 Martensitic Phase Transformation

### 2.2.1 Mechanism of the martensitic phase transformation

The phase transformation of austenite to  $\epsilon$ - or  $\alpha'$  martensite can be resulted from diffusionless shear process in steels with low alloyed austenite phase with cooling at or below the martensite start temperature ( $M_s$ ). This transformation process is defined as diffusionless transformation, which is described as any transformation in which atomic movements are less than one interatomic spacing [63]. Hence, in general, fast cooling or heating rate is required to prevent the diffusional movement of atoms in diffusionless transformation process. Here, the mechanisms of martensite nucleation and growth will be introduced separately.

According to the theory of thermodynamics, the following equation could provide the driving force for the nucleation of martensite,

$$\Delta G^{\gamma \rightarrow \alpha'} = \Delta H^{\gamma \rightarrow \alpha'} \frac{(T_0 - M_s)}{T_0} \quad (2.7)$$

where  $\Delta G^{\gamma \rightarrow \alpha'}$  is the difference of free energy between  $\gamma$  austenite and  $\alpha'$  martensite,  $\Delta H^{\gamma \rightarrow \alpha'}$  is the enthalpy difference between  $\gamma$  austenite and  $\alpha'$  martensite,  $T_0$  is the equilibrium temperature for austenite and martensite phases, and  $M_s$  is the martensite start temperature [63]. Hence, the energy barrier for martensitic phase transformation can be overcome by large free energy difference when the cooling rate is large enough, subsequently, transformation from austenite to martensite is promoted. The energy barrier is related to the interfacial free

energy (surface energy), and the strain energy. However, considering the small value of surface energy, the strain energy for martensite nucleation is more important than the surface energy. The schematic representation of a martensite nucleus is shown in Figure 2.4 [63]. Based on this geometry and Gibbs free energy equation of a system, the energy barrier for martensite nucleation can be described by the following equations:

$$\Delta G = A\gamma + V\Delta G_s - V\Delta G_v \quad (2.8)$$

$$\Delta G = 2\pi a^2\gamma + \frac{2\mu V \left(\frac{s}{2}\right)^2 \frac{2(2-\nu)}{8(1-\nu)} \pi c}{a} - \frac{4}{3}\pi a^2 c \cdot \Delta G_v \quad (2.9)$$

where  $\gamma$  is the coherent interfacial energy,  $\mu$  is the shear modulus of austenite,  $s$  is the shear strain,  $\nu$  is the Poisson ratio of austenite,  $\Delta G_v$  is the volume free energy release,  $V$  is the volume of the martensite nucleus, and  $a$  and  $c$  are shown in the Figure 2.4 as radius and half-thickness before and after shear strain.



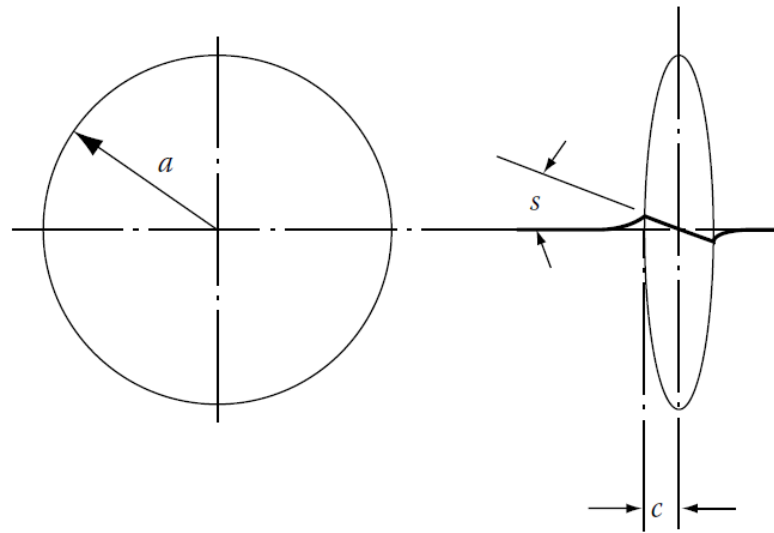


Figure 2.4 Schematic representation of a martensite nucleus [63].

Moreover, the martensite nucleation indeed is affected by dislocations. The formation of bcc structure from fcc structure by the movement of  $\langle 112 \rangle$  partial dislocations during twinning was investigated by Zenner [64], as shown the schematic diagrams in Figure 2.5. The twinning dislocation,  $\frac{a}{6}[\bar{2}11]$ , can be induced by the dissociation of a perfect dislocation into two partial dislocations, as shown in the following equations:

$$\frac{a}{2}[110] = \frac{a}{6}[\bar{2}11] + \frac{a}{6}[\bar{1}2\bar{1}] \quad (2.10)$$

It requires a movement of atoms by  $\frac{a}{12}[\bar{2}11]$  to form the bcc crystal structure from the fcc crystal structure. Brooks et al. [65] also proposed that the pile-ups of dislocations, in which the partial dislocations are accumulated, promote the nucleation of martensite. Considering the hcp structure  $\epsilon$ -martensite forming from the fcc structure  $\gamma$ -austenite, Venables [66] suggested one transformation model to explain the transformation from fcc structure to hcp structure, as shown in Figure 2.6. Depending on the overlapping of stacking faults on successive  $\{111\}$  planes, twins can form. Thus, the  $\epsilon$ -martensite structure thickens if inhomogeneous half-twinning shears on alternative  $\{111\}$  planes. This transformation region in deformed 17%Cr-8%Ni stainless steel was observed as shown in Figure 2.7 [63], which verified the dislocation-assisted martensite transformation according to Venables model. Furthermore, Kelly [67] found that the  $\epsilon$ -martensite was generated on the overlapping of stacking faults in Mn-Cr-Ni steel with quenching to  $-196^\circ\text{C}$ . There have been extensive efforts to investigate the sites of  $\alpha'$  martensite

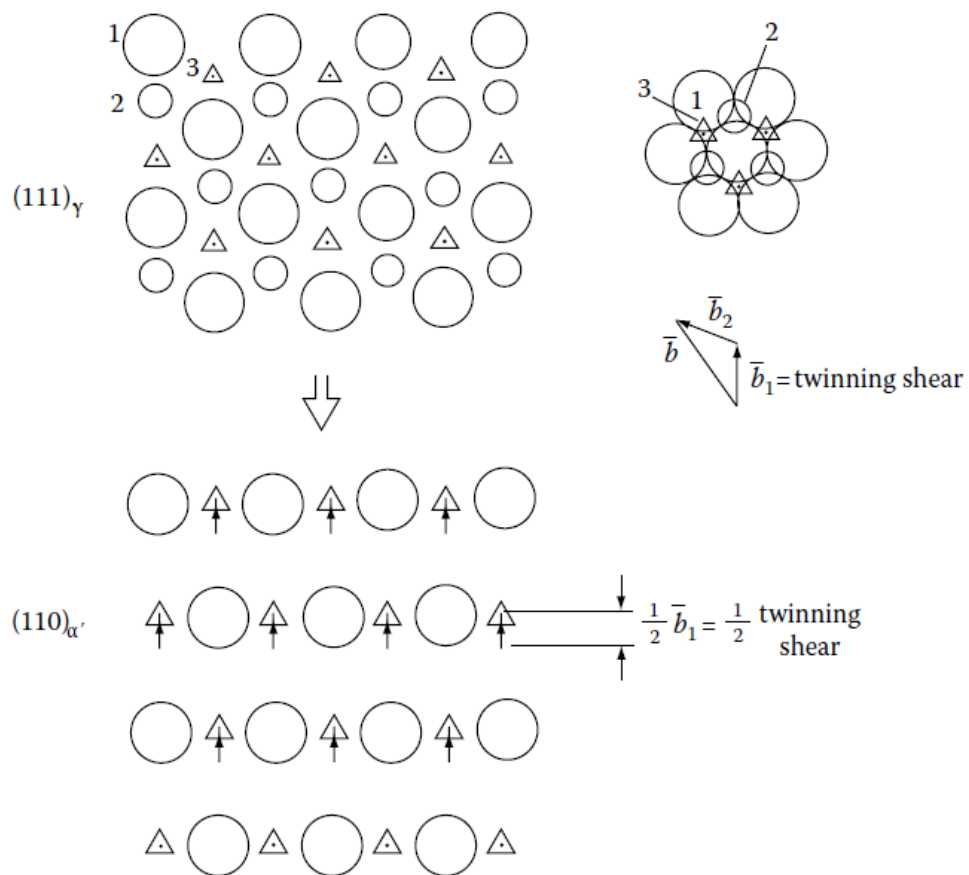


Figure 2.5 Zener's model of the generation of two-atom-thick martensite by a half-twinning shear [63].

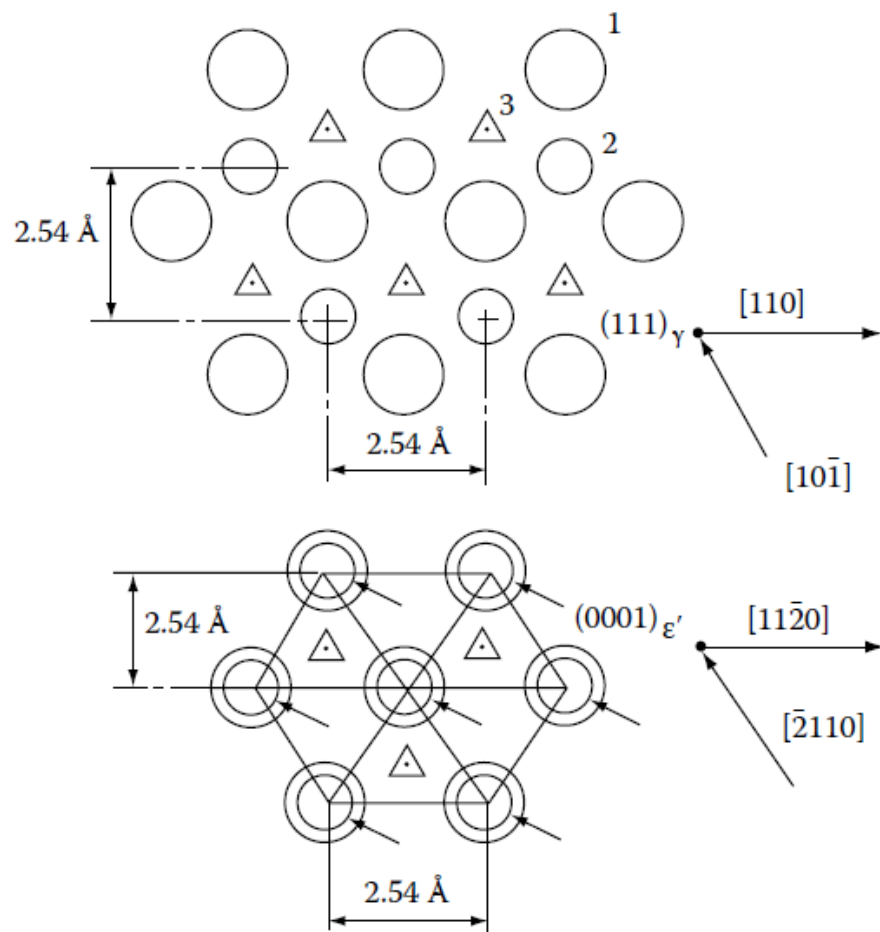


Figure 2.6 Venables' model for the  $\gamma \rightarrow \epsilon' \rightarrow \alpha'$  transformation in stainless steel.

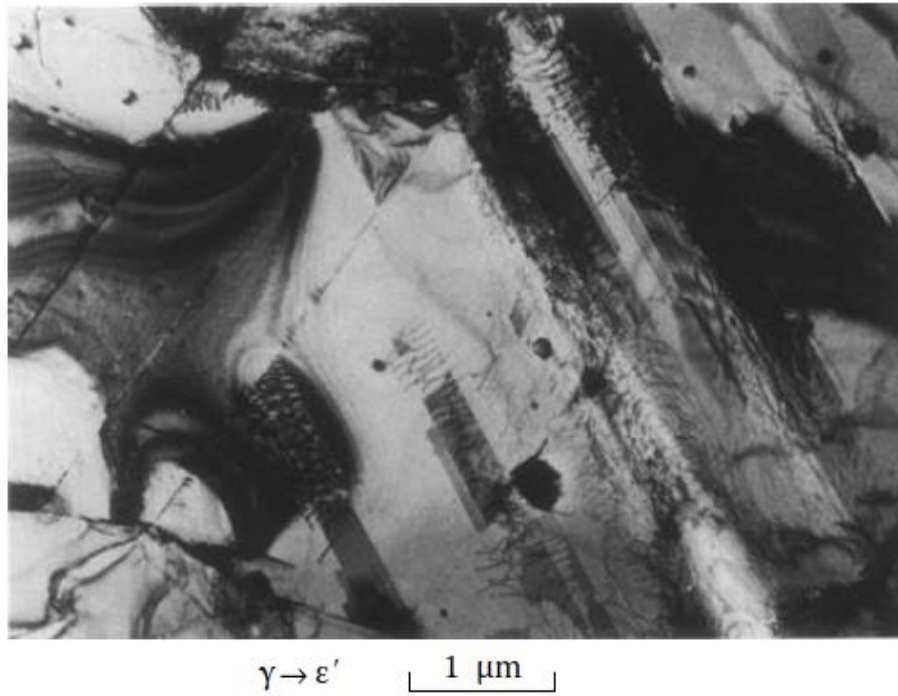


Figure 2.7 Dislocation-assisted martensite transformation in a physically deformed 17%Cr-8%Ni stainless steel [63].

formation since several decades ago. For example, there were evidences studied by TEM that the interactions of the  $\varepsilon$ -martensite, which acted as the sites of nucleation of  $\alpha'$ -martensite, promote the formation of  $\alpha'$ -martensite, as shown in Figure 2.8 [68]. Therefore, the transformation route,  $\gamma \rightarrow \varepsilon' \rightarrow \alpha'$ , in which  $\alpha'$  martensite forms via intermediate  $\varepsilon'$  martensite, was suggested and generally accepted. Figure 2.9 present the schematic model for bcc structure formation from an hcp structure [63]. It is thus seen that the generation and movement of dislocations can directly induce the martensitic phase transformation. It is well known that the generation and movement of extended dislocations are related to stress/strain field, so that the martensitic phase transformation also can occur by the help of stress or strain at the temperature above  $M_s$ , i.e. stress-induced or stain-induced martensitic phase transformation. The interaction provided from strain field associated with dislocations can be a favorable site of martensite nucleation, thus the dislocation interaction energy can contribute to reduce the energy barrier to promote formation of nuclei. Hence, the total energy barrier of martensite nucleation in Eq.2.8 can be modified by subtracting the dislocation interaction energy, as shown in the following equation:

$$\Delta G = A\gamma + V\Delta G_s - V\Delta G_v - \Delta G_d \quad (2.11)$$

$$\Delta G_d = 2\mu s\pi \cdot ac \cdot b \quad (2.12)$$

where  $\mathbf{b}$  is the Burges vector of the dislocation, and  $s$  is the shear strain. Subsequently, Eq.2.9 can be rewritten as:

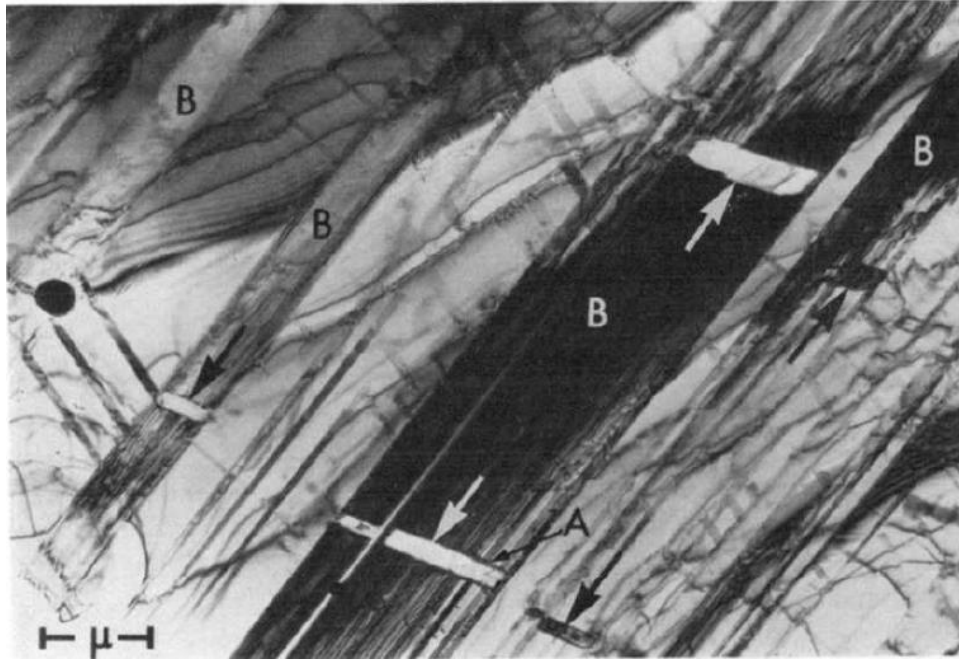


Figure 2.8 Mn-Cr-Ni steel quenched to 196°C showing a number of large  $\varepsilon$ -bands (B) containing  $\alpha$ -martensite laths. The positions of these laths are indicated by the large arrows and projected width of the  $\alpha$ -martensite habit plane interface is visible at A [68].

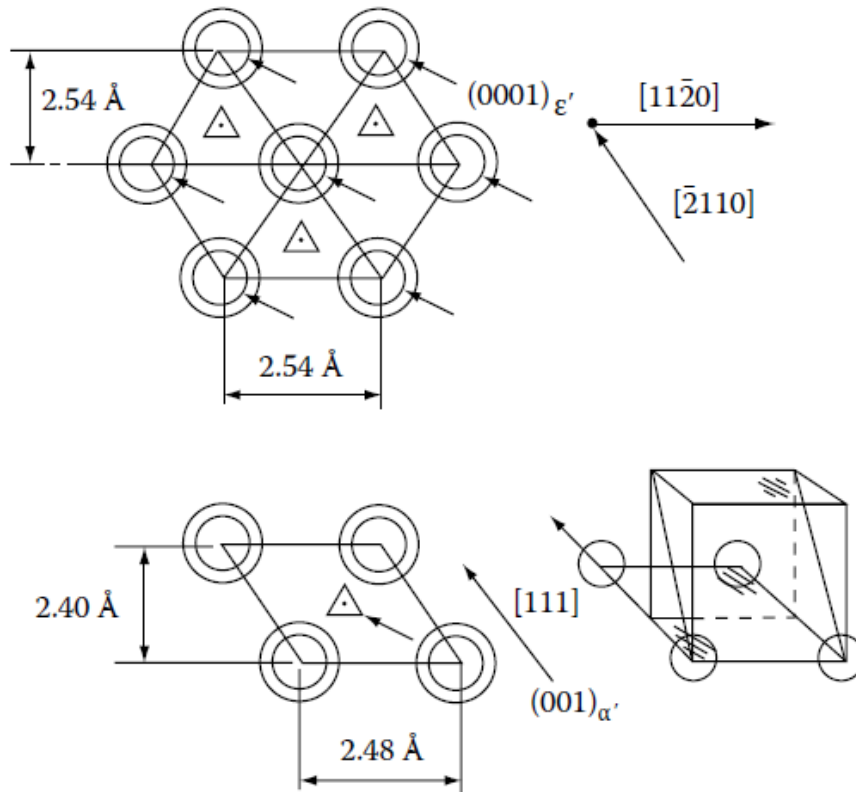


Figure 2.9 Schematic model for bcc structure formation from an hcp structure [63].



$$\Delta G = 2\pi a^2 \gamma + \frac{2\mu V \left(\frac{s}{2}\right)^2 \frac{2(2-\nu)}{8(1-\nu)} \pi c}{a} - \frac{4}{3} \pi a^2 c \cdot \Delta G_v - 2\mu s \pi \cdot ac \cdot b \quad (2.13)$$

As mentioned above, the shear stress or strain is critical for martensitic phase transformation by the aid of dislocations. Hence, the martensite start temperature ( $M_s$ ) can be increase to another martensite start temperature ( $M_d$ ), which is associated with plastic strain or stress, when there is the one component of applied stress or strain parallel to the shear deformation.  $M_d$  can vary from the temperature range of the start martensite temperature ( $M_s$ ) to the equilibrium temperature ( $T_0$ ) between austenite and martensite.

After the energy barrier of martensite nucleation has been exceeded, martensite will grow with a very high speed until it encounters an obstacle, such as high angle grain boundary. In general, two main morphologies of martensite growth are presented as lath and plate martensite. In the case of growth of lath martensite, it has been postulated that transformation dislocations, which induced by martensitic phase transformation due to the mismatch between the bct and fcc lattices, could be promoted to nucleate by itself at the lath surface. In order to reach this dislocation nucleation, the stresses have to overcome the strength of the material. Hence, Eshelby [69] suggested a model for the growth of lath martensite based on a geometry of ellipsoidal with  $a \gg c$ . At the surface between martensite and

austenite, the maximum shear stress,  $\sigma$ , induced by phase transformation is given as the following equation:

$$\sigma \cong \frac{2\mu sc}{a} \quad (2.14)$$

where  $\mu$  is the austenite shear modulus, and  $s$  is the shear strain. It can be found that the maximum shear stress depends on the martensite shape. On the other hand, the martensite formed in high stacking fault energy (SFE) or lower  $M_s$  temperature usually is the plate-like morphology with more retained austenite. Due to twinning in this case can easily be produced, plate martensite is often related to and promoted by twinning. To minimize the mismatch between martensite and austenite in a plate-like morphology, there has been found that a  $(522)_\gamma$  habit plane, which is related to twinning, can be the interface between martensite and austenite.

As regard to the mechanism of strain-induced martensitic phase transformation and martensite growth at temperature range of  $M_s$  to  $M_d$ , a model, which contains the interactions and relationships among shear bands, plastic strains, martensite formation, has been suggested by Olson and Cohen. The equations of Olson-Cohen model are shown as following:

$$f^{\alpha'} = 1 - \exp(-\beta(1 - e^{-\alpha\varepsilon}))^n \quad (2.15)$$

where  $f^{\alpha'}$  is the volume fraction of  $\alpha'$  martensite,  $\beta$  is a constant related to the volumes of  $\alpha'$  martensite and shear band,  $\alpha$  is a constant related to stacking fault

energy and strain rate,  $\varepsilon$  is the plastic strain, and  $n$  is a constant, which can be derived from the following equation:

$$N_v^I = K(N_v^{sb})^n \quad (2.16)$$

where  $N_v^I$  is the number of shear band intersections,  $K$  is a constant number, and  $N_v^{sb}$  is the number of shear bands.

In addition, it is worth to note that martensitic phase transformation is a deformation mechanism, and thus in some low SFE material it competes with the deformation mechanism of twinning and slipping.

### **2.2.2 Orientation relationship**

To complete the transformation from fcc crystal structure to bct/bcc crystal structure, Bain proposed one transformation model in which the bct structure can be obtained from fcc structure with the minimum of strain and atomic movement. In the Bain model, the z direction has to be compressed by 20% and x and y directions has to be extended by 12%. According to Bain model, the orientation relationship can be obtained as following:

$$(111)_\gamma // (110)_{\alpha'}$$

$$[\bar{1}01]_\gamma // [\bar{1}\bar{1}1]_{\alpha'}$$

$$[1\bar{1}0]_\gamma // [100]_{\alpha'}$$

$$[11\bar{2}]_\gamma // [01\bar{1}]_{\alpha'}$$

Furthermore, there has been observed that an undeformed plane, or called habit plane exists and is not distorted during phase transformation. However, this observation does not geometrically agree with the Bain model in which there is no an undistorted plane. Hence, in efforts to account for the habit plane during martensitic phase transformation, an extra deformation on the Bain model has to be added. As mentioned above, the dislocation slip or twinning can provide the additional deformation and thus influence the nucleation of martensite. Applying slip or twinning to the Bain model, the lattice distortion caused by Bain model can be compensated by the shear deformation. In the crystallographic theory, it is postulated that dislocation slip or twinning present in  $\{11\bar{2}\}\{111\}$  system in  $\alpha$  martensite, which is corresponding to  $\{110\}\{1\bar{1}0\}$  system in  $\gamma$  austenite.

In addition, there are two main orientation relationship between parent phase and transformed phase, which are generally accepted, i.e. Kurdjumov-Sachs (KS) relation (  $[\bar{1}01]_{\gamma} // [\bar{1}\bar{1}1]_{\alpha'}$  ) and Nishiyama-Wasserman (NW) relation (  $[1\bar{1}0]_{\gamma} // [101]_{\alpha'}$  ). These orientation relationships were obtained from the experimental observation. The experimental observation of orientation relationship between austenite and martensite presents  $(111)_{\gamma}$  is almost parallel to  $(110)_{\alpha'}$  with an error of  $5^{\circ}$  angles. This real orientation relationship varies between KS relation and NW relation. Moreover, Kurml et al. [70] observed that the martensite and austenite show the following orientation relationship:

$$(111)_{\gamma} // (0001)_{\varepsilon} // (110)_{\alpha'}$$

$$(110)_{\gamma} // (2110)_{\varepsilon} // (111)_{\alpha'}$$

### **2.2.3 Stacking fault energy**

The stacking sequence of atoms in  $\{111\}$  plane of fcc crystal structure is ABCABC. Slip, which usually dissociates into two partial dislocations as discussed above, exists on the  $\{111\}$  plane and in the  $\langle 110 \rangle$  direction of the fcc structure. As a result, the dissociation of slip creates a stacking fault ABCAC|ABC in the  $\{111\}$  plane stacking sequence. For example, if one layer is shifted by slip to ACAC in certain region. It can result in a hcp crystal structure with the ACAC type stacking. Hence, stacking fault can promote the formation of hcp phase in fcc phase in a certain region. The stacking fault energy (SFE), which can represent the tendency for forming stacking faults is defined as the measure of the distance between the partial dislocations.

The SFE is an important factor to determine the deformation mode, i.e. phase transformation, twinning, and slip of dislocations, of austenitic stainless steels. According to previous studies, the martensitic phase transformation from austenite is favorable in the low SFE ( $<20 \text{ mJ/m}^2$ ) and leads to phase transformation induced plasticity (TRIP) mechanism in austenitic steels. Middle SFE ( $20\text{-}45 \text{ mJ/m}^2$ ) promotes the twinning induced plasticity (TWIP) during deformation by the formation of twinning in austenite. In the low and middle SFE stainless steel alloys, the cross slip and dislocation climb is prevented since the extend screw dislocations cannot cross slip without the perfect dislocation combined by partial dislocations. And high SFE ( $>45 \text{ mJ/m}^2$ ) impedes the dissociation of perfect

dislocations into partial dislocations and thus the deformation mechanism of deformation is dominated by dislocation slipping. Subsequently, the difference of SFE in stainless steel leads to the different type of deformed textures in austenite due to the influence of deformation mechanism on the development of texture.

It is discussed above that the formation of  $\alpha'$  martensite strongly connects to the intersections of planar deformation structures, such as shear bands, twins, or  $\varepsilon$  martensite, which is depended on the SFE. Hence, the stability of austenite can be varied by its SFE. The SFE of stainless steels is mainly dependent on the chemical compositions and temperature. There have been a number of efforts to investigate the effects of chemical elements on the stability of austenite. Talonen et al. [71], for example, has suggested that the strain-induced martensitic phase transformation is affected more by SFE than the driving force,  $\Delta G^{\gamma \rightarrow \alpha'}$ .

To understand the effect of composition in stainless steel on SFE, several empirical equations have been proposed for the SFE calculation from the chemical elements. One of them is presented as following equation [72]:

$$SFE (mJ/m^2) = -25.7 + 2\%Ni + 410\%C - 0.9\%Cr - 77\%N - 13\%Si - 1.2\%Mn \quad (2.17)$$

Nevertheless, the interaction among alloying elements is not involved in this empirical equation. As regard this shortcoming, Dai et al. [73] suggested an expression considering the interaction of alloying elements. The equation is given as:

$$\begin{aligned}
SFE\gamma^{300}(mJ/m^2) = & \gamma^0 + 1.59\%Ni - 1.34\%Mn + 0.06Mn^2 - 1.75\%Cr + 0.01\%Cr^2 \\
& + 15.12\%Mo - 5.59\%Si - 60.69(\%C + 1.2\%N)^{0.5} + 0.61[\%Ni(\%Cr + \%Mn)]^{0.5} \\
& + 26.27(\%C + 1.2\%N)(\%Cr + \%Mn + \%Mo)^{0.5}
\end{aligned} \tag{2.18}$$

where  $\gamma^{300}$  is the value of SFE at ambient temperature and  $\gamma^0$  is the value of SFE of pure austenitic iron at ambient temperature. The drawback of those empirical equations is their limited data source. For instance, in the case of the Fe<sub>66</sub>Ni<sub>14</sub>Cr<sub>20</sub> alloy, the SFE is increased as the decreasing of spin moment, suggesting that it is sensitive to the magnetic moment in this alloy. Hence, computational thermodynamics based on the quantum mechanical first-principles method have been developed to study the SFE in stainless steels. Also, to complement the results calculated by modelling, TEM can be used to measure the SFE experimentally.

Besides the effect of alloying elements on SFE, the temperature also plays an important role on SFE. In general, the increasing of temperature leads to the increase of SFE due to the reduction of widths of dislocations by high temperature.

#### **2.2.4 Factors affecting the martensitic phase transformation**

Factors like alloying elements, stress fields, strain rate, grain size, austenite texture, hydrogen contents, magnetic field, etc. can affect the martensitic phase transformation in a metastable austenitic stainless steel.

As discussed in section 2.3.3, it has been known that the SFE of austenite strongly depends on the alloying elements and temperature, therefore these two factors indeed can influence the martensitic phase transformation in a metastable austenite phase. Beside the development of empirical equations related chemical composition to SFE, several empirical equations have been developed to correlate the alloying elements in solution to the  $M_s$  and  $M_d$  temperatures:

$$M_s(\alpha') = 1305 - 61.1\%Ni - 41.7\%Cr - 33.3\%Mn - 27.8\%Si - 1667\%(C + N) \quad (2.19)$$

$$M_d(\alpha')(30/50) = 413 - 9.5\%Ni - 13.7\%Cr - 8.1\%Mn - 9.2\%Si - 18.5\%Mo - 462\%(C + N) \quad (2.20)$$

where  $M_d(\alpha')(30/50)$  is the temperature at which 50%  $\alpha'$  martensite has been formed after 30% tensile true strain. Bowkett [74] investigated the influences of content of Ni and cold working on the amount of  $\alpha'$  martensite formed in 18Cr-8Ni, type 321 and 18Cr-12Ni austenitic steels at room temperature, suggesting that the content of strain-induced  $\alpha'$  martensite decreases with the increase of Ni.

The effect of deformation mode, such as tension, compression, and torsion, on the martensitic phase transformation behavior in austenitic steels has been confirmed by several studies. For example, Han et al. [75] investigated the change of  $M_s$  temperature by different deformation modes, i.e. uniaxial tension, uniaxial compression, and hydrostatic compression, in Fe-0.5 wt.% C-20 wt.% Ni and Fe-



30 wt.% Ni through comparing between calculated results and experimental data. The results show that  $M_s$  temperature increases as increasing of external stresses in tension and compression, while decreases with increasing of stresses in hydrostatic compression. It thus suggests that the deformation mode has a strong influence on the martensitic phase transformation.

Furthermore, a lot of studies have proposed that strain rate affects the martensite transformation through adiabatic heating. Han et al. [75] shows the mechanically induced martensite phase fraction as a function of true strain with varied strain rate base on modeling and experiments. It has been found that the volume fraction of martensite at a given true strain decreases markedly as the increase of strain rate. The temperature rise during deformation is as a result of the plastic deformation and the phase transformation. The change of temperature during deformation increases with the strain rate. Therefore, as the strain rate increases, the tendency of formation of shear bands is reduced due to elevated temperature.

The grain size of austenite has also been reported to influence the formation of martensite. Raman et al. [76] reported that coarser austenite grains can induce more amount of  $\alpha'$  martensite. One acceptable interpretation is the refinement of the austenite grain size results the Hall–Petch strengthening of austenite, thus leading it difficult for martensite transformation. Moreover, a high angle grain boundary can act as an effective barrier to prevent the growth of martensite as it depends on the coherency of surrounding austenite. There have been efforts to study the relationship between austenite grain size and  $M_s$  temperature. A study

of a series of low-alloyed steels was produced by Yang et al. [77] shows that the increase of  $M_s$  temperature is induced by the increase of austenite grains size, and it reaches a saturation level of the temperature around 340 °C. The reduction of  $M_s$  temperature is required with a higher driving force for martensite to form due to a stronger austenite of finer grains. Addition to this, the finer grain lead to a higher aspect ratio of martensite, therefore, increasing the stored energy and the driving force as well.

In terms of the texture relation between the parent and the product phases, the phase transformation in metastable austenitic SS is postulated to follow the KS relationship which offers 24 variants. However, Kireeva et al. [78] and Humbert et al. [37] have demonstrated that the martensitic phase transformation is orientation-dependence. In the other words, not all the variants are favored in this mechanism that leads to the various variant selection studies. Humbert et al. [37] studied the variant selection of martensitic phase transformation using EBSD on a local texture analysis. As shown in Figure 2.10, the theoretical martensite orientations around (0°, 45°, 0°) represented by plain dots in the theoretical (1 0 0) PF (Figure 2.10(c)) are not present in the experimental (1 0 0) PF (Figure 2.10(b)). In another study,

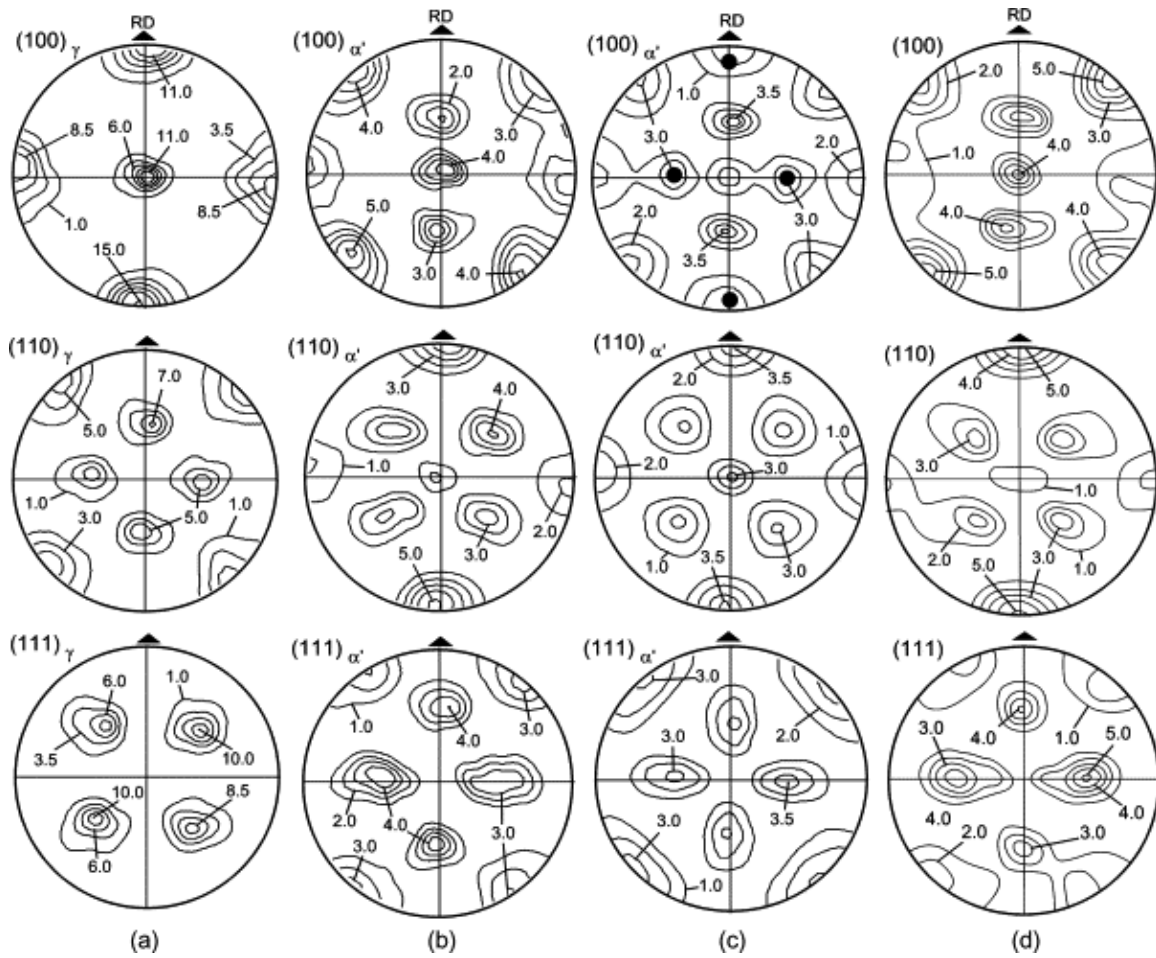


Figure 2.10 Characteristic pole figures after 10% strain at  $T = -60\text{ }^{\circ}\text{C}$  and corresponding to: (a) experimental  $\gamma$  grain orientations belonging to the Cube component  $\{1\ 0\ 0\}\langle 1\ 0\ 0\rangle$ , (b) experimental  $\alpha'$  martensitic orientations formed in those  $\gamma$  grains, (c)  $\alpha'$  martensitic orientations simulated without variant selection from those  $\gamma$  grains, (d)  $\alpha'$  martensitic orientations simulated with variant selection from those  $\gamma$  grains.

Hedstrom et al. [79] conducted in-situ martensite transformation from  $\gamma$  to  $\varepsilon$  by x-ray diffraction. The orientation dependence of slipping deformation prior to the martensite transformation leads to the occurrence of phase transformation in specific orientations of  $\{111\}\langle 121 \rangle$  with highest Schmid factor.

Beside those factors, hydrogen and magnetic field also influence the stability of the austenite phase and martensite transformation in steels. According to the work of Narita et al. [80], hydrogen-induced phase, i.e.  $\gamma$  to hydride  $\gamma^*$  and  $\varepsilon^*$ , proceeds when austenite is charged by a large amount of hydrogen. Subsequently, the formation of the hexagonal phase,  $\varepsilon^*$ , promotes the nucleation of  $\alpha'$  martensite. Additionally, the effect of magnetic field on the stability of austenite in steel was investigated by Fukuda et al [81]. They suggested that due to both of  $\gamma$  austenite and  $\varepsilon$  martensite are non-magnetic, the magnetic field will not affect the  $\gamma \rightarrow \varepsilon$  phase transformation, but  $\alpha'$  martensite due to its magnetic actually can be induced by a strong magnetic energy from the formed  $\varepsilon$  martensite.

#### ***2.2.5 Effect of $\alpha'$ martensite on mechanical properties***

The influence of  $\alpha'$  martensite on mechanical properties of stainless steel has been investigated in a numerous of studies. In general, the presence of  $\alpha'$  martensite can enhance the strengthening in stainless steels. For instance, Deng et al. [82] studied the effect of content of  $\alpha'$  martensite on strength and ductility of dual phase steels, which contains ferrite and martensite. They observed that the remarkable differences of strength and ductility for five steels, which varies the

content of martensite from 0 to over 90 %, were obtained based on the tensile testing data at room temperature. It is also found that the strength (yield strength and ultimate tensile strength) of those dual phase steels is increasing along with the increase of martensite phase fraction, but decreasing the ductility. It is a result of the harder martensite phase and the load partitioning between martensite and ferrite during deformation. In-situ synchrotron x-ray diffraction measurement was conducted by Cong et al. [83] to investigate the load partitioning between constituent phases. Their results indicate that the martensite bears a large portion of load during loading and additionally provide a high work-hardening rate to maintain high strength.

The martensitic phase transformation with the help of stress or strain occurs in metastable austenite during deformation, and then it results in the transformation induced plasticity (TRIP) effect on the mechanical properties. As the formation of martensite phase during deformation, the austenite grain size is refined, subsequently, enhancing the strength. Meanwhile, the martensite also acts as a barrier to prevent the motion of dislocations and then lead the pile-up of dislocations on the interfaces of austenite and martensite, which results in increased strain hardening of retained austenite phase. Due to the high strain hardening rate induced by martensitic phase transformation, the necking is delayed so that elongation is maintained. In addition, the volume expansion occurs when the transformation from austenite to martensite proceeds. The micro-voids induced by localized stress can be refilled by the volume expansion of phase

transformation, which results in a delayed fracture. Hence, because of the TRIP effect, the metastable austenitic stainless steels and TRIP-aid multiphase steels exhibit excellent mechanical properties with the combination of high strength and good ductility. However, it is worth to note that gradually induced martensitic phase transformation is essential to promote strain hardening rate and ductility, otherwise the rapid transformation would not improve the ductility due to higher amount of hard BCC martensite in the early stage of deformation. There have been a lot of works on TRIP steels to understand the mechanism of TRIP effect deeply under tension, compression, and torsion. For instance, a systematic work has been done by Angel et al. [84] to study the influence of temperature on the tensile behavior of a metastable austenitic stainless steel (18/8 grade austenitic steel). They proposed that the amount of transformed martensite is proportional to the strains, while inverse proportional to the applied temperatures. The decreasing of temperature also leads to an increase of martensitic transformation rate. Tao et al. [17] investigated the stress partitioning between austenite and martensite during uniaxial compression using high-energy x-ray diffraction. The existence of  $\alpha'$  martensite lead to an interaction between constituent phases, like the case of dual phase steels, and the load is transferred from austenite to  $\alpha'$  martensite after yielding. Hence, it can be found that the martensite plays an important role on the strengthening via load partitioning. Furthermore, the texture evolution in the grade 304L stainless steel (metastable austenitic stainless steel) during torsional loading was studied by Cakmak et al. [16]. They found the variant selection of orientations, in which martensite prefers to form, is confirmed. It indicates that the textures of

retained austenite and new-form martensite are a result of the combination of dislocation glide and phase transformation. Consequently, the mechanical properties of this material would be different to the stable austenitic stainless steel due to texture. After the onset of strain-induced martensitic phase transformation, the martensite develops its own deformation texture as the increasing of strains.

Moreover, the TRIP-assisted multi-phase steels, such as TRIP-assisted dual-phase steels and TRIP-assisted duplex steels, are attracted attentions because of the combination of benefits of austenite, martensite, and ferrite, such as high corrosion resistance, high strength, and good ductility. Due to the austenite in those steels is metastable, the beneficial TRIP phenomenon is induced during deformation so that it also can provide high work hardening associated with high strength. Tian et al. [85] conducted in-situ synchrotron x-ray diffraction during uniaxial tensile loading to study the effect of applied strain on martensitic phase transformation and the interaction between constituent phases in TRIP-assisted duplex stainless steel. They found that the martensitic phase transformation induced by plastic strain impact on the load partitioning between phases, in which  $\{111\}$  and  $\{220\}$  lattice planes of austenite phase start to yield and transfer a certain portion of load to martensite when the plastic deformation proceeds.

## **2.3 Crystallographic texture**

Metals, which are crystalline in solid state, in general, exhibit the anisotropic behaviors of mechanical and physical properties. Hence, in a polycrystalline aggregate, individual grains may be different from their neighboring grains in the

grain orientation, and thus the preferred crystallographic orientations, known as texture, in grains lead to be anisotropic in properties. The orientation can be changed during manufacturing processes, such as casting, annealing, rolling, etc., so that randomly distribution of grain orientation is hard to be achieved in microstructure. In this section, the orientation changes that take place during deformation will be discussed. It is as a result of which deformation of polycrystalline aggregate preforms by slipping or twinning, which is orientation-dependence.

The representation of crystallographic texture is by means of pole figures, inverse pole figures, and orientation distribution functions (ODFs). The rolling textures are often represented as being of  $\{hkl\}\langle uvw \rangle$ , in which the plane normal of  $\{hkl\}$  is parallel to the normal direction, ND, and the  $\langle uvw \rangle$  is parallel to the rolling direction, RD, of the sample. The pole figures are frequently used to represent rolling textures since they can be directly obtained by using x-ray diffraction technique. However, the texture information represented by pole figures is not complete, and some information is missing due to the way of presenting texture. Hence, nowadays, there is increasing use of ODFs, which give a more complete description of texture in the Euler orientation space. The inverse pole figures are usually used to explain the fibre textures which are formed during uniaxial loading, such as tension, compression, and extrusion.



### **2.3.1 Rolling texture in face centered cubic (FCC) metals**

The deformation texture of FCC materials primarily depends on their SFE. It is because that the deformation mode varies from twinning to slipping as increasing of SFE. The FCC textures are classified into two main textures, i.e. pure metal texture and alloy texture. The term of pure metal textures is defined as the textures of metals with high SFE, such as aluminum with about  $170 \text{ mJm}^{-2}$  SFE and copper with about  $80 \text{ mJm}^{-2}$  SFE. The slip mode with the  $\{111\}\langle 110 \rangle$  slip systems is predominate, thus ideal texture components related to the slip system are usually observed in pole figures. For instance, the  $\{111\}$  and  $\{100\}$  pole figures of 95% cold rolled aluminum studied by Grewen et al. [86]. The  $\{112\}\langle 111 \rangle$ ,  $\{110\}\langle 112 \rangle$ , and  $\{123\}\langle 412 \rangle$  texture components are observed in the rolling texture of aluminum. The ODFs of  $\varphi_2$  sections are used to represent the texture of 95% cold rolled aluminum. More detailed texture components can be seen in the ODFs. This texture can be described by two fibre textures, i.e.  $\alpha$ -fibre and  $\beta$ -fibre, which contain  $\{011\}\langle 100 \rangle$ ,  $\{110\}\langle 112 \rangle$ , and  $\{110\}\langle 112 \rangle$ ,  $\{123\}\langle 634 \rangle$ ,  $\{112\}\langle 111 \rangle$ , respectively. On the other hand, FCC metals with low SFE, such as 70:30 brass and austenitic stainless steel with  $<25 \text{ mJm}^{-2}$  SFE, develop a type of alloy texture after rolling process. Comparing between pure metal texture and alloy texture, the  $\alpha$ -fibre in alloy texture is more pronounced. Additionally, two fibres ( $\gamma$ -fibre and tau-fibre) are observed in the alloy texture. The materials with intermediate SFE (about  $40 \text{ mJm}^{-2}$ ) usually develop the tau-fibre texture after rolling process. Texture transition between pure metal texture and alloy texture occurs in the materials with

intermediate SFE or by changing the temperature of deformation. There is an evidence to which the texture transition is induced by increasing temperature in 304L austenitic stainless steel. It shows that as increase of temperature the rolling texture varies from the type of alloy texture to the type of pure metal texture.

### ***2.3.2 Rolling texture in body centered cubic (BCC) metals***

The rolling textures in BCC metals are almost identical and largely independent of solute additions and processing parameters. The effect of temperature on the rolling texture of BCC materials is studied to be limited. The rolling texture of 90% cold rolled low carbon steel is described in {200} pole figure. The prominent components like {111}<112>, {111}<110>, {110}<011>, and {211}<011> are composed in this pole figure. Due to a lot of important texture components in BCC metals are involved in an ODF section of  $\varphi_2 = 45^\circ$ , only this section is frequently discussed to study the texture of BCC materials. It is well known that  $\alpha$ -fibre texture comprising <110> parallel to the rolling direction and  $\gamma$ -fibre texture composed of <111> parallel to the normal direction are generally formed during deformation in BCC materials. The texture of a cold rolled interstitial-free steel in ODF section of  $\varphi_2 = 45^\circ$ . The  $\alpha$ -fibre and  $\gamma$ -fibre are clearly presented with a stronger  $\alpha$ -fibre compared with  $\gamma$ -fibre.

### ***2.3.3 Fiber texture***

The deformation textures of metals subjected to uniaxial deforming process, like tension, compression, wires or rods, extrusion, etc. usually develop the preferred

crystallographic orientations which are fibrous, known as fibre textures. The inverse pole figures are often used to describe this type of textures. In general, there has a difference of texture between surface and interior of material, which is attributed to the friction at the surface. The deformation textures at surface are more complex than that in interior. Also, it depends essentially on the crystal structure and processing variables.

In FCC materials, a double fibre texture with  $\langle 111 \rangle$  and  $\langle 100 \rangle$  parallel to the tensile or extruded axis is developed by tension or constrained tension. The intensities are concentrated in two components, i.e.  $\langle 111 \rangle$  and  $\langle 100 \rangle$ . The relative proportions of  $\langle 111 \rangle$  and  $\langle 100 \rangle$  components are primarily related to the SFE. The fibre texture of AgCl polycrystals extruded at 77K composes  $\langle 111 \rangle$  and  $\langle 100 \rangle$  components along the axis, whereas a higher concentration of  $\langle 100 \rangle$  component is developed compared to  $\langle 111 \rangle$  component. Therefore, as the SFE increasing, the amount of  $\langle 100 \rangle$  component of fibre texture in FCC material is decreasing. However, the deformation texture in FCC materials subjected to uniaxial compression is different to those under tension or extrusion. It is attributed to the fact that the plastic deformation is promoted by single slip so that the normal vector of active slip plane is rotated toward the direction of uniaxial loading, whereas in the case of tension the slip vector is rotated toward the axis of tensile loading. Thus, the final orientations after tension is opposite to that after compression, i.e. a fibre texture comprising of a strong  $\langle 110 \rangle$  component and a scattering between  $\langle 110 \rangle$  and  $\langle 113 \rangle$  tends to form in the case of uniaxial compression. The strong

component around  $\langle 110 \rangle$  associated with a spread from  $\langle 110 \rangle$  to  $\langle 113 \rangle$  and  $\langle 112 \rangle$  in compression texture is observed. There is a weak  $\langle 100 \rangle$  component in this fibre texture as well, but  $\langle 111 \rangle$  component is absent. For some FCC metals, like CuAl alloys with low SFE, beside the predominant  $\langle 110 \rangle$  and the scattering of  $\langle 110 \rangle$  to  $\langle 113 \rangle$  components, a weak component around  $\langle 111 \rangle$  develops instead of  $\langle 100 \rangle$ . The characters of this compression texture in FCC materials depend on the SFE as well.

In BCC materials, the fibre texture is always  $\langle 110 \rangle$  parallel to the axis of tension or constrained tension. Compression texture is also different and almost opposite to the case of tension or constrained tension in BCC materials. A double  $\langle 111 \rangle$  and  $\langle 100 \rangle$  fibre texture can be developed in BCC metals, such as Fe or Si-ferrite, subjected to compression. In general, the relative proportion of  $\langle 111 \rangle$  component compared with  $\langle 100 \rangle$  component is always higher.

#### ***2.3.4 Factors influencing texture development***

In addition to those described just, several factors, such as temperature, grain size, second phase, etc., may have an effect on the development of the deformation texture.

The temperature may affect the deformation texture including texture components and intensities, and due to the annealing process induces different type of texture to deformation, the deformation at high temperature may develop textures which is affected by dynamic recrystallization. For instance, the effect of temperature on

the development of rolling texture in two iron–silicon–(carbon) steels was investigated by Atake et al [87]. Volume fraction of texture fibre components, i.e.  $\langle 111 \rangle // \text{ND}$ ,  $\langle 110 \rangle // \text{ND}$ , and  $\langle 100 \rangle // \text{ND}$ , as a function of rolling temperature in ultra-low carbon (ULC) steel and interstitial free (IF) steel under rolled and recrystallized conditions, respectively, is present. In the rolled condition,  $\langle 111 \rangle$  and  $\langle 100 \rangle$  parallel to ND components show an increase along with the increasing of temperature, while  $\langle 110 \rangle // \text{ND}$  component is declining slightly at elevated temperature.

Grain size plays an important role in the development of microstructure and texture during deformation. Barnett et al. [88] studied the influence of grain size on deformation texture in wrought Mg–3Al–Zn alloys with average grain sizes of 3  $\mu\text{m}$  and 16  $\mu\text{m}$ , respectively, by using electron backscatter diffraction (EBSD). The inverse pole figures of Mg alloys with 3  $\mu\text{m}$  and 16  $\mu\text{m}$  grain sizes along the extrusion axis indicate the coarse grains may tend to develop the extrusion texture consisting of the primary component, which locates in between  $\langle 10\bar{1}0 \rangle$  and  $\langle 2\bar{1}\bar{1}0 \rangle$ .

## **2.4 Deep drawing and the formability of high-strength steel alloy**

Deep drawing operation as a sheet-metal forming process is used to shape the products. It is one of the most important sheet-metal forming processes because of its wide-spread use in industrial applications, especially in automotive industry. In general, the plastic flow in the metal alloys during deep-drawing process is

strongly influenced by the deep-drawing parameters, i.e. geometry of punch and die, blank holding force, punch speed, clearance between punch and die, and lubrication. Moreover, the temperature plays an important role in the deformation behavior of material during the deep-drawing process. Most of deep-drawing processes are used at ambient temperature on sheet metal alloys to form designed shapes. The formability of metal alloys is examined using deep-drawing process (Swift test) by manufacturing cylindrical cups.

In general, high tensile elongation, high strain-hardening rate, and low plastic anisotropy in metal alloys are good for the deep-drawing process. For example, low-carbon steel alloys are the most commonly used because of its low cost and generally high tensile strength and ductility. Moreover, most recently developed third-generation advanced high-strength steel alloys with high tensile strength and elongation, such as the TRIP and/or TWIP steel alloys, have been developed to meet the improved requirements on the broad applications in industry. However, as describe earlier, the high-strength steel alloys usually exhibit the poor formability during deep-drawing process at ambient temperature due to the cracking phenomenon. It has been shown that the cracking phenomenon in high-strength steel alloys subjected to deep-drawing process is strongly correlated to the residual stresses generated from the heterogeneous plastic deformation. Moreover, the formability or cracking behavior in high-strength steel alloys also depends on the microstructure of steel alloys, such as constituent phases and crystallographic texture.

## **CHAPTER 3 Effects of Phase Transformation Kinetics, Constituent Phases, Crystallographic Texture on Phase-Specific Tensile Stress Partitioning in Alloy Plates**

### **3.1 Introduction**

The formability of advanced high-strength steels is an important issue for successful and broad structural applications. In general, high tensile ductility is considered to be essential for a good formability. The transformation induced plasticity (TRIP) steel alloys, with high tensile strength and ductility, have been developed to meet this requirement. As the strain-induced  $\alpha'$ -martensitic phase transformation leads to an increase in the strain-hardening rate during the plastic deformation, the onset of necking is delayed and the ductility is enhanced [25, 66, 89]. However, the TRIP steels frequently exhibit a cracking problem during a sheet-metal forming process, such as the deep-drawing process, despite its high toughness [20, 21, 90]. The tensile residual-stress concentration is one of the critical factors for this cracking behavior [27, 91, 92]. During the deep-drawing process, inhomogeneous plastic deformation can result in a local concentration of macroscopic residual stresses. Simultaneously, microscopic interphase residual-stress localization could also be caused by the microstructural changes in TRIP steels during the severe plastic deformation due to the stress partitioning among constituent phases and the sheet-plastic anisotropy.

The interphase stress partitioning occurs in the TRIP steels or other multi-phase steels during the deformation due to the difference in mechanical properties

between constituent phases. In those steels, the stress partitioning among constituent phases occurs at different stress or strain levels due to the difference of phase-specific mechanical behavior [17, 93]. For example, Tao et al. [17], using an in-situ neutron diffraction (ND) characterization of a metastable 304L austenitic stainless steel (SS), showed that the applied stress concentrates in the strain-induced  $\alpha'$ -martensite phase due to the stress partitioning between austenite and  $\alpha'$ -martensite during the tensile plastic deformation. Furthermore, the micro-mechanical behavior of a duplex SS under uniaxial loading has been investigated using in-situ ND, showing that the plastic flow initiates in the austenite phase, and subsequently in the ferrite phase which carries higher applied stress during the plastic deformation [94-96]. The martensitic transformation kinetics can be influenced by the changes in the phase-specific stress or strain in a TRIP steel. Based on this concept, Wu et al. [26] recently proposed a strategy of TRIP-assisted steel alloy designed to enhance the advantage of TRIP effect by manipulating the phase-specific stress, which, in turn, influence the martensitic phase transformation.

It has been reported that the residual stress in a deep-drawn AISI-1010 cup measured by ND is higher at the rolling direction (RD) than at the transverse direction (TD), indicating that the sheet-plastic anisotropy can result in an inhomogeneous distribution of residual stress [93]. Hence, the phase-specific stress partitioning and the plastic anisotropy in the sheet material subjected to a forming process, play a significant role in the microscopic residual-stress



concentration, which could exacerbate the cracking phenomenon. It is well known that the crystallographic texture plays an important role in the plastic anisotropy on a sheet metal. The strain-induced phase transformation can result in a textured martensite phase from an initially textured austenite phase due to the orientation relationship and the selective phase transformation mechanism [16, 37, 97-99]. For example, Cakmak et al. [16], in their high-energy synchrotron x-ray diffraction study of texture evolution in a TRIP steel, showed that the strain-induced martensitic phase transformation follows a selective phase transformation, which is closely related to stored strain energy and dislocation density of the textured austenite phase. Therefore, the plastic anisotropy can be enhanced not only by the crystallographic texture but also by the phase transformation. In addition, the grains with a preferred orientation accompany a certain stress partition based on the elastic and plastic anisotropy, and thus the texture has an effect on the orientation-specific stress distribution [100].

In the current study, we are aiming to improve the formability of advanced high-strength steels and meanwhile taking the benefit of the TRIP effect. To this end, a lean duplex TRIP SS alloy, consisting of ferrite and metastable austenite, was designed to manipulate the stress partitioning among constituent phases and the plastic anisotropy. Recently, Jung et al. [34], using a split ring test, showed that macroscopic hoop residual stresses in a deep-drawn lean duplex TRIP steel can be significantly reduced as compared to a TRIP counterpart subjected to an identical drawing ratio. However, limited studies have been conducted on the

micromechanical understanding of phase-specific residual-stress partitioning in the lean duplex TRIP steels and its effect on the formability, e.g., [35]. Moreover, cold-rolled duplex SS alloys exhibit a strong plastic anisotropy, which is governed by the strong ferritic texture [101, 102]. Moverare et al. [103] showed that the phase-specific stress distribution can be influenced by the anisotropic flow behavior in a duplex SS based on an in-situ x-ray diffraction study. It was demonstrated that the phase-specific stresses vary with the changes in the loading direction (LD) with respect to the plate orientation, showing that the crystallographic texture plays an important role in the stress partitioning behavior. Therefore, it is crucial to obtain the in-depth understanding of the combinational effects of the martensitic phase transformation, stress partitioning, and texture on the phase-specific residual-stress concentration to enhance the formability of TRIP-assisted steel alloys.

In this chapter, we studied four different alloys: (1) a TRIP SS, (2) a stable austenitic SS (stable counterpart of (1)), (3) a lean duplex TRIP SS, and (4) a lean duplex stable SS (stable counterpart of (3)). Macroscopic tensile behaviors were examined along three different LDs with respect to the RD of the alloy plates at ambient temperature to study the tensile behavior and plastic anisotropy including the Lankford coefficients. The martensitic transformation kinetics and the evolutions of crystallographic texture were studied during tensile deformation using synchrotron x-ray diffraction. In-situ neutron diffraction was used to measure the evolutions of lattice strain and phase-stress partitioning during the tensile

deformation. The correlation between microstructure, martensitic phase transformation, texture evolution, and lattice strain evolution; and their correlated role in the residual-stress partitioning and plastic anisotropy is discussed. The current work provides a basic understanding of the constitutive properties of steel alloys and the relationship between the microstructural evolution associated with tensile deformation and the phase-specific stress concentration.

## **3.2 Experimental**

### ***3.2.1 Alloy design and processing***

The two key alloys prepared in this study are: (1) a TRIP SS (a metastable austenitic SS alloy and (2) a lean duplex TRIP SS (a dual-phase alloy with metastable austenite and ferrite). In order to provide non-transforming stable references for the investigation of effects of the strain-induced martensitic transformation on the residual-stress partitioning, an austenitic SS and a lean duplex SS, both with a stable austenite phase, were studied along with the two main TRIP alloys. The alloy designations and compositions are listed in Table 3.1. Cast ingots were heated to 1523 K for 3 h and hot rolled to reduce the thickness to 4 mm. Subsequently, single-phase austenitic SS alloys (TRIP and A-SS) and dual-phase lean duplex SS alloys (D-TRIP and D-SS) were solution annealed at 1323 K and 1373 K for 30 seconds, respectively, followed by a cold rolling along the previous hot rolling direction to a final thickness of 2 mm. To minimize the effect of hydrogen, its content was kept below 0.5 ppm.

Table 3.1. Chemical compositions (wt.%) of stainless steel alloys manufactured for the current study. The TRIP SS (TRIP) consists of an initially single-phase metastable austenitic SS that will go through martensitic phase transformation with applied strain. The austenitic SS (A-SS) is a stable counterpart to the TRIP alloy. The lean duplex TRIP SS (D-TRIP) consists of metastable austenite and ferrite phases, where the austenite phase will provide the TRIP effect. Finally, the lean duplex SS (D-SS) is a stable counterpart of the D-TRIP alloy.

Alloy designation	C	Si	Mn	Cr	Ni	Cu	N	Fe	H <sub>2</sub> (ppm)
TRIP SS (TRIP)	.055	.5	7.0	17.1	4.0	-	.200	Bal.	.32
Austenitic SS (A-SS)	.051	.5	1.0	17.7	12.1	3.0	.196	Bal.	.23
Lean duplex TRIP SS (D-TRIP)	.085	.5	6.2	18.9	1.1	2.6	.078	Bal.	.20
Lean duplex SS (D-SS)	.079	.5	6.0	21.0	3.5	2.5	.080	Bal.	.30

### **3.2.2 Microstructure and tensile behavior of alloy plates**

The microstructure of as-rolled alloy plates was characterized using a light optical microscopy. An etchant consisting of 60% nitric acid and 40% water was used on the mechanically polished samples. The grain morphologies of constituent phases in all four alloy plates were characterized for all three orthogonal surfaces.

Tensile samples (25 mm gauge length, 6 mm width, and 2 mm thickness) were machined by the electrical discharge machining (EDM), and were tested at a strain rate of  $6.5 \times 10^{-3}$ /s at ambient temperature using a servo hydraulic MTS load frame. An extensometer was used to measure the engineering axial strain. Tensile tests were carried out along three different loading directions (LDs), i.e.  $0^\circ$  (rolling direction, RD),  $45^\circ$  ( $45^\circ$  to the RD), and  $90^\circ$  (transverse direction, TD), to investigate the plastic anisotropy of each alloy plate. The Lankford coefficients ( $r$ -value) were also measured in the three LDs at 20% engineering strain:

$$r = \frac{\varepsilon_w}{\varepsilon_t} \quad (3.1)$$

where  $\varepsilon_w$  and  $\varepsilon_t$  are the plastic strains along the tensile sample width and thickness directions, respectively.

### **3.2.3 Phase fraction and texture measurements using S-XRD**

The evolutions of phase fraction and texture were measured as a function of tensile strain along the three LDs using high-energy synchrotron x-ray diffraction (S-XRD)

at beamline 11-ID-C, Advanced Photon Source (APS), Argonne National Laboratory (ANL). After a series of tensile tests to various engineering strain values, a rectangular pin (2 mm × 2 mm × 10 mm) was extracted from the gauge section of each deformed tensile sample using the EDM for subsequent S-XRD measurements.

One of the advantages of high-energy S-XRD technique is its high-penetration rate, and, therefore, the bulk-average microstructure information can be obtained. The x-ray beam with 0.11798 Å wavelength was collimated to 500 µm × 500 µm, which allowed us to illuminate approximately 1000 grains. The specimens were rotated around the LD from 0° to 90° with a 15° step angle to obtain sufficient accuracy in the phase fraction and texture measurements. The Perkin-Elmer area detector was used to obtain the Debye-Scherrer rings using the transmission scattering geometry. The Debye-Scherrer rings then were converted into diffraction patterns with 10° caking using the Fit2D software [104]. The Material Analysis Using Diffraction (MAUD) software [105] and the E-WIMV algorithm [106] were used for performing the Rietveld refinement to evaluate phase fraction and texture evolutions. The pole figures and orientation distribution functions (ODFs) were generated using the MTEX [107] software.

#### ***3.2.4 Lattice strain measurements using in-situ ND tensile testing***

The in-situ lattice strain evolutions of the four alloy plates were measured to investigate the micro-mechanical behavior and interactions of constituent phases during uniaxial tension at ambient temperature. Time-of-flight neutron diffraction

(ND) measurement were performed at the VULCAN beamline, Spallation Neutron Source (SNS), Oak Ridge National Laboratory (ORNL). The tensile samples were orientated at 45° with respect to the incident neutron beam so that the ND patterns with the scattering vectors both parallel and perpendicular to the LD were simultaneously recorded by two detector banks at  $\pm 90^\circ$   $2\theta$ . In-situ tensile testing was performed using a dedicated-MTS hydraulic load frame with an extensometer (12.7 mm gauge length) to measure the applied macroscopic strain. The in-situ measurement was performed under load control mode at a strain rate of  $10^{-4}$ /s. The samples initially were subject to a tensile load of 40 N (about 6 MPa engineering stress), which is considered as the load-free reference state. During a tensile testing, several unloading curves were also measured at various plastic strains to evaluate the evolution of residual-lattice strains. The VULCAN Data Reduction and Interactive Visualization (VDRIVE) software [108] was used to process raw neutron diffraction data and to convert to diffraction patterns. The d-spacings of various (*hkl*) lattice planes were obtained using the single peak fitting using the VDRIVE, and then the lattice strain for a specific (*hkl*) lattice plane ( $\epsilon_{hkl}$ ) was obtained based on the changes in diffraction peaks as a function of applied stress (or strain):

$$\epsilon_{hkl} = \frac{d_{hkl} - d_{0,hkl}}{d_{0,hkl}} \quad (3.2)$$

where  $d_{0,hkl}$  and  $d_{hkl}$  are the interplanar spacings at the load-free and the loaded states, respectively.

### 3.3 Results

#### 3.3.1 *Microstructure and constituent phases*

The microstructure of all rolled alloy plates is presented for the RD-TD cross-section, in Figure 3.1a-d. Also, the microstructural morphologies of the TRIP and D-TRIP alloys were verified by a 3D microstructural map, Figure 3.1e,f. The TRIP and A-SS alloys exhibit isotropic grain morphology and size distribution with equiaxed grains (mean size of 20  $\mu\text{m}$ ) although these alloys were operated by the rolling, Figure 3.1a,b. On the other hand, the D-TRIP and DSS show a laminar microstructure with the elongated grain morphology along RD, Figure 3.1c,d. The darker and lighter phases are the ferrite and austenite phases with mean grain sizes of 10  $\mu\text{m}$  and 20  $\mu\text{m}$ , respectively. The microstructures of TRIP and D-TRIP alloys respectively exhibit similar features of their counterparts.

Figure 3.2 shows neutron diffraction patterns of all rolled alloy plates, showing that TRIP and A-SS alloys initially consist of single FCC phase, and D-TRIP and A-SS alloys consist of both FCC and BCC phases. The volume fraction ratio of the BCC phase to the FCC phase in both D-TRIP and D-SS alloys is approximately 3:7.



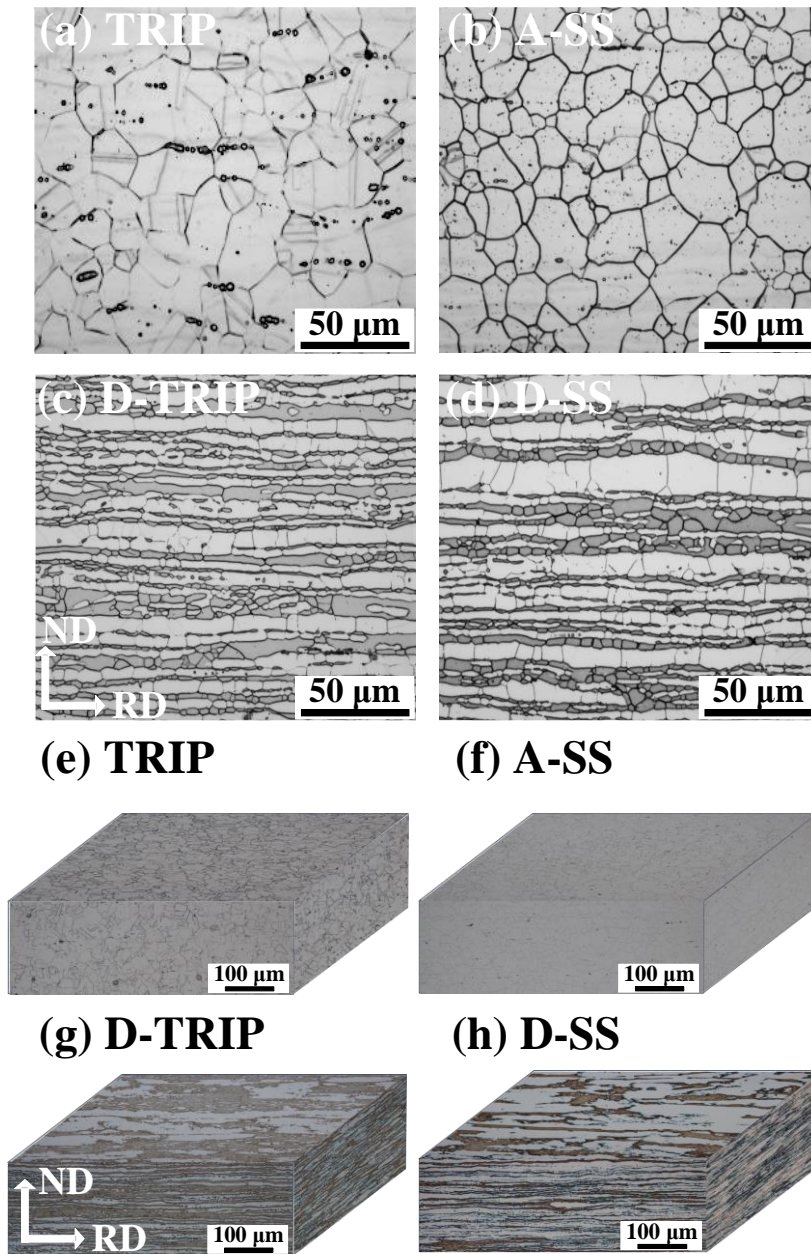


Figure 3.1. Optical micrographs of (a) TRIP, (b) A-SS, (c) D-TRIP, and (d) D-SS alloys on the RD-TD surface. 3D optical micrographs of the RD, TD, and ND surfaces of (e) TRIP, (f) A-SS, (g) D-TRIP and (h) D-SS alloys.

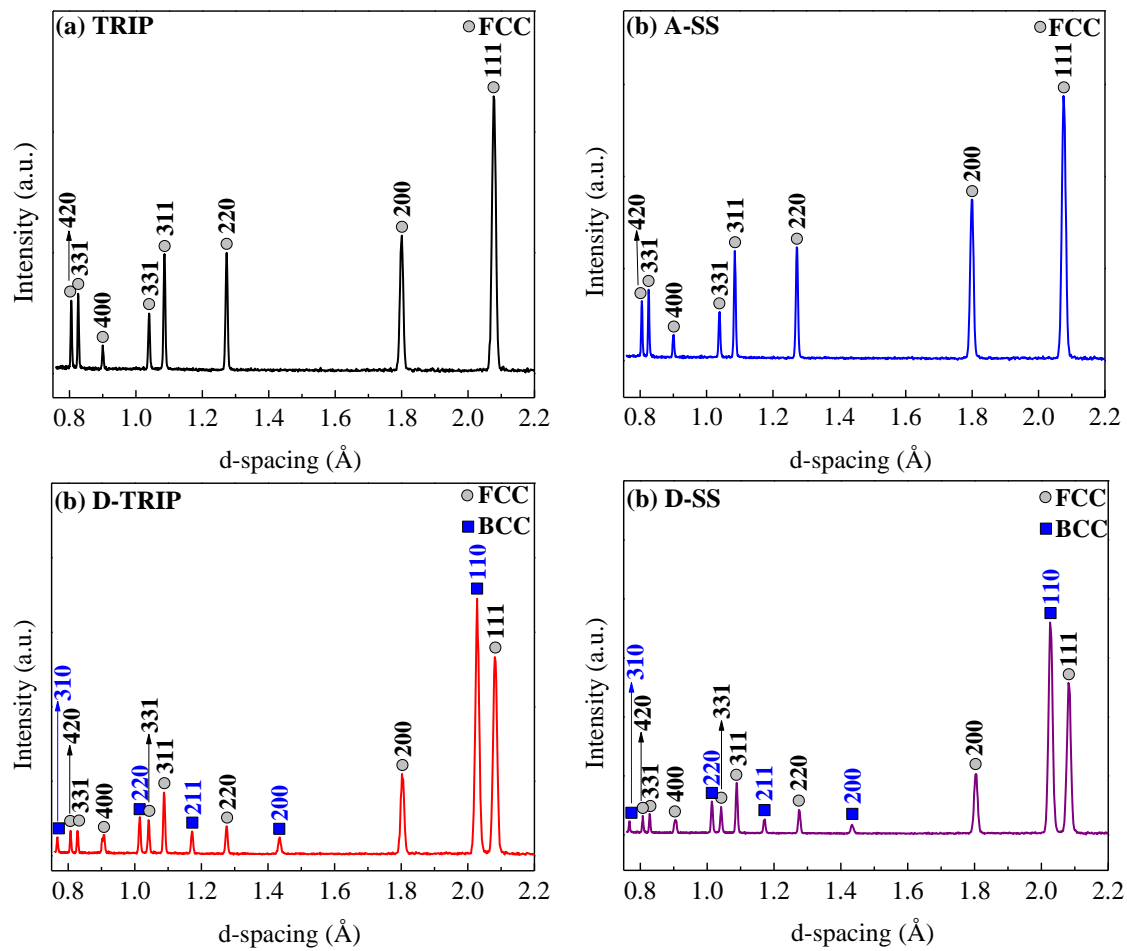


Figure 3.2. Neutron diffraction patterns of as-rolled plates measured with the scattering vector along RD for: (a) TRIP, (b) A-SS, (c) D-TRIP, and (d) D-SS.

### **3.3.2 Tensile behavior of alloy plates**

The tensile stress-strain curves were measured along different LDs ( $0^\circ$ ,  $45^\circ$ ,  $90^\circ$ ) and R-values are obtained, Figure 3.3. Key tensile properties are also summarized in Table 3.2. The stress-strain curves of all alloys showed little anisotropy as a function of LD. Hence, the stress-strain curves with LD parallel to RD in all alloys are selected for a comparison. Compared to the A-SS alloy, the TRIP alloy exhibits higher ductility and strength owing to the TRIP effect, as shown in Figure 3.3e and Table 3.2. On the other hand, the D-TRIP and D-SS alloys present comparable stress-strain curves, whereas the D-TRIP alloy with the TRIP effect provides slightly higher ductility and strength than its counterpart. Moreover, the TRIP alloy exhibits a larger elongation in contrast to the D-TRIP alloy.

Figure 3.3f shows R-values as a function of planar orientations with respect to RD. The TRIP and D-TRIP alloys both present comparable curves of R-value in contrast to their individual counterparts, suggesting that the effect of martensitic phase transformation on the R-value is not significant. The TRIP alloy shows higher R-values in all orientations as compared to the D-TRIP alloy. Moreover, the R-values in the TRIP alloy decrease almost linearly from RD to TD, whereas the inverse “V” trends are observed in the D-TRIP alloy with the maximum R-value at  $45^\circ$ . It suggests that the ferrite phase may play a significant role in the plastic anisotropy.

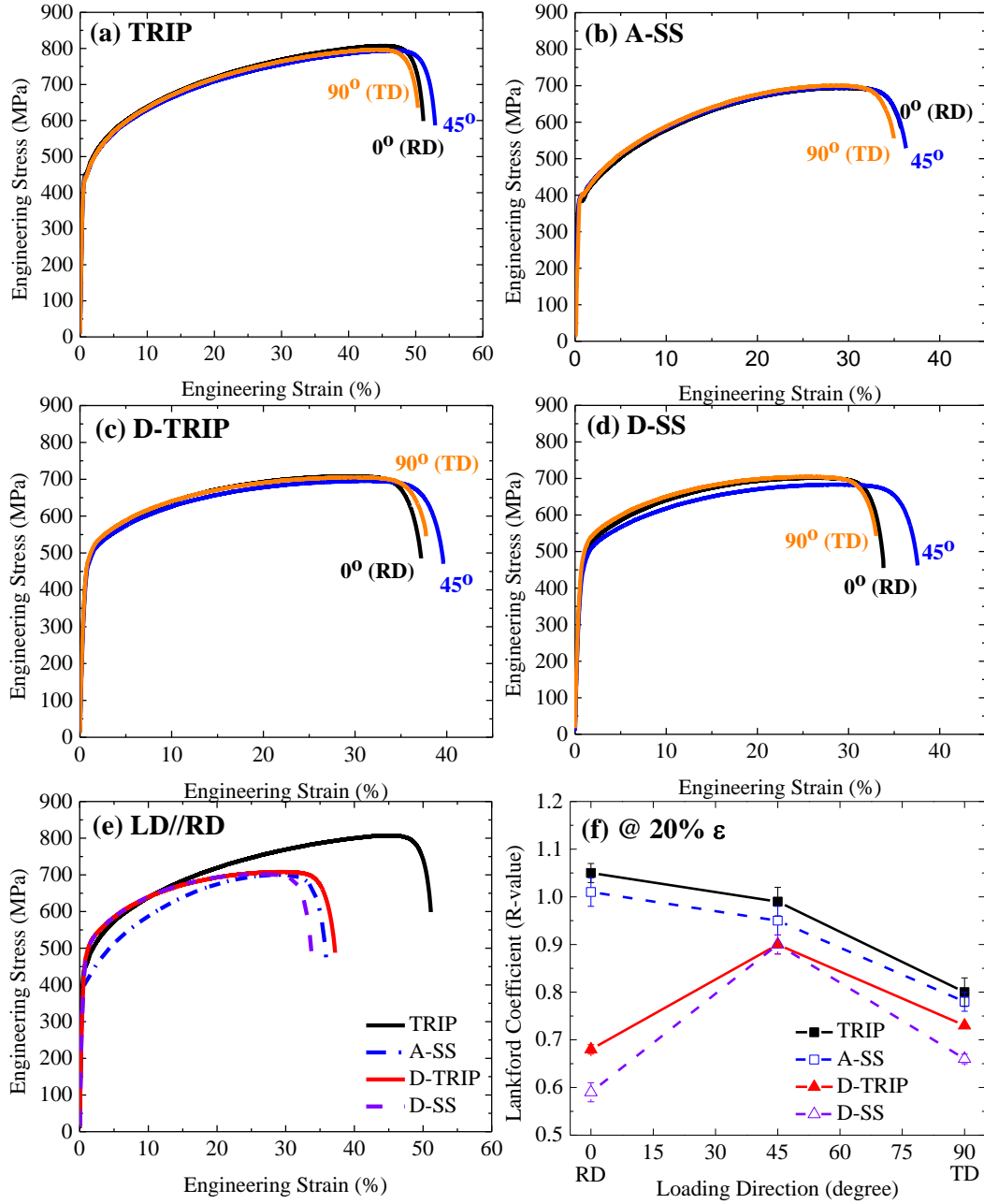


Figure 3.3. Tensile stress-strain curves of (a) TRIP, (b) A-SS, (c) D-TRIP, and (d) D-SS alloys measured as a function of the LD with respect to RD. (e) A comparison between tensile stress-strain curves of all four alloys with the LD parallel to RD. (f) R-values as a function of the angle with respect to RD for all four alloys.

Table 3.2. Tensile properties and Lanford coefficients:  $E$  is the Young's modulus,  $\sigma_y$  is the 0.2% proof stress,  $UTS$  is the tensile strength,  $\varepsilon_u$  is the total elongation, and  $\varepsilon_t$  is the total elongation.

Alloy designation	$E$ (GPa)	$\sigma_y$ (MPa)	$UTS$ (MPa)	$\varepsilon_u$ (%)	$\varepsilon_t$ (%)
TRIP SS (TRIP)	214(3)	443(4)	807	45	51
Austenitic SS (A-SS)	200(6)	406(4)	700	29	36
Lean duplex TRIP SS (D-TRIP)	203(8)	439(8)	708	29	37
Lean duplex SS (D-SS)	200(10)	432(11)	702	26	34

### ***3.3.3 Martensitic phase transformation***

The evolution of strain-induced martensite phase fraction in the TRIP and D-TRIP alloys are present in Figure 3.4. The martensitic phase transformation was not observed in the A-SS and D-SS reference alloys. As shown in Figure 3.4, the LD did not significantly influence the phase transformation kinetics in both TRIP and D-TRIP alloys. The  $\alpha'$ -martensitic transformation rate initially is higher in the D-TRIP alloy, while beyond 30% engineering strain, it saturates to 4.4 wt.%. In contrast, the phase fraction of  $\alpha'$ -martensite continues to increase almost linearly in the TRIP alloy when the engineering strain exceeds 30%. It continuously increases up to 12.1 wt.% at 50% engineering strain.

This difference in the  $\alpha'$ -martensitic phase transformation kinetics in the D-TRIP alloy would lead to a lower  $\alpha'$ -martensite fraction at higher strain, and its origin and implications will be discussed in terms of a stress partitioning in section 3.4.1. Furthermore, the strain-induced  $\epsilon$ - martensite presented in the TRIP alloy, and it initially increases rapidly to 8.5 wt.% at 40% strain, then decreases to 5.5 wt.% at 50% engineering strain. Whereas the  $\epsilon$ -martensite was not observed in the D-TRIP alloy.

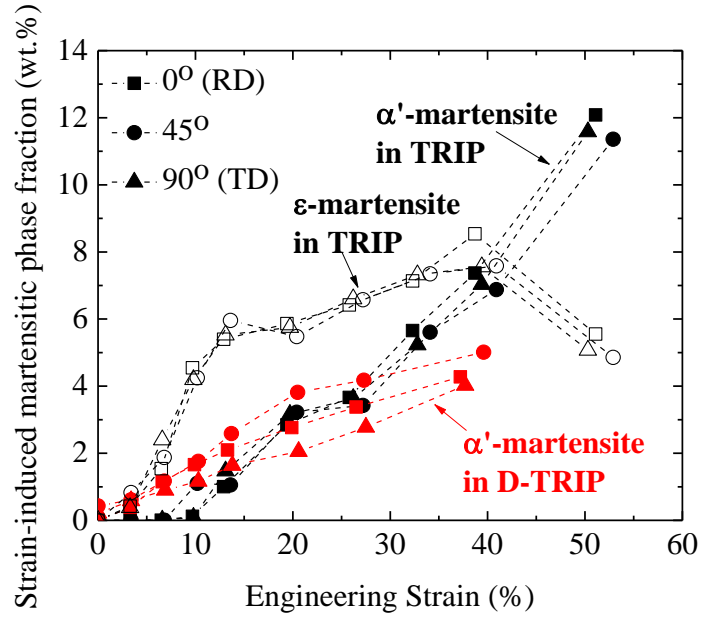


Figure 3.4. Evolution of strain-induced HCP  $\epsilon$ - and BCC  $\alpha'$ -martensite phase fractions in TRIP D- TRIP alloys measured as a function of the applied strain at three different LDs.

### 3.3.4 Texture evolution

The initial textures in FCC austenite phase are represented using ODFs at the sections of  $\varphi_2 = 0^\circ$  and  $\varphi_2 = 45^\circ$  in Figure 3.5a and b for the TRIP and A-SS alloys, respectively. The ideal components of FCC and BCC textures are summarized in Table 3.3. The TRIP alloy exhibits a weak Brass-type texture, but the A-SS alloy shows a weak Copper-type texture. On the other hand, the D-TRIP and the D-SS alloys present a similar weak  $\alpha$ -fiber texture, Figure 3.5c and d. Moreover, the initial and deformation textures as a function of LD, which were measured at 26% engineering strain, are presented using (111), (220), and (200) PFs in Figure 3.6. The comparable  $\langle 111 \rangle$  and  $\langle 100 \rangle$  fiber textures along LD, which is generally formed in FCC materials, were developed in the austenite phase in all SS alloys. The changes in texture intensity along different LDs are not significant. These results suggest that the influence of the austenitic texture in the plastic anisotropy is not significant in all rolled SS alloys, which is consistent with the result of martensitic phase transformation kinetics.

The initial BCC ferrite ODFs at section of  $\varphi_2 = 45^\circ$  of both D-TRIP and D-SS alloys are shown in Figure 3.7a and b, respectively. They show the comparable  $\alpha$ -fiber textures associated with the strong  $\{001\}\langle 110 \rangle$  component, while no typical  $\gamma$ -fiber texture was observed, which is not consistent with the rolling texture of typical BCC steel alloys. Combining with the texture results of austenite phase, it suggests that the texture of one phase is affected by the second phase in the D-TRIP and its



Table 3.3. Ideal components of FCC and BCC textures with their orientation relations with respect to the sample axes. The plane normal of  $\{hkl\}$  is parallel to the normal direction (ND), and the  $\langle uvw \rangle$  is parallel to the rolling direction (RD) of the alloy plate.

FCC		BCC	
Component	Symbol	Component	Symbol
Cube $\{001\}\langle 100 \rangle$	□	$\{001\}\langle 110 \rangle$	□
Goss $\{110\}\langle 001 \rangle$	△	$\{211\}\langle 011 \rangle$	△
Brass $\{110\}\langle 112 \rangle$	◇	$\{111\}\langle 011 \rangle$	◇
A $\{110\}\langle 111 \rangle$	○	$\{111\}\langle 112 \rangle$	○
Rotated Goss $\{110\}\langle 011 \rangle$	▽	$\{110\}\langle 110 \rangle$	+
Copper $\{112\}\langle 111 \rangle$	+		

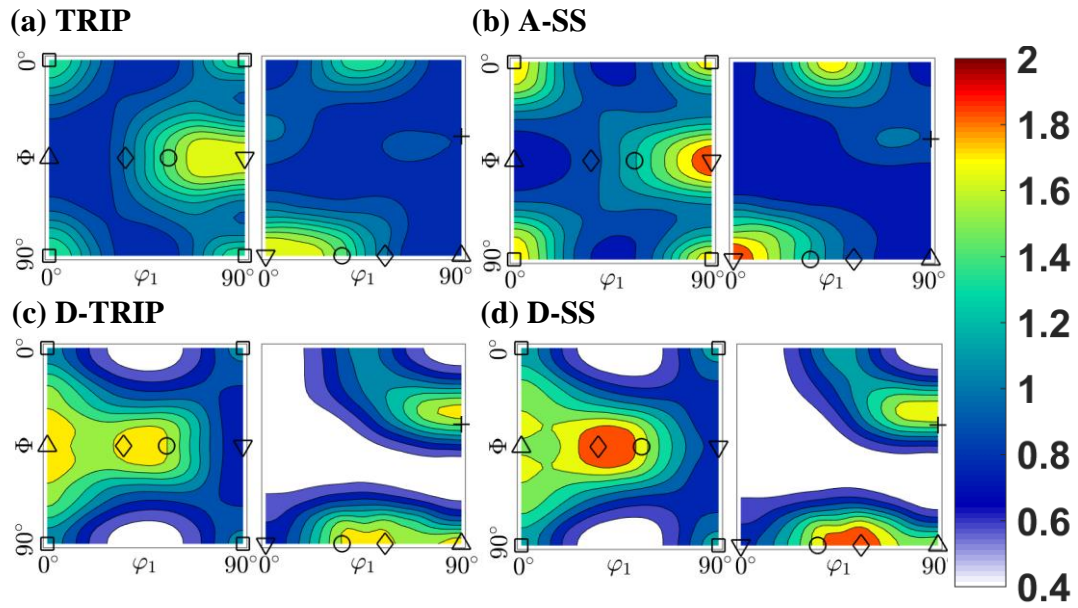


Figure 3.5. Two orientation distribution function (ODF) sections ( $\varphi_2 = 0^\circ$ ) and ( $\varphi_2 = 45^\circ$ ) showing the initial texture of the austenite phase in the as-rolled plates of (a) TRIP, (b) A-SS, (c) D-TRIP, and (d) D-SS alloys.

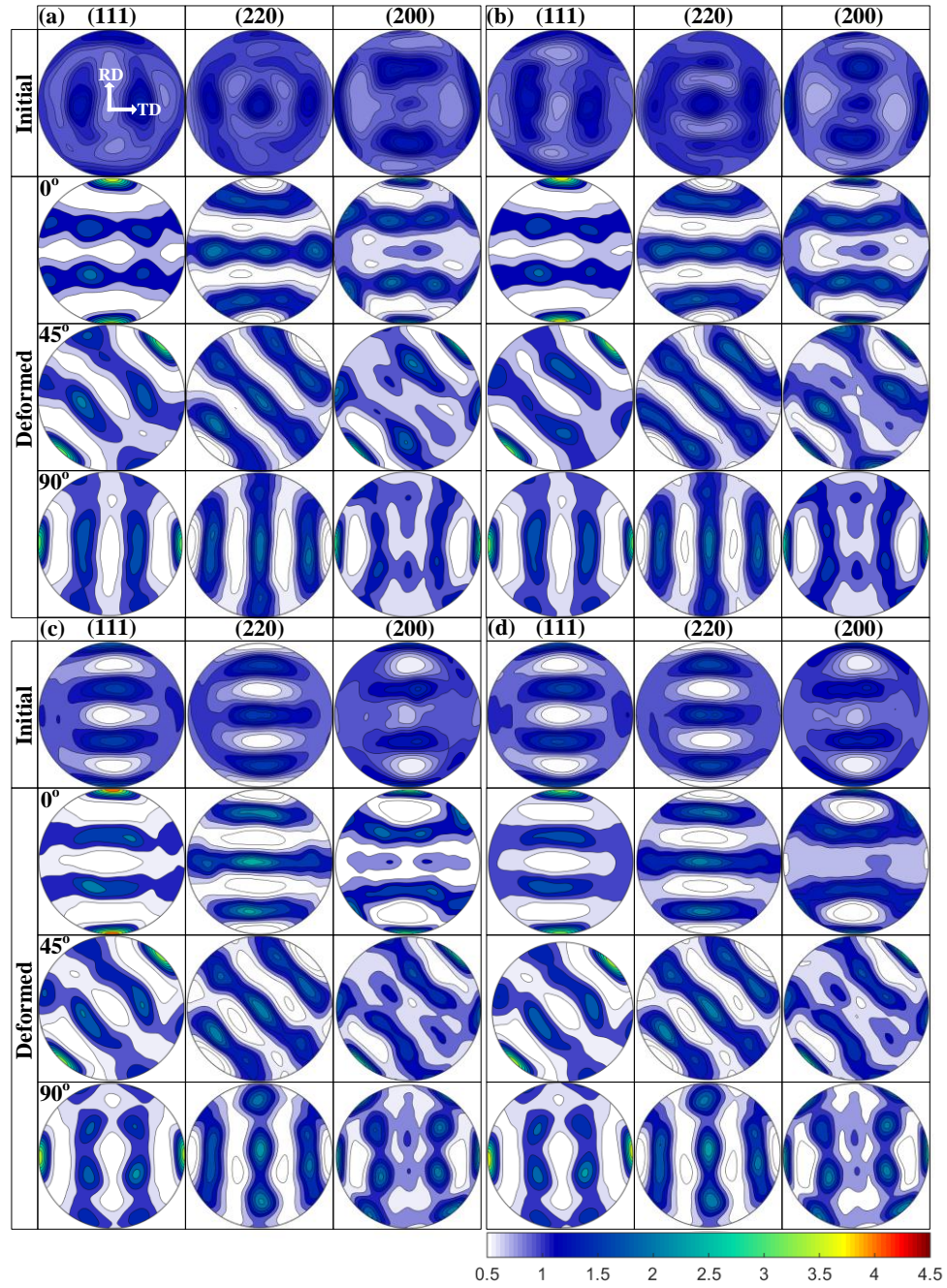


Figure 3.6. (111), (220), and (200) pole figures (PFs) of the FCC austenite phase in the as-received and tensile samples deformed (26% engineering strain) along three different LDs in (a) TRIP, (b) A-SS, (c) D-TRIP, and (d) D-SS alloys.

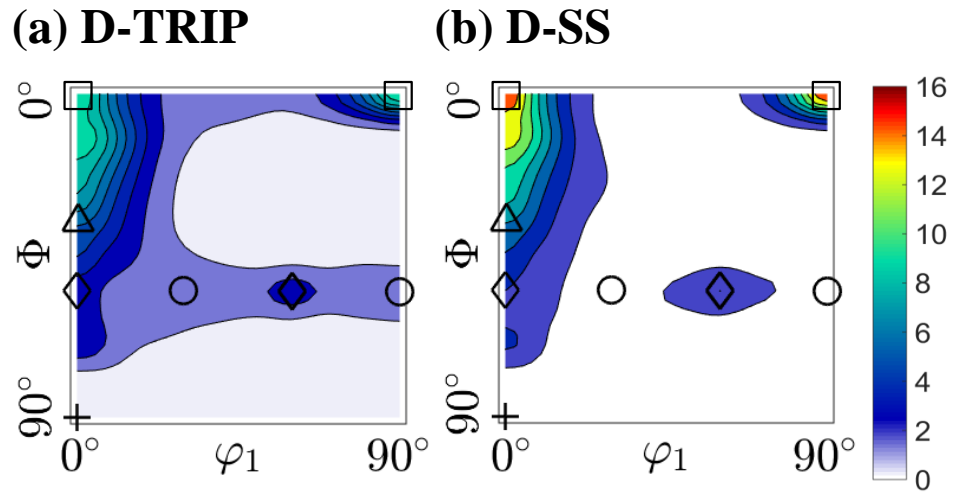


Figure 3.7. An ODF section ( $\varphi_2 = 45^\circ$ ) showing the initial texture of the ferrite phase in the as-received plates of (a) D-TRIP and (b) D-SS alloys.

reference alloys. The initial and deformation textures of the ferrite/ $\alpha'$ -martensite and ferrite phases using (222), (110), and (200) PFs, which were measured at 26% engineering strains, Figure 3.8b-d and e-g, respectively, show the  $\langle 110 \rangle$  fiber along LD. In contrast, no obvious difference between the ferrite/  $\alpha'$ -martensite and ferrite phases was observed, suggesting that the effect of martensitic phase transformation on the evolution of ferritic texture is not significant. However, the significant variation of the texture intensities along different LDs was observed after plastic deformation in both D-TRIP and D-SS alloys. These results indicate that the plastic anisotropic behavior of the D-TRIP and D-SS alloys is dominated by the strong initial textures of the laminar ferrite phase. It is consistent with the results of R-value.

Figure 3.9 present the textures of the strain-induced  $\alpha'$ -martensite phase, which were measured at 26% engineering strains, as a function of LD in the TRIP alloy. The weak  $\langle 110 \rangle$  fiber texture with relatively same intensities along different LDs is observed, further confirming that the effect of martensitic phase transformation on the plastic anisotropy is not significant.

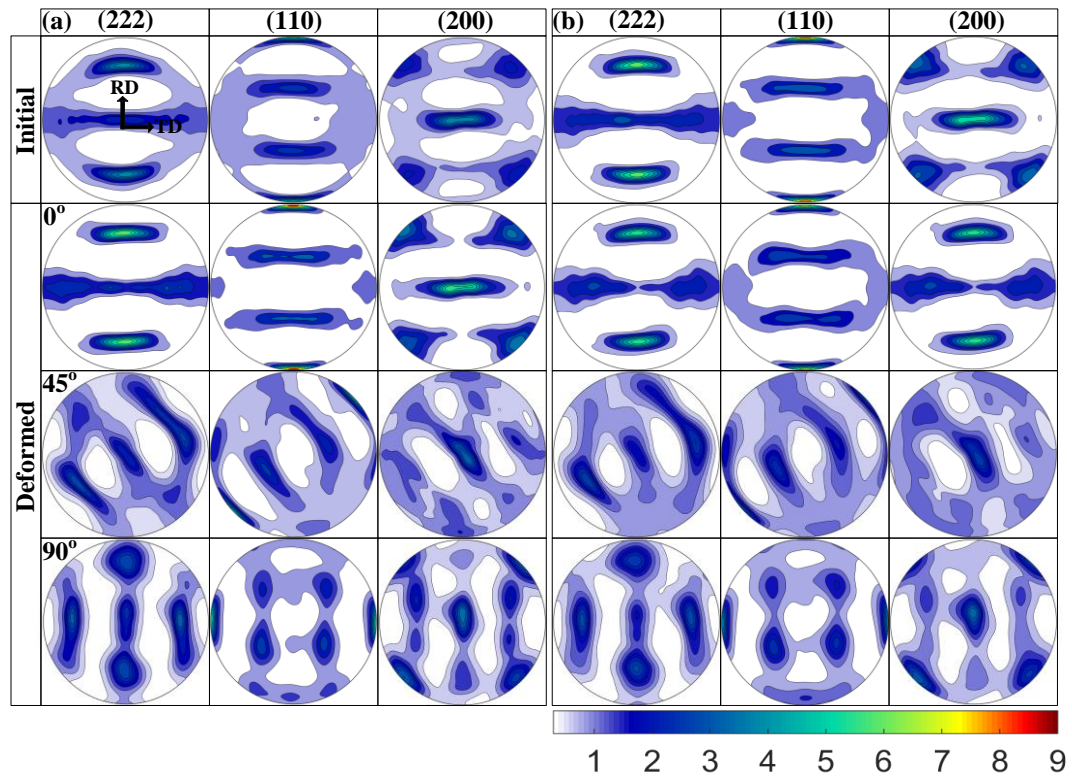


Figure 3.8. (222), (110), and (200) PFs of the BCC phases in the as-received and tensile samples deformed (26% engineering strain) along three different LDs. (a) Ferrite and  $\alpha'$ -martensite phases in D-TRIP, and (b) ferrite phase in D-SS.

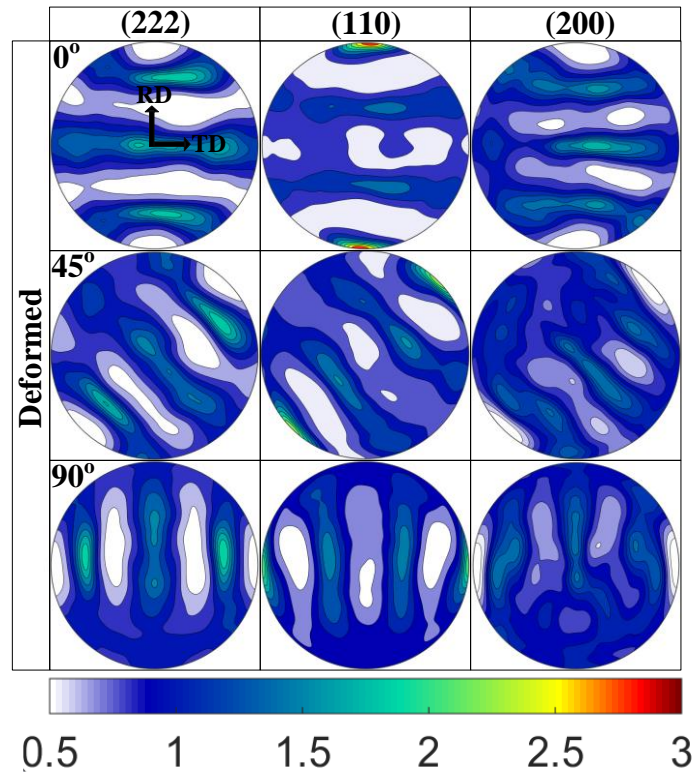


Figure 3.9. (222), (110), and (200) PFs of the strain-induced  $\alpha'$ -martensite phase in TRIP alloy deformed (26% engineering strain) along three different LDs.



### **3.3.4 Lattice strain and residual-lattice strain evolutions**

Figure 3.10a, c, and d show the evolutions of lattice strain as a function of the applied stress during tensile testing along LD for all steel alloys. In the TRIP and A-SS alloys in Figure 3.10a, three stages can be classified for the lattice strain evolution of the austenite phase. The almost linear responses of lattice strain to applied stress are observed in the stage I (0 to 300 MPa) for all the investigated ( $hkl$ ) lattice planes, showing both TRIP and A-SS alloys are in elastic region. The slopes of different lattice planes, which is attributed to the elastic anisotropy, can be measured as diffraction modulus. The (111) shows largest modulus while (200) shows lowest modulus in both TRIP and A-SS alloys, suggesting that (111) is stiffest plane while (200) is the most compliant plane. In the stage II (300 to 600 MPa), the responses of lattice strains departure from the linearity, signifying the plastic deformation in the austenite phase in both TRIP and A-SS alloys. The austenite phase plastically deforms through certain preferential slip system, and thus the sequence of yielding in oriented grains depends on their Schmid factor. This different response of lattice planes origins from the plastic anisotropy. As shown in Figure 3.10a, the slopes of the (111) and (220) lattice strains increase from the loading range of 300 to 600 MPa, suggesting that the plastic flow initiates earlier in the stiff (111) and (220) planes than the compliant (200) and (311) planes in the TRIP alloy. This phenomenon leads to the stress partitioning, e.g. the applied stresses transfer from (111) and (220) planes to (200) and (311) planes, resulting



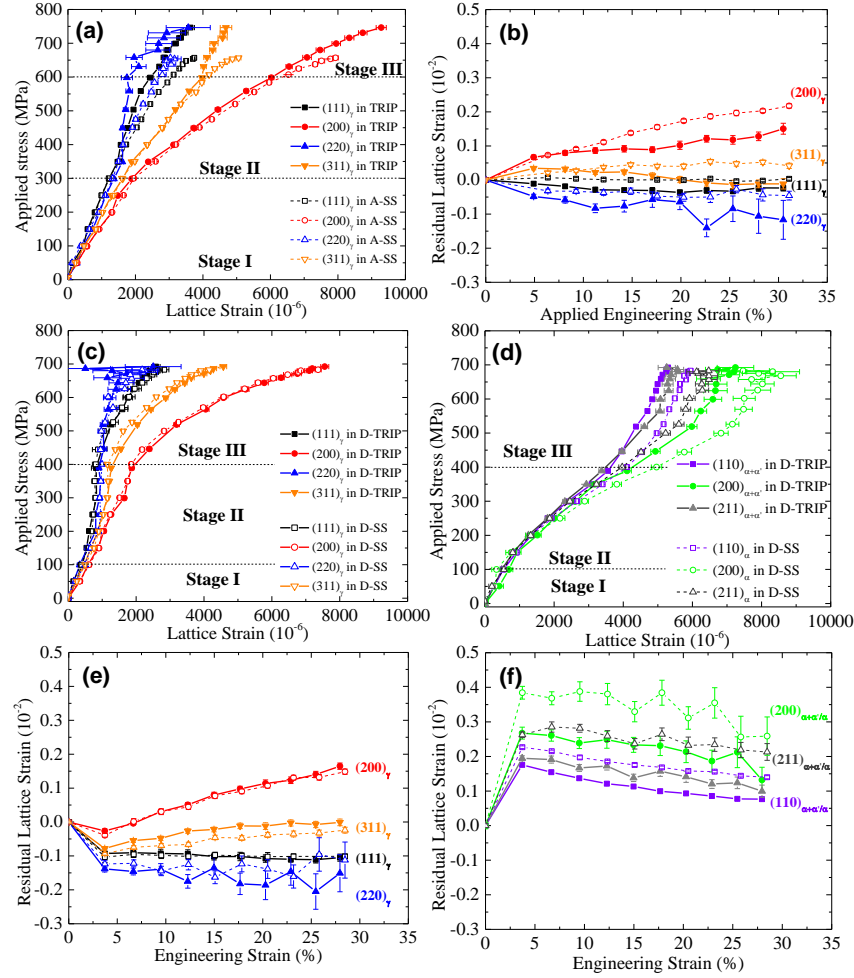


Figure 3.10. Evolutions of elastic lattice strain and residual lattice strain of (111), (200), (220), and (311) in FCC phase and (110), (200), and (211) in BCC phases measured using in-situ neutron diffraction. Elastic lattice strains as a function of the applied stress. Austenite phase in (a) TRIP and A-SS, (c) D-TRIP and D-SS, and (d) ferrite and  $\alpha'$ -martensite phases in D-TRIP and ferrite phase D-SS. Residual lattice strains as a function of the strain. Austenite phase in (b) TRIP and A-SS, (e) D-TRIP and D-SS, and (f) ferrite and  $\alpha'$ -martensite phases in D-TRIP and ferrite phase D-SS.

in the increase of the (200) and (311) lattice strains. In contrast, the lattice strain evolution of (111) and (220) planes of the austenitic SS show that the slopes are slightly lower than the TRIP alloy, suggesting that the stress accompanied by the (111) and (220) planes is higher in the A-SS alloy as compared to the TRIP alloy. In the stage III, the (311) lattice plane of the austenite phase in TRIP alloy starts to yield as the slope of lattice strain decreases, suggesting the stress transferred from the (311) austenitic grains to the other austenitic grains, resulting in the increase of the lattice strains of (111), (220), and (200) planes. In contrast, however, the (311) lattice strain of the A-SS alloy is increasing more significantly than that of the TRIP alloy. Moreover, no significant difference of lattice strain of (111), (220), and (200) planes between TRIP and A-SS alloys was observed. Note that the strain-induced martensite was formed during the plastic deformation in the TRIP alloy, suggesting that the changes in the slopes of lattice planes in the TRIP alloy is closely related to the strain-induced martensite phase.

On the other hand, the lattice strain evolutions of constituent phase of the D-TRIP and D-SS alloys are presented in Figure 3.10c and d, respectively. Since lattice parameters of ferrite and strain-induced  $\alpha'$ -martensite are very similar, the peak center for a combined profile from ferrite and strain-induced  $\alpha'$ -martensite phases is determined to evaluate lattice strain of the convoluted ferrite/martensite phase. The lattice strain evolutions also can be classified into three stages by concerning the changes in lattice strain. In the stage I (0 to 150 MPa), the lattice strains of austenite and ferrite phases all exhibit the linear response to the applied stress for

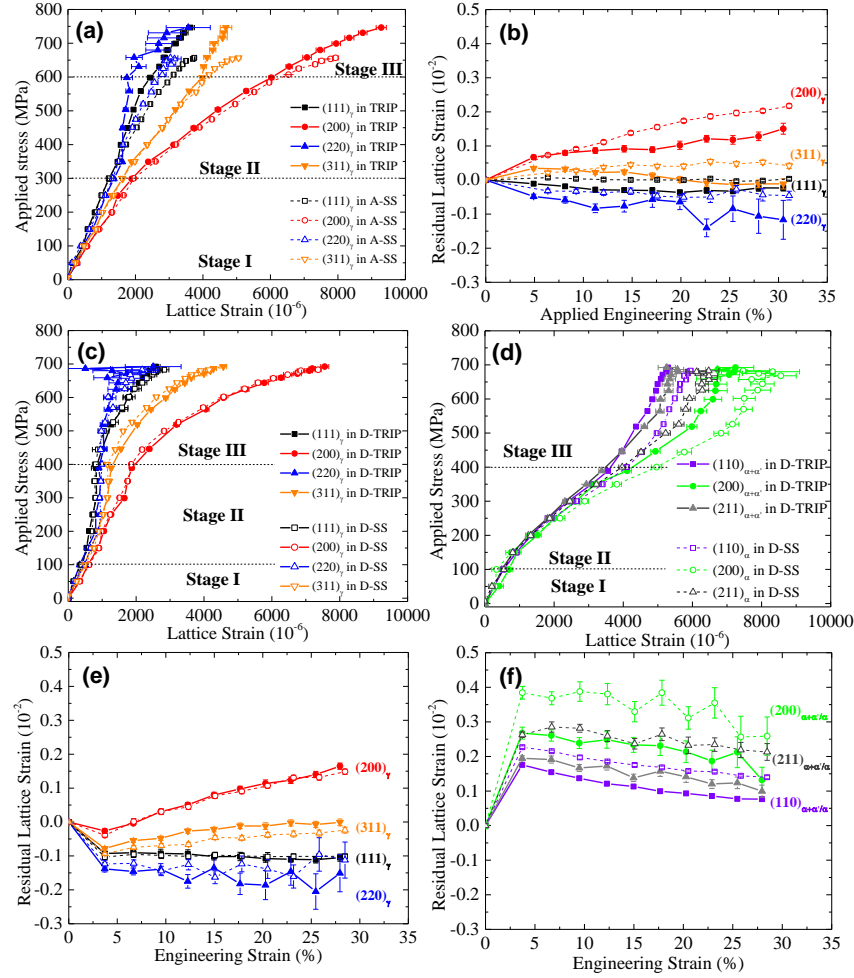


Figure 3.11. Evolutions of elastic lattice strain and residual lattice strain of (111), (200), (220), and (311) in FCC phase and (110), (200), and (211) in BCC phases measured using in-situ neutron diffraction. Elastic lattice strains as a function of the applied stress. Austenite phase in (a) TRIP and A-SS, (c) D-TRIP and D-SS, and (d) ferrite and  $\alpha'$ -martensite phases in D-TRIP and ferrite phase D-SS. Residual lattice strains as a function of the strain. Austenite phase in (b) TRIP and A-SS, (e) D-TRIP and D-SS, and (f) ferrite and  $\alpha'$ -martensite phases in D-TRIP and ferrite phase D-SS.

all investigated ( $hkl$ ) lattice planes in both D-TRIP and D-SS alloy, indicating the elastic deformation. The slopes of lattice planes in the austenite phase are higher than in the ferrite phase, suggesting that the austenite phase is stiffer than the ferrite phase in both D-TRIP and D-SS alloys. In the stage II (150 MPa to 400 MPa), the nonlinear responses of lattice strains to the applied stress in all lattice planes were observed, which is attributed to the plastic deformation. Note that although the obvious difference of the lattice strain was observed in different lattice planes, the trends of lattice strain evolution are clearly separated into two groups, i.e. FCC phase and BCC phase. The slopes of lattice strain in the austenite phase decrease, resulting in the applied stress transferred to the ferrite/ $\alpha'$ -martensite phase and ferrite phase in the D-TRIP and D-SS alloys, respectively. Accordingly, the lattice strains in the ferrite/  $\alpha'$ -martensite phase or ferrite phase increase. In the stage III (400 MPa to 700 MPa), the slopes of lattice strain in austenite phase increase, and correspondingly, the slopes of lattice strain in ferrite/  $\alpha'$ -martensite and ferrite phases decrease. It suggests that the ferrite/ $\alpha'$ -martensite or ferrite phase starts to yield for the elastic-plastic transition, in which the applied stress gradually transferred to the austenite phase. In contrast, no significant variation of the lattice strain evolution in the austenite phase for the D-TRIP and D-SS alloys was observed, indicating that the loads in the austenite phase are almost the same. However, the lattice strains of ferrite/ $\alpha'$ -martensite phase in the D-TRIP alloy are consistent lower than that of ferrite phase in the D-SS alloy in the loading range of 300 to 700 MPa, in which the  $\alpha'$ -martensitic phase transformation was taken

place in the D-TRIP alloy. This difference could be associated with the strain-induced  $\alpha'$ -martensite phase.

The neutron diffraction measurement was also performed during the unloading at several plastic strains, and the corresponding residual-lattice strain evolutions for various lattice planes in all SS alloys, respectively, are presented in Figure 3.10b, e, and f as a function of the applied plastic strain. The tensile strain was observed in the compliant (200) lattice planes, while the compressive strain was developed in the stiff (220) lattice planes in both TRIP and A-SS alloys, in Figure 3.10b. The evolutions of residual-lattice strain of the (111) and (311) lattice planes lie in the middle of that of (200) and (220) lattice planes, as the effect of intergranular stress on the lattice strain of (111) and (311) lattice planes is not significant. In contrast, the residual-lattice strain evolutions of the austenite phase reveal that the residual-lattice strains of all investigated lattice planes of the A-SS alloy are higher than the TRIP alloy during the plastic strain over 10%. It indicates that the residual stress for tensile loading of the austenite phase in the A-SS alloy is higher than that in the TRIP alloy when the plastic strain exceeds to 10%. Note that the residual-lattice strain of (311) lattice plane in the TRIP alloy initially increases and then gradually decreases along with the increase of the plastic strain as compared to the continuous increasing of the (311) residual-lattice strain in the A-SS alloy. It is consistent with the observation of the lattice strain evolution during the tensile loading, in Figure 3.10a.

Figure 3.10e and f present the residual-lattice strain evolutions of the (111), (200), (220), and (311) lattice planes in the FCC austenite phase and (110), (200), and (211) lattice planes in the BCC ferrite/ $\alpha'$ -martensite and ferrite phases in the D-TRIP and the D-SS alloys, respectively. The residual-lattice strain evolutions of the D-TRIP and D-SS alloys exhibit comparable behavior, which is consistent with the lattice strain evolutions during the loading. The trends of the residual-lattice strain of the constituent phase are clearly separated, in Figure 3.7b and c, showing that all the lattice planes of the ferrite/martensite or ferrite phase exhibits the tensile strain, but most lattice planes of the austenite phase are in the compressive strain except the (200) lattice plane. Moreover, the residual-lattice strains of all the lattice planes in each phase is approaching to each other along the increase of the plastic strain, which is consistent with the observation in stage II of the lattice strain evolution. It suggests that the phase-specific residual stress could be released in the D-TRIP and D-SS alloys during the plastic deformation. In contrast, the residual-lattice strain evolutions exhibit the similar behavior as the lattice strain evolutions, e.g. the residual-lattice strains of the austenite phases in the D-TRIP and A-SS alloys show a similar behavior, in the Figure 3.7b. The residual-lattice strains of the ferrite/ $\alpha'$ -martensite phase in the D-TRIP alloy, however, are consistently lower than that of the ferrite phase in the D-SS alloy. This result indicates that the effect of the  $\alpha'$ -martensitic phase transformation on the phase-specific residual stress is more significant in the ferrite phase than the austenite phase in the D-TRIP alloy.

### 3.4 Discussion

#### ***3.4.1 Stress partitioning and its effect on the residual-stress concentration***

It was presented in Figure 3.4 that the austenite phase in the TRIP alloy was transformed to the  $\epsilon$ -martensite and  $\alpha'$ -martensite phases during the tensile loading due to its low stacking fault energy, whereas no phase transformation was observed in the A-SS alloy. Therefore, it is expected that the stress partitioning among constituent phase, which exhibit phase-specific mechanical properties, could take place in the TRIP alloy during the deformation, resulting in the phase-specific residual-stress concentration at unloading state. As shown in Figure 3.10a, the significant difference between the TRIP and A-SS alloys was observed in the (111) and (220) lattice planes at the stress range of 400 to 600 MPa, in which the austenite phase of TRIP alloy was transferred to the  $\epsilon$ -martensite phase. Based on the single-phase microstructure of the A-SS alloy, those results indicate that the stresses of (111) and (220) lattice planes of the TRIP alloy transferred to the new-formed  $\epsilon$ -martensite phase, resulting in the increase of the interplanar distance (d-spacing) of the  $\epsilon$ -martensite phase during loading range of 400 to 600 MPa, in Figure 3.11. Nevertheless, no significant difference of (311) and (200) lattice strains between the TRIP and A-SS alloys was observed at the stress range of 400 to 600 MPa, indicating that the stresses of (311) and (200) lattice planes are approximately same in those two materials. Furthermore, it has been reported that the (311) lattice plane is weakly influenced by the intergranular stress in the FCC austenitic steel alloys, and thus it can be used to represent the phase strain

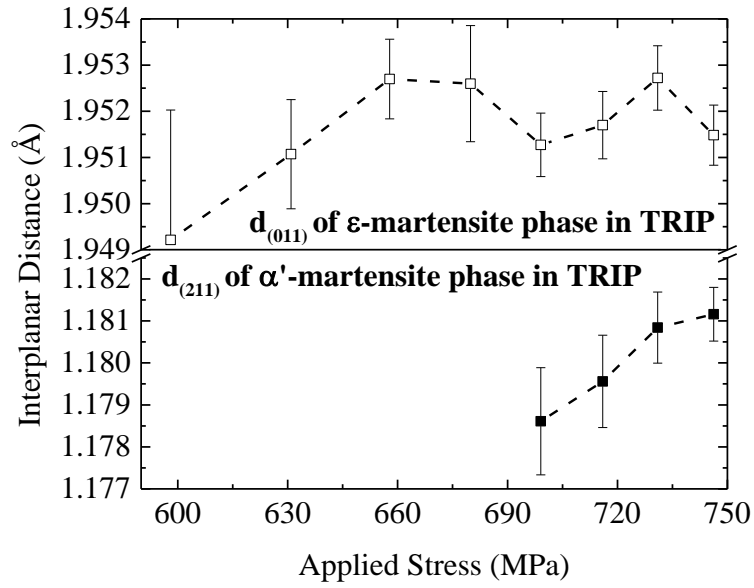


Figure 3.12. The evolutions of interplanar distance, e.g.  $d_{011}$  of strain-induced  $\epsilon$ -martensite phase and  $d_{211}$  of strain-induced  $\alpha'$ -martensite phase in TRIP alloy, as a function of applied stress.



of austenite phase. Hence, although the local-stress partitioning is induced by the  $\epsilon$ -martensitic phase transformation, the stress level of the austenite phase in the TRIP alloy is not significantly affected by the  $\epsilon$ -martensite phase. It is consistent with the conclusion by Tao et al. [17], that the stress partitioning induced by the strain-induced  $\epsilon$ -martensite phase, which weakly bears the substantial load in the TRIP steel, is not significant. As a result, it is expected that the effect of  $\epsilon$ -martensite phase on the phase-specific residual-stress concentration is not significant. However, the slope of (311) lattice strain in the TRIP alloy is significant higher as compared to the A-SS alloy when the applied stress exceeded 600 MPa, in Figure 3.10. Moreover, the slope of (200) lattice strain in the TRIP alloy is slightly higher than that in the A-SS alloy. Those slope changes in the lattice strain evolutions indicate the stress of the austenite phase in the TRIP alloy transferred to the new-formed  $\alpha'$ -martensite phase at the stress range of 600 to 750 MPa. Moreover, as shown in Figure 3.11, the d-spacing of the  $\epsilon$ -martensite phase initially decreases and then increases when the formation of  $\alpha'$ -martensite takes place, indicating that the stress of the  $\epsilon$ -martensite phase initially was released and transferred to the  $\alpha'$ -martensite phase. As a result, the d-spacing of the  $\alpha'$ -martensite phase is increasing along the increase of plastic strain, in Figure 3.11. Note that the lattice strains of (220) and (311) lattice planes in the TRIP alloy exhibit the serrated behavior, as compared to the A-SS alloy, Figure 3.10a. This behavior may result from the fact that the  $\alpha'$ -martensite transformation is a dynamic process in which the level of stress is locally different in newly-formed  $\alpha'$ -martensite and early-formed  $\alpha'$ -martensite [109]. Therefore, the strain-induced  $\alpha'$ -martensite

phase leads to a significant stress partitioning among constituent phase in the TRIP alloy during the tensile loading. Subsequently, it results in the tensile residual stress in the  $\alpha'$ -martensite phase, leading to the lower residual-lattice strains of the austenite phase in the TRIP alloy as compared to the A-SS alloy at the strain range of 10% to 30%, in Figure 3.10b.

On the other hand, it was shown in Figure 3.10c and d that the stress partitioning among constituent phase was occurring in the D-TRIP and D-SS alloy during the deformation, e.g. the yielding initiates in the austenite phase, resulting in the flow stress transferring to the ferrite/ $\alpha'$ -martensite or ferrite phases. This result suggests that the critical resolved stress of the ferrite phase is higher than the austenite phase in the D-TRIP and D-SS alloys. It has been reported that the nitrogen, which acts as the interstitial element, plays an essential role on the strengthening of austenite phase and determines relative strength between the austenite and ferrite phases in duplex steel alloys [85, 103, 110-112]. For example, Foct et al. [110] proposed that the ferrite phase in the duplex steels is harder than the austenite phase when the content of nitrogen is less than 0.12 wt.% if their grain sizes are similar. In the current study, both D-TRIP D-SS alloys contain 0.08 wt.% nitrogen, and in addition to this, the ferrite phase has smaller grain size than the austenite phase, as shown in Figure 3.1, suggesting the less strengthening in the austenite phase. Hence, the ferrite phase accumulates more lattice strain and bears higher applied stress than the austenite phase in both D-TRIP and D-SS alloys during the deformation. Subsequently, it leads to the tensile residual-lattice strain in the ferrite

phase, while the compressive residual-lattice strain in the austenite phase, as shown in Figure 3.10e, f. Furthermore, Figure 3.4 reveals that the D-TRIP alloy exhibits the lower  $\alpha'$ -martensitic transformation rate when the strain exceeds 30%, as compared to the TRIP alloy. This phenomenon is closely related to the stress partitioning due to the stress or strain level of the austenite phase being manipulated by the ferrite phase in the D-TRIP alloy. The austenite phase is promoted to deform plastically and bears relative lower stress in the D-TRIP alloy, resulting in a lower  $\alpha'$ -martensitic phase transformation rate at higher strain, and thus lower amount of strain-induced  $\alpha'$ -martensite phase, in Figure 3.4.

To understand the effect of strain-induced  $\alpha'$ -martensite phase on the phase-specific residual stress concentration in the D-TRIP alloy, the comparison of the lattice strain evolution between the D-TRIP and D-SS alloys is analyzed and shown in Figure 3.10b, c. It illustrates that the responses of lattice strain in the austenite phase are almost identical in both materials, indicating that the stresses in the austenite phase are almost same. This is consistent with the similarity observed in macroscopic stress-strain curves and the microstructures, Figure 3.1 and Figure 3.3, respectively. Nevertheless, the significant discrepancy was observed in the ferrite/ $\alpha'$ -martensite and ferrite phases, Figure 3.10c. This difference could be due to the stress partitioning induced by the strain-induced  $\alpha'$ -martensite phase in the D-TRIP alloy during the deformation. Note that the peak position of the ferrite/ $\alpha'$ -martensite phase in the D-TRIP alloy is expected to be close to the position of the ferrite phase because of the small amount of the  $\alpha'$ -martensite phase. Hence, the

lattice strain of the ferrite/ $\alpha'$ -martensite phase measured using the ND is believed to be mostly equal to the lattice strain of the ferrite phase in the D-TRIP alloy. In such a case, a portion of the applied stress could transfer from the ferrite phase to the  $\alpha'$ -martensite phase, leading to a decrease of the lattice strain of the ferrite phase in the D-TRIP alloy. However, the effect of this stress partitioning on the stress level of retained austenite phase is not significant. Note that the increment of the flow stress is mainly accumulated by the ferrite phase, rather than the austenite phase, at the loading range of 200 to 600 MPa in the D-TRIP alloy, and thus the effect of the stress partitioning induced by the new-formed  $\alpha'$ -martensite phase is more considerable on the stress level of the ferrite phase. Nevertheless, no significant variation of the lattice strain in the austenite phase between the D-TRIP and A-SS alloys was observed in Figure 3.10b at the loading range of 600 to 700 MPa, suggesting that the austenite phase, which bears a portion of the applied stress when the ferrite phase is yielding, is still unaffected by the stress partitioning of the  $\alpha'$ -martensite phase. It indicates that the strain-induced  $\alpha'$ -martensite phase is in the elastic-plastic transition, in which the  $\alpha'$ -martensite phase exhibits a similar critical resolved stress as the ferrite phase. Hence, the increment of the applied stress is mainly accumulated by the austenite phase at the loading range of 600 to 700 MPa. Moreover, the lattice strain evolutions of different lattice planes in the D-TRIP alloy exhibit similar trends as the D-SS alloy, indicating that the effect of the local-stress partitioning between the ferrite and  $\alpha'$ -martensite phases on the specific orientation of the ferrite phases is not significant.

In order to quantitatively understand the stress partitioning behavior in the TRIP and D-TRIP alloys and its effect on the residual stress concentration, the residual-lattice strains are further converted to the phase-specific residual stress using neutron diffraction elastic constants,  $E_{hkl}$  and  $\nu_{hkl}$ , obtained using the Kröner model [113]. The merit is that the continuity of strain/stress in grain boundaries is taken into account in this Kröner model [114, 115]. The parameters obtained from the Kröner model are presented in in Table 3.4. The phase-specific residual stress was calculated using the Hooke's law by assuming plane-stress condition:

$$\begin{aligned}\sigma_1 &= \frac{E_{hkl}}{1 - \nu_{hkl}^2} (\varepsilon_1^{hkl} + \nu_{hkl} \varepsilon_2^{hkl}) \\ \sigma_2 &= \frac{E_{hkl}}{1 - \nu_{hkl}^2} (\varepsilon_2^{hkl} + \nu_{hkl} \varepsilon_1^{hkl})\end{aligned}\quad (3.3)$$

where  $\sigma_1$  is the axial principal stress,  $\sigma_2$  is the transverse principal stress,  $E_{hkl}$  is the diffraction elastic modulus,  $\nu_{hkl}$  is the diffraction Poisson's ratio, and  $\varepsilon_1^{hkl}$  and  $\varepsilon_2^{hkl}$  are the measured elastic lattice strains in the axial and transverse directions, respectively. The (311) lattice plane of the austenite phase and (211) lattice plane of the ferrite/ $\alpha'$ -martensite and ferrite phases are used to calculate the residual stress per Equation 3.3, since they are not significantly influenced by the intergranular stress in FCC and BCC steel alloys, respectively. The results of the phase-specific residual stress in the A-SS and D-SS alloys, respectively, are selected as a reference of the calculation of residual stress of the  $\alpha'$ -martensite phase in the TRIP and D-TRIP alloys. The changes in the phase fraction induced

Table 3.4. Diffraction moduli,  $E_{311}$  for austenite and  $E_{211}$  for ferrite, and Poisson's ratios,  $\nu_{311}$  for austenite and  $\nu_{211}$  for ferrite, following the Kröner model.

	$E_{hkl}$ (GPa)	$\nu_{hkl}$	$C_{11}$ (GPa)	$C_{12}$ (GPa)	$C_{44}$ (GPa)
Austenite	184.1	.31	217.6	138.7	112.7
Ferrite [35]	224.4	.276	231.4	134.7	116.4

by the martensitic phase transformation with the rule of mixtures approach is taken into account. Figure 3.12a presents the phase-specific residual stresses in the TRIP alloy as a function of plastic strain, which shows that the level of residual stress in the  $\alpha'$ -martensite phase is much higher than that in the austenite phase. It demonstrates that the tensile residual stress concentrates in the  $\alpha'$ -martensite phase after the plastic deformation in the TRIP alloy. Moreover, the brittle  $\alpha'$ -martensite phase, which contains high carbon content, is more sensitive to crack than the ductile austenite phase. Hence, the premature fracture or microcrack initiation could occur preferentially in the brittle  $\alpha'$ -martensite grains or martensite grain boundaries, thus leading to the poor formability. On the other hand, the results of the phase-specific residual stress, as shown in Figure 3.12b, show that the tensile residual stress also concentrates in the  $\alpha'$ -martensite phase in the D-TRIP alloy, which is similar to the TRIP alloy. However, the deviation of the residual stress level of the  $\alpha'$ -martensite phase in the D-TRIP alloy from the TRIP alloy was observed in the Figure 3.12b. We compare the residual stress of the  $\alpha'$ -martensite phase between Figure 3.12a and b, showing a lower residual stress in the  $\alpha'$ -martensite phase in the D-TRIP alloy, as compared to the TRIP alloy. It is facilitated by the ferrite phase that shares the load and plays a beneficial role in the stress partitioning during the deformation. Hence, this load-sharing effect from the ferrite phase described herein facilitates the relaxation of residual-stress concentration in the  $\alpha'$ -martensite phase in the D-TRIP alloy.

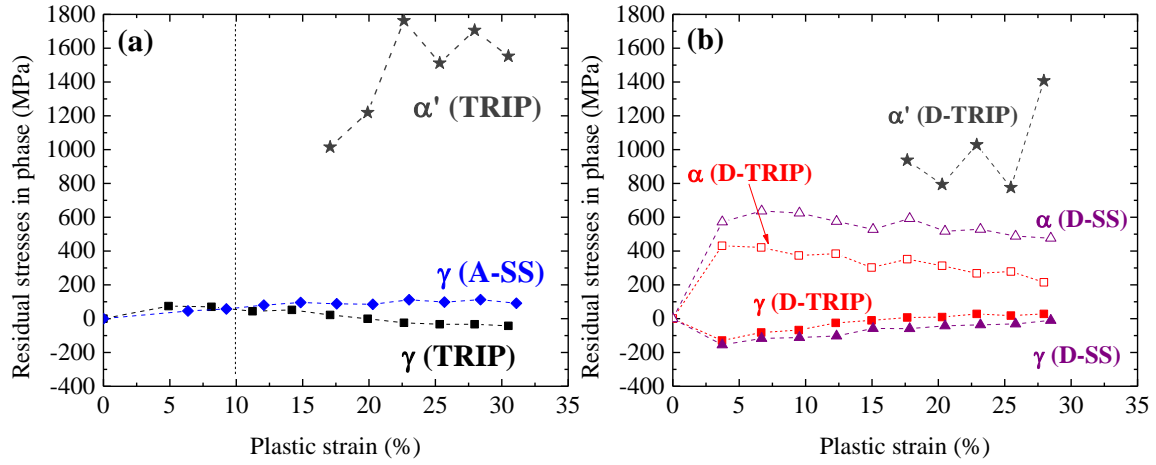


Figure 3.13. Evolutions of phase-specific residual stress measured using in-situ neutron diffraction. (a) residual stress evolutions of the austenite and  $\alpha'$ -martensite phases as a function of the applied strain in TRIP and A-SS alloys, and (b) residual stress evolutions of the austenite, ferrite, and  $\alpha'$ -martensite phases as a function of the applied strain in D-TRIP and D-SS.



### ***3.4.2 Texture evolution and its effect on the martensitic phase transformation and plastic anisotropy***

It has been demonstrated in section 3.4.1 that the  $\alpha'$ -martensite phase significantly affects the stress partitioning behavior, which results in the tensile residual-stress concentration in the  $\alpha'$ -martensite phase in both the TRIP and D-TRIP alloys. In addition, the phase fraction of the strain-induced  $\alpha'$ -martensite phase affects the mechanical properties as well as the fracture mechanism of the TRIP steel alloys. For example, the fracture of a TRIP-assisted steel alloy was investigated, using the experimental and numerical methods, showing that higher amount of the strain-induced  $\alpha'$ -martensite increases the possibility of fracture. Since it enhances the network of  $\alpha'$ -martensite, the crack propagation without crossing of the ductile phase is allowed [20]. Moreover, the martensitic phase transformation kinetics is closely related to the texture of the parent austenite phase due to the orientation relationship and the selective phase transformation mechanism, suggesting that the phase fraction of the  $\alpha'$ -martensite phase varies along with the change of texture of the austenite phase. In the current work, the dominant component of the as-received texture of the austenite phase in the TRIP alloy is the Brass, while the dominant Rotated-Goss component associated with Copper was observed in the A-SS alloy, as shown in Figure 3.5a and b. It has been reported that the high SFE can result in the Copper-type deformation texture, while low SFE can lead to the Brass-type deformation texture [116, 117], and thus the SFE is expected to be higher in the A-SS alloy than the TRIP alloy. Note that the as-received textures of both TRIP and A-SS alloys exhibit the Cube component, which is promoted by the

recrystallization [97]. Hence, the recrystallization is expected to occur in both TRIP and A-SS alloys during the hot-rolling process, leading to the disappearance of the Goss component [97]. On the other hand, the as-received textures of the austenite phase in both D-TRIP and D-SS alloys show the Goss, Brass, and Copper components, which are generally formed by the deformation in the FCC steel alloys [97], as shown in Figure 3.5c and d. Moreover, the as-received textures of the ferrite phase in both materials contain the strong  $\{001\}\langle 110 \rangle$  component and the relatively weak  $\{111\}\langle 011 \rangle$  component, in Figure 3.7. Considering the ferritic phase transformation during the hot-rolling process, the austenitic grains with the Cube component primarily transfer to the ferritic grains with  $\{001\}\langle 110 \rangle$  component [118], indicating that the austenite phase recrystallized prior to its transformation to the ferrite phase in both D-TRIP and D-SS alloys. Nevertheless, the  $\{111\}\langle 011 \rangle$  component in the as-received ferritic texture is transferred from the austenitic grains with Copper component, which originates from the deformation rather than the recrystallization [118]. Hence, the austenitic grains in the D-TRIP and D-SS alloys are partially recrystallized prior to the ferritic phase transformation during the hot-rolling process. As a result, the subsequent cold-rolling process associated with the constraint of ferrite phase on the austenite phase could lead to the deformation texture, consisting of Goss, Brass, and Copper components, in the austenite phase in the D-TRIP and D-SS alloys. It has been reported that the martensitic phase transformation prefers to occur in some austenitic grains with certain orientations, which is so called variant selection. According to the investigation on the 304 stainless steel with metastable austenite phase by

Humbert et al. [37], the strain-induced martensite phase is formed more considerably from the austenitic grains with Cube and Goss components. Hence, the austenite phase, which contain higher amount of the Cube and Goss components, could be transferred more to the martensite phase regardless of the effect of the chemical composition, which certainly accounts for the high amounts of the  $\alpha'$ -martensite phase in the TRIP alloy, as shown in Figure 3.4.

Furthermore, beside the effect of the austenitic texture on the martensitic phase transformation, the plastic anisotropy, which is closely related to the evolution of textures of the constituent phase, affects the level of stress or strain in the material as well as the constituent phase when the material is loading at different directions. Thus, it could result in the different amount of the strain-induced martensite phase. In the current study, it was present in the Figure 3.6 that the similar resultant textures of the austenite phase were observed at different LDs in both TRIP and A-SS alloys, indicating that the influence of the evolution of austenitic texture on the plastic anisotropy is limited. Consequently, it can be deduced that the effect of the plastic anisotropy on the martensitic phase transformation is not significant, which leads to the similarity of  $\alpha'$ -martensitic texture among different LDs, as shown in Figure 3.9. Those results account for the similarities of the amount of  $\alpha'$ -martensite phase and R-value along different LDs in the TRIP alloys. On the other hand, the typical  $\langle 111 \rangle$  and  $\langle 100 \rangle$  fiber austenitic textures with comparable intensities at different LDs were developed in both D-TRIP SS and D-SS alloys, suggesting that the austenite phase forms its own deformation texture, rather than

influenced by the ferrite phase. Moreover, it shows that the effect of the austenitic texture on the plastic anisotropy is not significant in both D-TRIP and D-SS alloys during tensile deformation. Nevertheless, Figure 3.8 shows that the ferritic texture gives rise to the plastic anisotropy in the D-TRIP SS and D-SS alloys, and thus it could result in the different stress levels in the ferrite phase during the deformation along different LDs. Subsequently, due to the stress partitioning behavior, the stresses accumulated by the austenite phase may vary along different LDs. It is well known that Taylor factor,  $M$ , is a measure of the relative strength required to promote and maintain plastic deformation in a certain slip system. In the other words, the grains with lower  $M$  is rotated by plastic deformation with lower strength. Moreover, the Taylor factor is influenced by the anisotropic coefficient ( $R$ -value) because of the inhomogeneity of two contractions in width and thickness directions. To understand the influence of the ferritic texture in the plastic anisotropy determining the phase-specific stress in the D-TRIP alloy, the Taylor factors of oriented grains in BCC crystals are calculated based on the octahedral slip, i.e.  $\{110\}\langle 111 \rangle$  slip system for ferrite phase, as shown in Figure 3.13a. The  $R$ -values used for this calculation in the ferrite phase are assumed as the ones measured in deformed tensile samples based on the consideration of less effect of austenitic texture on plastic anisotropy. To compare the initial texture components of the ferrite phase in the D-TRIP alloy with the Taylor factors of oriented grains in BCC crystals, the normal of  $\{hkl\}$  and the  $\langle uvw \rangle$  of the lattice plane, respectively, are parallel to the normal direction (ND) and LD of the sample, in Figure 3.13b-d. The result suggests that the yielding strength of the ferrite phase

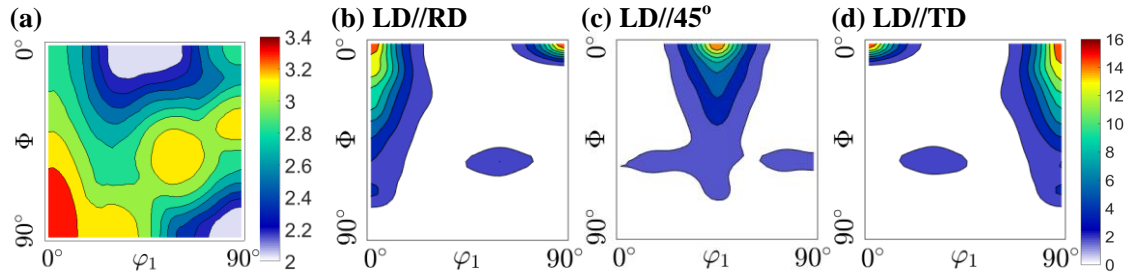


Figure 3.14. ODF section ( $\varphi_2 = 45^\circ$ ) showing (a) the Taylor factors of oriented grains in BCC crystals based on the octahedral slip, i.e.  $\{110\}\langle 111 \rangle$  slip system, and the initial texture of the ferrite phase with the normal of  $\{hkl\}$  and the  $\langle uvw \rangle$  of the lattice plane parallel to the normal direction (ND) and LD in D-SS. (b) LD parallel to RD, (c) to  $45^\circ$  with respect with RD, and (d) to TD.

is relative lower in the 45° since the texture components have lower M, and thus the austenite phase could accumulate higher stresses in the 45° during the deformation. As a result, it could promote the martensitic phase transformation and result in a higher amount of the strain-induced  $\alpha'$ -martensite phase in the 45° in the D-TRIP alloy, which is consistent with the observation that the phase fraction of  $\alpha'$ -martensite phase is slightly higher in the 45° as compared to the others. Nevertheless, the effect of the ferritic texture on the plastic anisotropy in the D-TRIP alloy is still not significant during uniaxial tensile deformation based on consideration of the similar macroscopic stress-strain curves of the D-TRIP alloys and the slightly deviation of the  $\alpha'$ -martensite phase fraction at different LDs. However, it may be reinforced at the high strain or complicated strain path and lead to the strong non-uniform distribution of  $\alpha'$ -martensite phase, which would result in the high residual-stress concentration and thereby fracture.

### **3.5 Conclusions**

The correlation of phase transformation kinetics, constituent phases, crystallographic texture, and stress partitioning between constituent phases were studied on the TRIP SS (TRIP) alloy and lean duplex TRIP SS (D-TRIP) alloy during uniaxial tension at ambient temperature to understand the constitutive behavior of steel alloys and provide a basic understanding of mechanism responsible for the formability of the TRIP-assisted steel alloys. The effect of phase transformation kinetics, constituent phases, and crystallographic texture on phase-specific stress concentration and plastic anisotropy were investigated using in-situ

neutron diffraction (ND) and synchrotron x-ray diffraction (S-XRD) techniques. The conclusions are as follows.

1. The stress partitioning between constituent phases was investigated during tensile deformation using in-situ ND. The effect of strain-induced  $\epsilon$ -martensite phase on the stress partitioning between constituent phase in the TRIP alloy is not significant. Nevertheless, the applied stresses are transferred to the strain-induced  $\alpha'$ -martensite phase, resulting in the residual stress concentration in  $\alpha'$ -martensite phase in both TRIP and D-TRIP alloys. However, owing to the local stress sharing of ferrite and  $\alpha'$ -martensite phases in the D-TRIP alloy, the residual stresses in  $\alpha'$ -martensite phase are reduced significantly during tensile deformation as compared to the TRIP alloy. Hence, the  $\alpha'$ -martensitic phase transformation, which leads to the residual-stress concentration, is the key factor determining the formability of the TRIP alloy, whereas the ferrite phase, which provides more possibilities to tailor the stress partitioning behavior, releases the residual stress concentration and thus would improve the formability of the D-TRIP alloy.

2. The austenite phase developed similar deformation textures in both TRIP and D-TRIP alloys during tensile deformation for the different loading directions (LDs), suggesting that the effect of initial austenitic texture on the plastic anisotropy is not significant. However, the significant difference in texture intensities of the ferrite phase between LDs during tensile deformation suggests that the strong initial ferritic texture is the dominant source of the plastic anisotropy in the D-TRIP alloy, which is consistent with the result of R-value, although its effect on the plastic

anisotropy is not significant in terms of tensile behavior. It is believed to be responsible for the difference of  $\alpha'$ -martensite phase fraction at different LDs. Moreover, this plastic anisotropy, which is strongly affected by the ferritic texture, could arise at high strain, and thus play an important role on the phase-specific residual stress concentration.



## **CHAPTER 4 Phase-Specific Residual Stress Partitioning and Cracking Behavior In Deep-Drawn Alloy Cups**

### **4.1 Introduction**

It is well known that the initiation of strain localization is critical to the analysis of formability of sheet metal alloys during sheet-metal forming processes [1-3]. The strain imported during the heterogeneous forming process concentrates as deformation bands of sheet metals [4, 5]. The forming limit diagram, based on the limit strains in the sheet-metal forming process, has been developed as a strain-based failure criterion to evaluate the formability of sheet metal alloys [6-11]. Mechanistic studies have been extensively reported based on the forming limit diagram [1, 12-14]. For example, A.K. Ghosh [1] and S.B. Kim et al. [12] studied the formability of advanced high-strength steel alloys using numerical analysis and experimental tensile testing, respectively. Their works show that the limit strain is closely related to the strain rate, strain hardening rate, as well as fracture elongation, and it is effectively enhanced through increasing strain hardening rate, which leads to the delayed onset of necking during the plastic deformation. The approach for improvement of formability by enhancing strain hardening rate and ductility was applied in a number of alloy design studies [15, 119, 120]. For example, Xie et al. [119] improved the strain hardening rate and ductility of CP800 high-strength steel alloy by optimizing the texture components, and in their study the formability of this high-strength steel alloy was enhanced by increasing the tensile elongation while keeping its high strength. Srivastava et al. [15], using an

optimal heat treatment on a TRIP steel alloy to improve the tensile elongation, showed that the heat-treated TRIP steel alloy exhibits higher limit strain in the forming limit curve. Due to the high tensile strength, strain hardening rate, and good ductility, the transformation induced plasticity (TRIP) steel alloys received the increasing attentions [16-19]. However, many studies have reported that TRIP steel alloys usually present cracking problem during the sheet-metal forming process at ambient temperature [20-22, 90]. It was acknowledged that this cracking problem is governed by the microstructure and its evolution of alloys during the sheet-metal forming process [20, 21, 23, 24]. Therefore, the consideration of limit strain criterion is not sufficient to provide a fundamental understanding of the underlying mechanisms responsible for the formability of steel alloys. Metallurgical studies on the microstructure-processing relationship are needed and the microstructure and its evolution during forming processes could be essential to enhance the formability of steel alloys.

Prior studies are mostly focused on the influence of initial microstructure and its evolution on the stress concentration and hydrogen embrittlement during forming processes [22, 27-30, 90]. For examples, Papula et al. [22], using Ferritescope and x-ray diffraction to study the formability of steel alloys with different stabilities of austenite phase during deep-drawing process, showed that macroscopic residual stresses increase with the increased content of strain-induced  $\alpha'$ -martensite phase. Moreover, the strain-induced  $\alpha'$ -martensite phase provides a diffusion path of hydrogen and thus facilitates the hydrogen embrittlement as the hydrogen

releasing rate is higher in bcc structure compared to fcc structure. However, in the studies of Guo et al. [33] and Jung et al. [34], it was found that metastable austenitic steel alloys exhibited the cracking phenomenon in their deep-drawn components although the content of hydrogen was controlled to be less than 0.5 ppm. In our recent experiments (in Chapter 3), a transformation-induced plasticity (TRIP) stainless steel (SS) (TRIP) alloy also shows this cracking problem during a deep-drawing process at room temperature when the hydrogen is extremely limited, as shown in Figure 4.1. Nevertheless, a lean duplex TRIP SS (D-TRIP) alloy, consisting of ferrite phase and metastable austenite phase, exhibits a better formability as compared to the TRIP alloy when they were both subjected to the deep-drawing process at 2.1 drawing ratio, in Figure 4.1. Thus, in the current study, the hydrogen embrittlement will not be a considerable factor responsible for the cracking phenomenon. The engineering stress-strain curves are presented in Figure 4.2 for the TRIP and D-TRIP alloys. TRIP alloy exhibits higher ultimate tensile strength and elongation as compared to the D-TRIP alloy. Although TRIP alloy shows an improvement of tensile properties, its formability has not been accordingly improved, in Figure 4.1. Therefore, the microstructural difference between the TRIP and D-TRIP alloys is believed to result in their distinguish performance in their deep-drawn components.

In general, the heterogeneous properties of different constituent phases in a TRIP or multiphase steel alloy can lead to the interphase stress partitioning, and thus the stress concentration. For example, Tao et al.'s in-situ neutron diffraction study

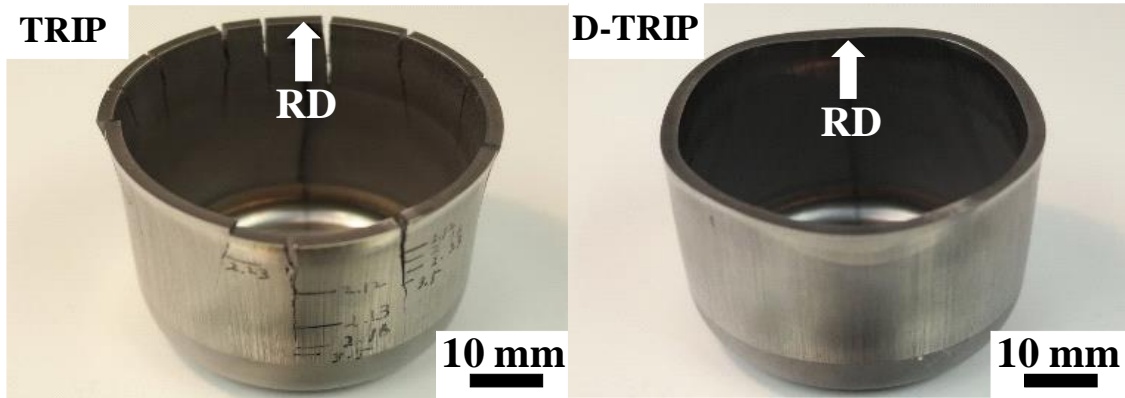


Figure 4.1. Images of deep-drawn TRIP and D-TRIP alloys at DR=2.1, showing the cracking phenomenon in deep-drawn TRIP alloy.

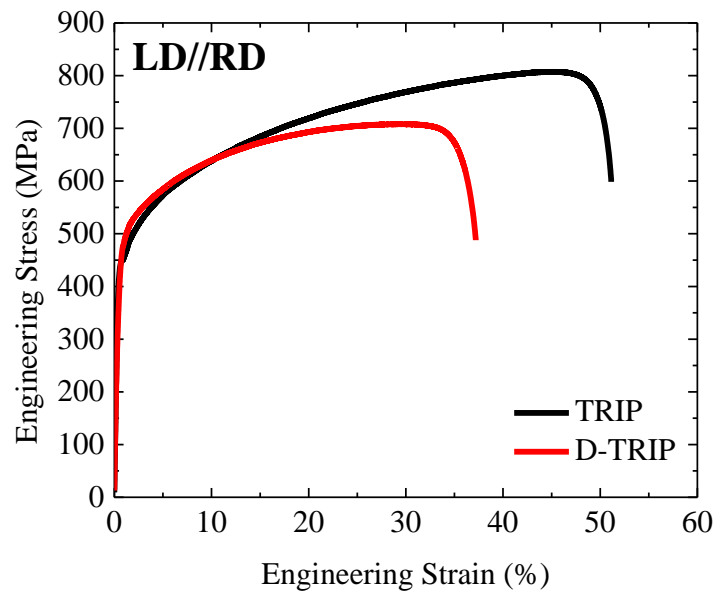


Figure 4.2. Tensile stress-strain curves of TRIP and D-TRIP alloy with the loading direction parallel to RD.

of lattice strain evolution in a 304L SS alloy showed that the applied stresses were transferred from austenite phase to strain-induced  $\alpha'$ -martensite phase when the martensitic phase transformation occurred [17]. Furthermore, the magnitude of accumulated stress in the strain-induced  $\alpha'$ -martensite phase also depends on the phase transformation kinetics, which is influenced by the crystallographic texture [16, 37]. According to the high-energy synchrotron x-ray diffraction study by Cakmak et al. [16], the selective phase transformation was observed in the martensitic phase transformation in TRIP steel alloy, resulting in the different martensitic phase transformation rate. Thus, to connect the microstructure including constituent phases, crystallographic texture, and martensitic phase transformation to the cracking behavior in deep-drawn steel alloys, the phase-specific residual stresses could be considered as a key factor for this connectivity. In general, however, conventional non-destructive approach, such as laboratory x-ray diffraction, does not provide bulk quantitative data on alloys owing to its limit penetration depth.

High-energy synchrotron x-ray diffraction (S-XRD) allowing volumetric measurement in the bulk metal has been used to study the phase-specific residual stress as well as constituent phase and texture. For example, Gnaeupel-Herold et al. [91] analyzed the through-thickness distribution of residual stress in a Al6022 deep-drawn cup and showed that the axial and hoop stresses exhibit non-linear gradients through thickness and concentrate in the outside surface. Furthermore, Jimenez-Melero et al. [121] used S-XRD to study the texture development and its

effect on the martensitic phase transformation in TRIP steel alloys. As the texture intensity in  $\langle 100 \rangle$  component increased in austenite phase, the martensitic phase transformation rate increases due to the changes in critical stress for phase transformation.

In the current chapter, we studied the combinational effect of martensitic phase transformation, constituent phases, and crystallographic texture on the phase-specific residual stress concentration to understand the mechanisms responsible for the cracking behavior in deep-drawn steel alloys. Four different stainless steel alloys, e.g. (1) a TRIP SS, (2) a stable austenitic SS (stable counterpart of (1)), (3) a lean duplex TRIP SS, and (4) a lean duplex SS (stable counterpart of (3)), were investigated on their deep-drawn cups. The formability of steel alloys were examined using deep-drawing process. The distributions of strain-induced  $\alpha'$ -martensitic phase fraction and texture measured at outside surface in tip of deep-drawn cup wall were analyzed using S-XRD. The phase-specific residual stresses were mapped in deep-drawn steel cups. The role of changes in microstructure including martensitic phase transformation and constituent phases in the phase-specific residual stress partitioning is studied. Moreover, the effect of texture on the martensitic phase transformation kinetics and its influence on the cracking behavior are discussed.

## 4.2 Experimental

### 4.2.1 Deep-drawing process

The two key stainless steel (SS) alloys prepared in the current study are: (1) a TRIP SS (a metastable austenitic SS alloy) and (2) a lean duplex TRIP SS (a duplex alloy with metastable austenite phase and ferrite phase). Moreover, an austenitic SS and a lean duplex SS were provided as non-transforming stable references for two key TRIP alloys to study the influence of the martensitic phase transformation on the cracking phenomenon in deep-drawn cups. The details of alloy designations, chemical compositions, and characterization has been reported in Chapter 3.

Deep-drawing processing was carried out to examine the sheet formability of these SS alloys by manufacturing cylindrical cups at ambient temperature. The geometries of deep-drawing tool are of 55 mm inner die diameter with 12 mm shoulder radius and 50 mm outer punch diameter with 6 mm shoulder radius and they are all axisymmetric. The surfaces of deep-drawing tools were lubricated using tallow oil. The round blank diameters varying from 90 mm, 95 mm, 100 mm, and 105 mm with 2 mm thickness were machined to provide different drawing ratio, which is defined as the following equation:

$$DR = \frac{D}{d} \quad (4.1)$$

where DR is the drawing ratio, D is the round blank diameter, and d is the outer punch diameter.

During deep-drawing process, the punch speed and the blank holder force were held as 100 mm/min and 10 KN, respectively. It should be noted that the hydrogen content was controlled to be less than 0.32 ppm during the alloy manufacturing and deep-drawing process, and thereby the hydrogen embrittlement can be neglected in the current work.

#### ***4.2.2 Phase fraction, texture, and microscopic residual stress measurements in deep-drawn SS cups using S-XRD***

High-energy synchrotron x-ray diffraction (S-XRD) measurements were performed to study constituent phase and crystallographic texture of deep-drawn SS cups at beamline 11-ID-C, Advanced Photon Source (APS), Argonne National Laboratory (ANL). The synchrotron x-ray beam has a wavelength of 0.11798 Å and was collimated to 500 µm × 500 µm for volumetric measurements. The circumferential distributions of strain-induced  $\alpha'$ -martensite phase fraction and texture at outside surface in tip of deep-drawn cup walls were measured by extracting a series of specimens as function of positions varying from rolling direction to transverse direction of deep-drawn cups at DR = 2.0. The specimens were rotated around the axial direction from 0° to 90° at 15° interval. Fit2D software [104] was used to convert the Debye-Scherrer rings into diffraction patterns. Rietveld refinements were performed for the analysis of constituent phases and texture using MAUD



[105] and E-WIMV algorithm [106]. The pole figures and inverse pole figures then were plotted using MTEX software [107].

The hoop and axial residual stresses in deep-drawn SS alloys at DR = 1.9 were analyzed using the S-XRD measurements at 1-ID-C, APS, ANL. The wavelengths of synchrotron x-ray beam were determined to be 0.1711 Å and 0.1597 Å, which can be respectively used to collect diffraction data of (311) lattice planes in austenite phase and of (211) lattice planes in ferrite or strain-induced  $\alpha'$ -martensite phase. The scattering volume was defined using conical slits with 0.02 mm width to collimate synchrotron x-ray beam into 50  $\mu\text{m}$  (hoop direction)  $\times$  50  $\mu\text{m}$  (axial direction)  $\times$  200  $\mu\text{m}$  (radial direction), allowing the through-thickness measurement, in Figure 4.3. The diffraction data were collected through the deep-drawn cup thickness at 0.5 mm interval and along the deep-drawn cup wall height from 0.5 mm below the tip at 3 mm interval. Single-peak fitting was preformed using GSAS II software [122] to obtain the d-spacing of (311) lattice planes in austenite phase and of (211) lattice planes in ferrite or strain-induced  $\alpha'$ -martensite phase. Then, the following equation was used to calculate the lattice strains:

$$\varepsilon_{hkl} = \frac{d_{hkl} - d_{0,hkl}}{d_{0,hkl}} \quad (4.2)$$

where  $d_{0,hkl}$  and  $d_{hkl}$  are the interplanar spacings at the stress-free and the stressed states, respectively. The phase-specific residual stress was calculated

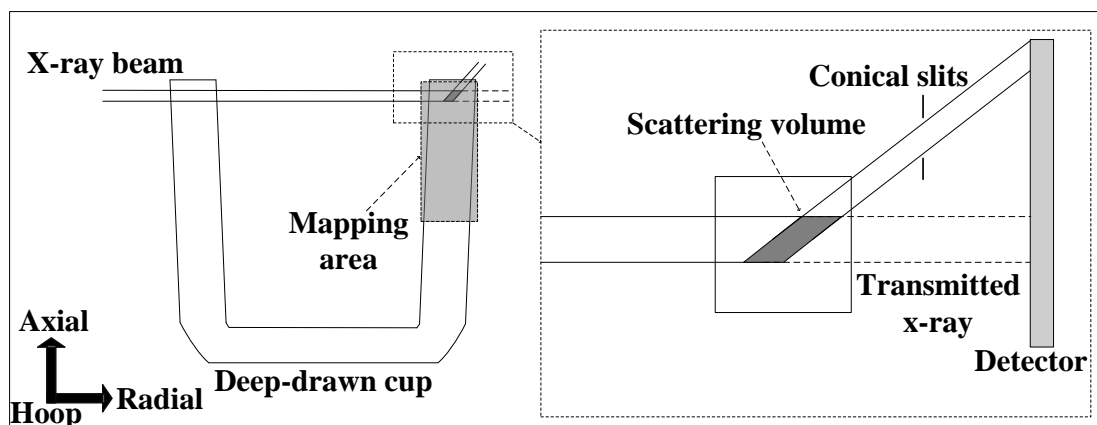


Figure 4.3. The schematics of the transmission geometry setup at 1-ID-C, APS, ANL and area mapped in deep-drawn SS cups for hoop and axial residual stress measurements using S-XRD.

according to the Hooke's law with the assumption of plane-stress condition (radial residual stress equal to zero) using the following equations [23, 27]:

$$\begin{aligned}\sigma_{hoop} &= \frac{E_{hkl}}{1 - \nu_{hkl}^2} (\varepsilon_{hoop}^{hkl} + \nu_{hkl} \varepsilon_{axial}^{hkl}) \\ \sigma_{axial} &= \frac{E_{hkl}}{1 - \nu_{hkl}^2} (\varepsilon_{axial}^{hkl} + \nu_{hkl} \varepsilon_{hoop}^{hkl})\end{aligned}\quad (4.3)$$

Where  $\sigma_{hoop}$  and  $\sigma_{axial}$  are the hoop and axial phase-specific residual stress, and  $\varepsilon_{hoop}^{hkl}$  and  $\varepsilon_{axial}^{hkl}$  are the measured elastic lattice strains in hoop and axial directions. The diffraction elastic constants, e.g. diffraction modulus  $E_{hkl}$  and diffraction Poisson's ratio  $\nu_{hkl}$  were used from our prior in-situ neutron diffraction measurement and the Kröner model [113], which has been reported detailed in Chapter 3.

## 4.3 Results

### 4.3.1 Cracking behavior in deep-drawn stainless steel alloys

The formability of stainless steel (SS) alloys are presented in Table 4.1 in terms of the number of cracks. Macroscopic cracks are observed in the deep-drawn TRIP alloy at DR = 1.9, 2.0, and 2.1, suggesting the poor formability. Cracks, which initiated at outside surface in tip of deep-drawn cup wall, propagated from outside surface to inside surface and subsequently went down vertically along the deep-drawn cup wall height. Furthermore, the circumferential crack length measured in deep-drawn TRIP alloy at DR = 2.1 was presented in Figure 4.4 as a function of

Table 4.1. The formability of SS alloys examined using deep-drawing process as a function of drawing ratio at ambient temperature in terms of cracking phenomenon.

Stainless steel alloy	Drawing ratio (DR)		
	1.9	2.0	2.1
TRIP SS (TRIP)	1 crack	4 cracks	12 cracks
Austenitic SS (A-SS)	-	-	-
Lean duplex TRIP SS (D-TRIP)	-	-	-
Lean duplex SS (D-SS)	-	-	-

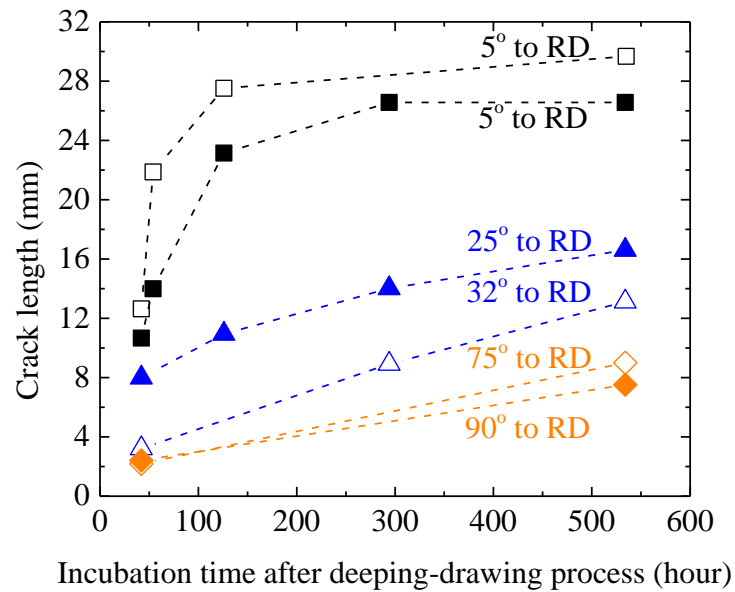


Figure 4.4. Evolution of selected crack length located at deep-drawn TRIP alloy at DR = 2.1 with respect to RD as a function of the incubation time after deep-drawing process.

incubation time. The crack length increases from rolling direction (RD) to transverse direction (TD), suggesting the crack prefers to form at RD in deep-drawn TRIP alloy. Moreover, there is no crack observed in all other deep-drawn SS alloys at all DRs, suggesting the D-TRIP alloy shows better formability than TRIP alloy.

#### ***4.3.2 Constituent phases and strain-induced $\alpha'$ -martensite phase fraction in the deep-drawn stainless steel alloys***

The diffraction patterns measured using S-XRD at outside surface of tip of deep-drawn cup walls for four SS alloys are presented in Figure 4.5. The deep-drawn TRIP alloy consists of fcc austenite phase, bcc  $\alpha'$ -martensite phase, and hcp  $\epsilon$ -martensite phase, while its stable counterpart, deep-drawn A-SS alloy, has single fcc austenite phase, in Figure 4.5a, b. Combining with our prior studies in Chapter 3 on the alloy plates, the results suggest that the martensitic phase transformation occurs in TRIP alloy during deep-drawing process. On the other hand, both deep-drawn D-TRIP and D-SS alloys show fcc phase and bcc phase in their diffraction patterns, in Figure 4.5c, d. Based on Rietveld refinement analysis, about 44 wt.% and 30 wt.% bcc phases are respectively in deep-drawn D-TRIP and D-SS alloys. It should be noted that both as-received D-TRIP and D-SS alloys have 30 wt.% bcc ferrite phase, and thereby the increase of bcc phase in deep-drawn D-TRIP alloy is generated from the martensitic phase transformation during deep-drawing process. And the A-SS and D-SS alloys as non-transforming stable references

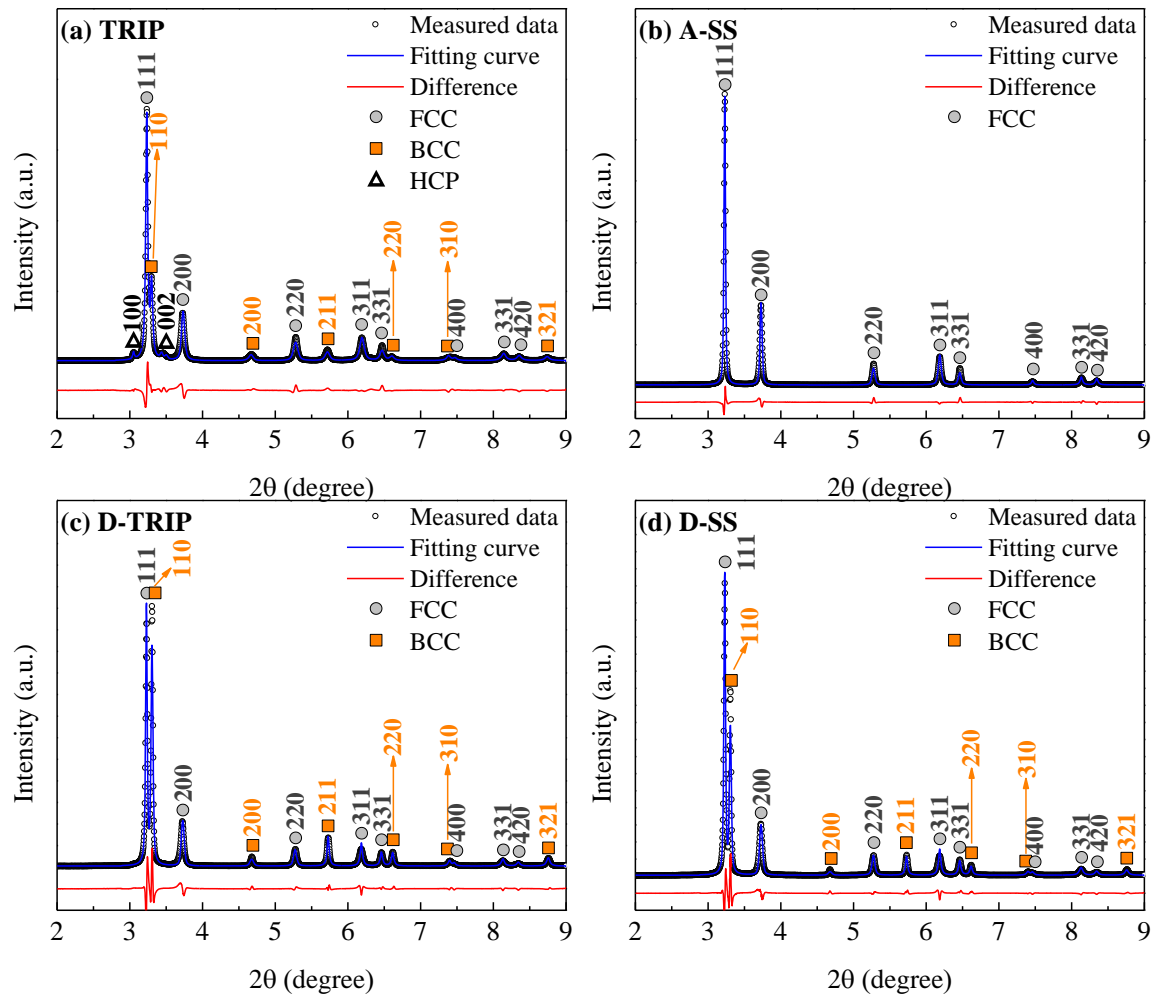


Figure 4.5. Synchrotron x-ray diffraction patterns measured at the outside surface of tip of deep-drawn SS cups wall (DR =2.0): (a) TRIP, (b) A-SS, (c) D-TRIP, and (d) D-SS.

show good agreement with the alloy designations and do not have the phase transformation during deep-drawing process.

Figure 4.6 shows the strain-induced  $\alpha'$ -martensite phase fraction as a function of orientation with respect to RD at outside surface of tip of deep-drawn cup walls for TRIP and D-TRIP alloys. It shows higher average amount of strain-induced  $\alpha'$ -martensite phase in the deep-drawn TRIP alloy as compared to that of deep-drawn D-TRIP alloy. The distribution of  $\alpha'$ -martensite phase is observed to be inhomogeneous in both deep-drawn TRIP and D-TRIP alloys due to the nonuniform plastic deformation during the deep-drawing process. In deep-drawn TRIP alloy, the  $\alpha'$ -martensite phase fraction decreases slightly from RD to TD. On the other hand,  $\alpha'$ -martensite phase fraction increases from RD to  $45^\circ$  then decreases slightly to TD in deep-drawn D-TRIP alloy. Comparison of distribution of  $\alpha'$ -martensite phase fraction, in Figure 4.6, and initial propagating rate of cracks, in Figure 4.4, for deep-drawn TRIP alloy shows the same trend, suggesting that the amount of strain-induced  $\alpha'$ -martensite phase could be closely related to the anisotropic cracking behavior during the deep-drawing process.

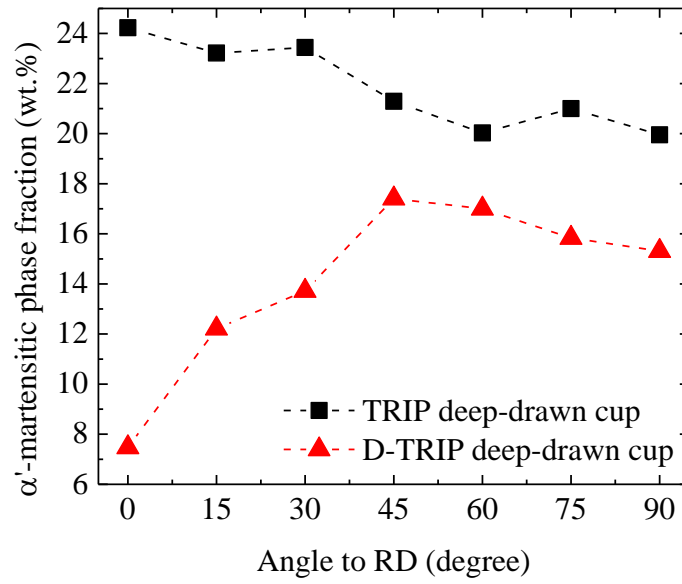


Figure 4.6. Evolutions of strain-induced  $\alpha'$ -martensite phase fraction measured at the outside surface of tip of deep-drawn TRIP and D-TRIP cups wall (DR = 2.0) using S-XRD as a function of orientation with respect to RD.



### **4.3.3 Textures in the deep-drawn stainless steel cups**

The crystallographic texture analysis was conducted using the diffraction patterns measured by S-XRD and pole figures are generated for all deep-drawn alloys, as shown in Figure 4.7 to Figure 4.9. For the fcc austenite phase, the ideal fcc texture components are presented in Table 4.2 and Figure 4.7e. The (111), (220), and (200) pole figures measured at outside surface in tip of deep-drawn cup walls as shown in Figure 4.7 show that the fcc austenite phases in all deep-drawn alloys have the typical  $\langle 110 \rangle$  fiber along the hoop direction, which is ascribed to a combinational effect of strain path and active slip systems. The scale bar shows texture intensity in terms of multiple of a random distribution. Comparison of the austenite phases at different orientations for all deep-drawn SS alloys does not show significant changes in texture intensity, suggesting that the effect of texture in austenite phase on plastic anisotropy is limited. Hence, the textures in austenite phases measured at RD are selected as representative one for the texture analysis. Textures in all austenite phases primarily consist of A  $\{011\}\langle 111 \rangle$  and Goss  $\{011\}\langle 100 \rangle$  components, while Cube  $\{100\}\langle 100 \rangle$  components are weak in all austenite phases. According to the works conducted by Daniel et al. [123] for the development of texture in austenite phase, the Cube  $\{100\}\langle 100 \rangle$  component is unstable and rotating towards the Goss  $\{011\}\langle 100 \rangle$  component during deep-drawing process, which is consistent with results in Figure 4.7. Comparison of texture components in austenite phase for deep-drawn TRIP and A-SS alloys shows that the texture in austenite phase has weaker Rotated Goss  $\{110\}\langle 011 \rangle$

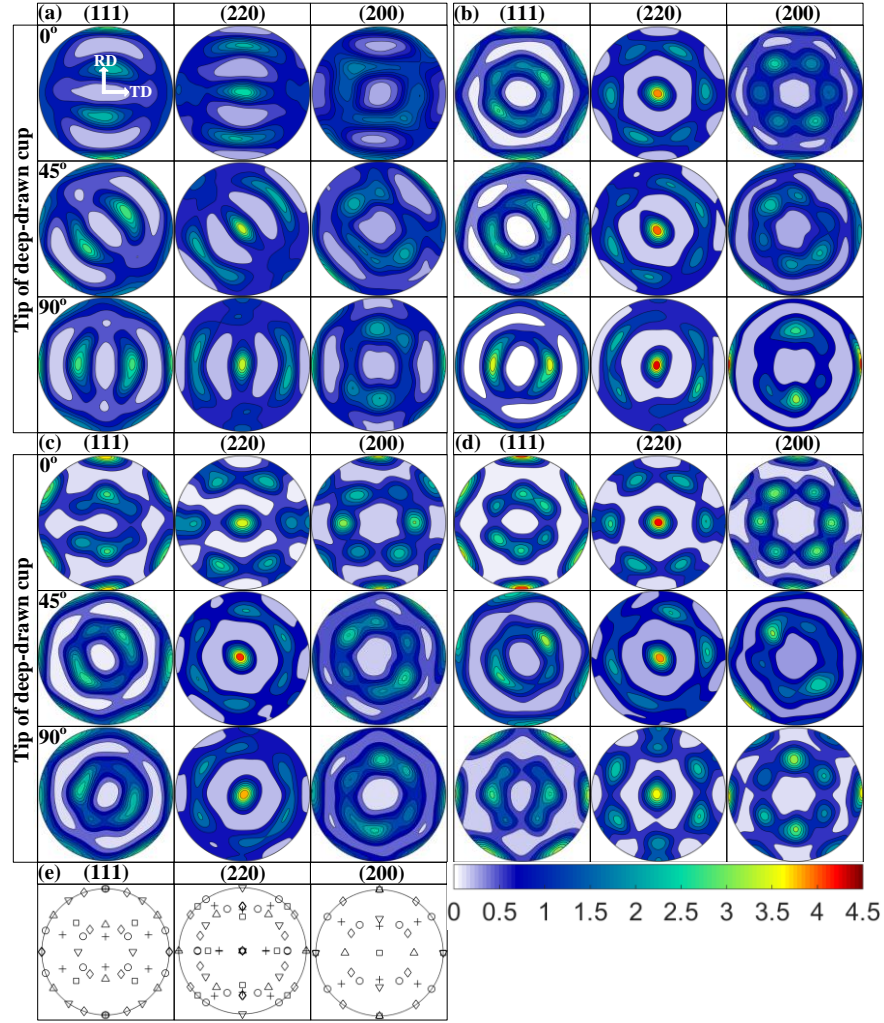


Figure 4.7. (111), (220), and (200) pole figures of fcc austenite phase measured at the outside surface of tip of deep-drawn SS cups wall (DR = 2.0) using S-XRD as a function of orientation with respect to RD: (a) TRIP, (b) A-SS, (c) D-TRIP, and (d) D-SS. Ideal components of fcc texture with their orientation relations with respect to the alloy plate axes. The plane normal of  $\{hkl\}$  is parallel to the normal direction (ND), and the  $\langle uvw \rangle$  is parallel to the rolling direction (RD) of the alloy plate.

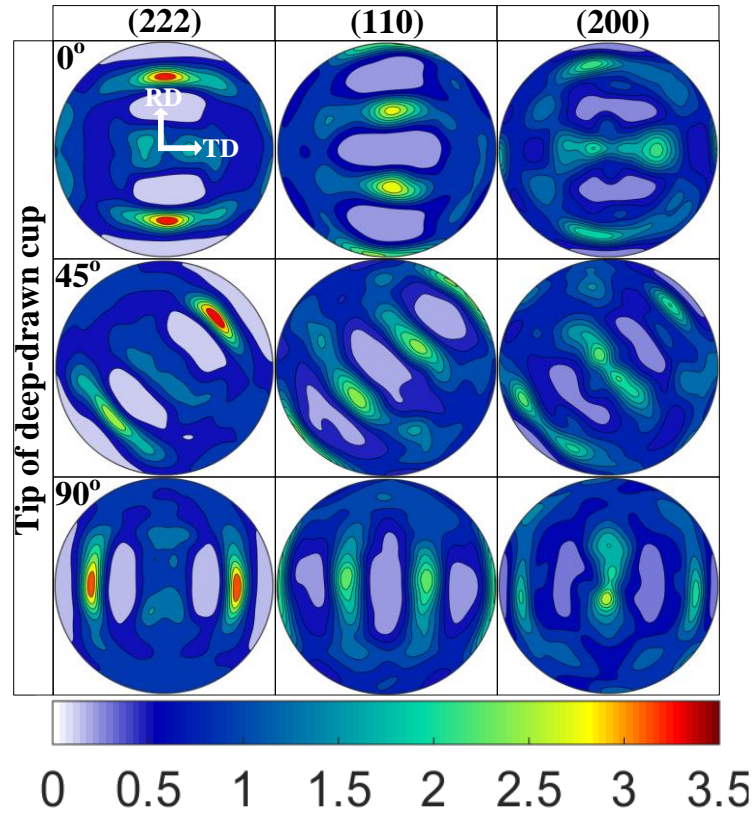


Figure 4.8. (222), (110), and (200) pole figures of the strain-induced  $\alpha'$ -martensite phase measured at the outside surface of tip of deep-drawn TRIP cup wall (DR = 2.0) using S-XRD as a function of orientation with respect to RD.

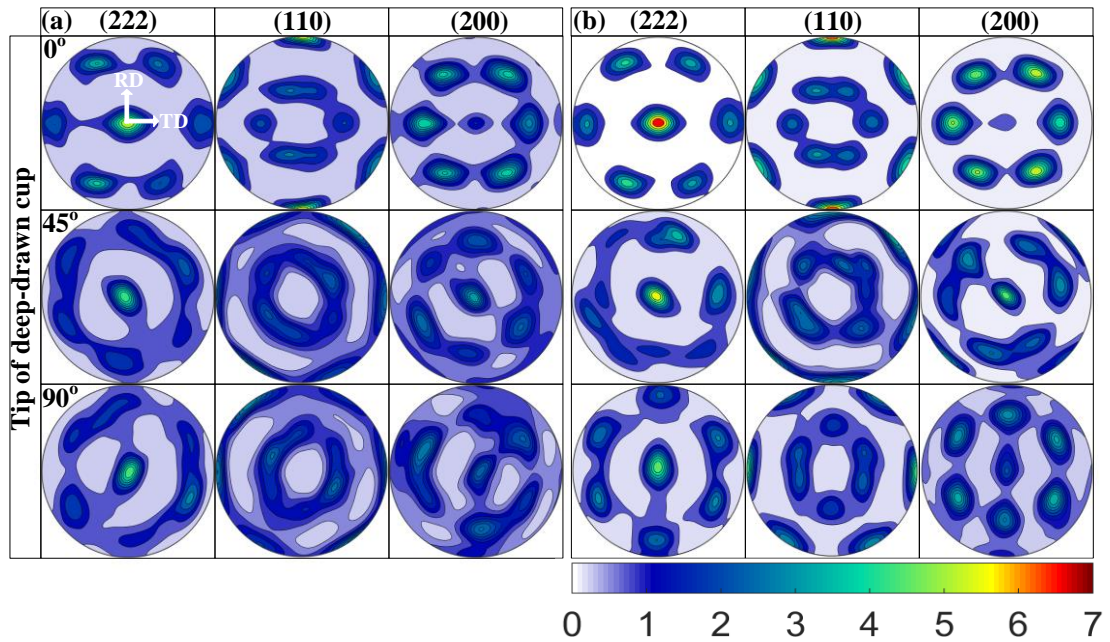


Figure 4.9. (222), (110), and (200) pole figures of bcc phases (ferrite phase and strain-induced  $\alpha'$ -martensite phase in D-TRIP; ferrite phase in D-SS) measured at the outside surface of tip of deep-drawn SS cup wall (DR = 2.0) using S-XRD as a function of orientation with respect to RD: (a) D-TRIP and (b) D-SS.

Table 4.2. Ideal components of fcc texture with their orientations relations with respect to the sample axes. The plane normal of  $\{hkl\}$  is parallel to the normal direction (ND), and the  $\langle uvw \rangle$  is parallel to the rolling direction (RD) of the alloy plate.

FCC ideal components	Symbol
Cube $\{001\}\langle 100 \rangle$	□
Goss $\{110\}\langle 001 \rangle$	△
Brass $\{110\}\langle 112 \rangle$	◇
A $\{110\}\langle 111 \rangle$	○
Rotated Goss $\{110\}\langle 011 \rangle$	▽
Copper $\{112\}\langle 111 \rangle$	+

component in deep-drawn TRIP alloy than that in deep-drawn A-SS alloy. Similarly, the Rotated Goss  $\{110\}<011>$  component in austenite phase in deep-drawn D-TRIP alloy is more random compared to that in deep-drawn D-SS alloy. These results suggest that the development of texture in austenite phase is influenced by martensitic phase transformation, which shows a preferred crystallographic direction.

For the strain-induced bcc  $\alpha'$ -martensite phase in deep-drawn TRIP alloy, (222), (110), and (220) pole figures measured at outside surface of tip of deep-drawn cup walls are presented in Figure 4.8 as a function of orientations with respect to RD. The texture in strain-induced  $\alpha'$ -martensite phase develops typical  $<111>$  and  $<100>$  fibers along the hoop direction and these fibers at different orientations are correspondingly parallel to the given orientations with respect to RD due to different strain paths during deep-drawing process. The changes in texture intensity of strain-induced  $\alpha'$ -martensite phase from RD to TD are not significant, which is consistent with the observation of change in texture intensity in parent austenite phase. It suggests that the anisotropic behavior in terms of martensitic phase transformation is not significant in TRIP alloy during deep-drawing process. It should be noted that the texture intensity of strain-induced  $\alpha'$ -martensite phase is slightly higher at RD as compared to that at other orientations, although this difference as describe earlier is limited.

For the bcc phases (strain-induced  $\alpha'$ -martensite phase and original ferrite phase in deep-drawn D-TRIP alloy; ferrite phase in deep-drawn D-SS alloy), (222), (110), and (220) pole figures measured at outside surface of tip of deep-drawn cup walls are shown in Figure 4.9 as a function of orientation with respect to RD. The textures in bcc phases are characterized as typical  $\langle 111 \rangle$  and  $\langle 100 \rangle$  fibers along the hoop direction in deep-drawn D-TRIP and D-SS alloys as well and no significant difference of texture in bcc phases in terms of texture components was observed between deep-drawn D-TRIP and D-SS alloys. The scale bar shows a strong texture intensity in bcc phases. This sharp texture in bcc ferrite phase in deep-drawn D-SS alloy suggests that the texture in bcc phases consisting of ferrite phase and strain-induced  $\alpha'$ -martensite phase in deep-drawn D-TRIP alloy primarily shows the texture in ferrite phase, while texture in strain-induced  $\alpha'$ -martensite phase could be weak. This effect of texture in bcc strain-induced  $\alpha'$ -martensite phase on texture in convoluted bcc phases also was confirmed by the fact that the texture in bcc phases of deep-drawn D-TRIP alloy is more random than that of deep-drawn D-SS alloy. Furthermore, comparison of texture intensity in bcc phases for deep-drawn D-TRIP alloy shows obvious change in texture intensity at different orientations. It is also shown that the texture intensity in bcc phases measured at RD shows highest multiple of a random distribution. These results suggest that the texture in bcc ferrite phase can be responsible for the nonuniform distribution of texture intensity in bcc phases from RD to TD.

#### ***4.3.4 Microscopic residual stresses in deep-drawn stainless steel cups***

The hoop and axial phase-specific residual stresses measured using S-XRD for all deep-drawn SS alloys are presented in Figure 4.10 and Figure 4.11 as a function of deep-drawn cup wall thickness and height, respectively. It should be noted that the A-SS alloy has single-phase (fcc austenite phase) microstructure and thus the residual stresses in austenite phase in deep-drawn A-SS alloy can be used as the estimation of macroscopic residual stresses in deep-drawn SS alloys to analyze phase-specific residual stress partitioning behavior. The hoop residual stresses are tensile stresses at outside surface and decrease almost linearly from outside surface to inside surface of all deep-drawn SS alloys, as shown in Figure 4.10. For the deep-drawn TRIP alloy, comparison of hoop residual stresses for deep-drawn TRIP and A-SS alloys show that the hoop residual stresses in deep-drawn TRIP alloy are partitioned between austenite phase and strain-induced  $\alpha'$ -martensite phase. Tensile hoop residual stresses concentrate in the strain-induced  $\alpha'$ -martensite phase at outside surface of tip of deep-drawn TRIP cup wall. The austenite phase in deep-drawn TRIP alloy shows a reduction in hoop residual stresses as compared to that in deep-drawn A-SS alloy due to the phase-specific residual stress partitioning. This result also illustrates the effect of martensitic phase transformation on the stress in austenite phase. On the other hand, the hoop residual stresses in deep-drawn D-TRIP and D-SS alloys are



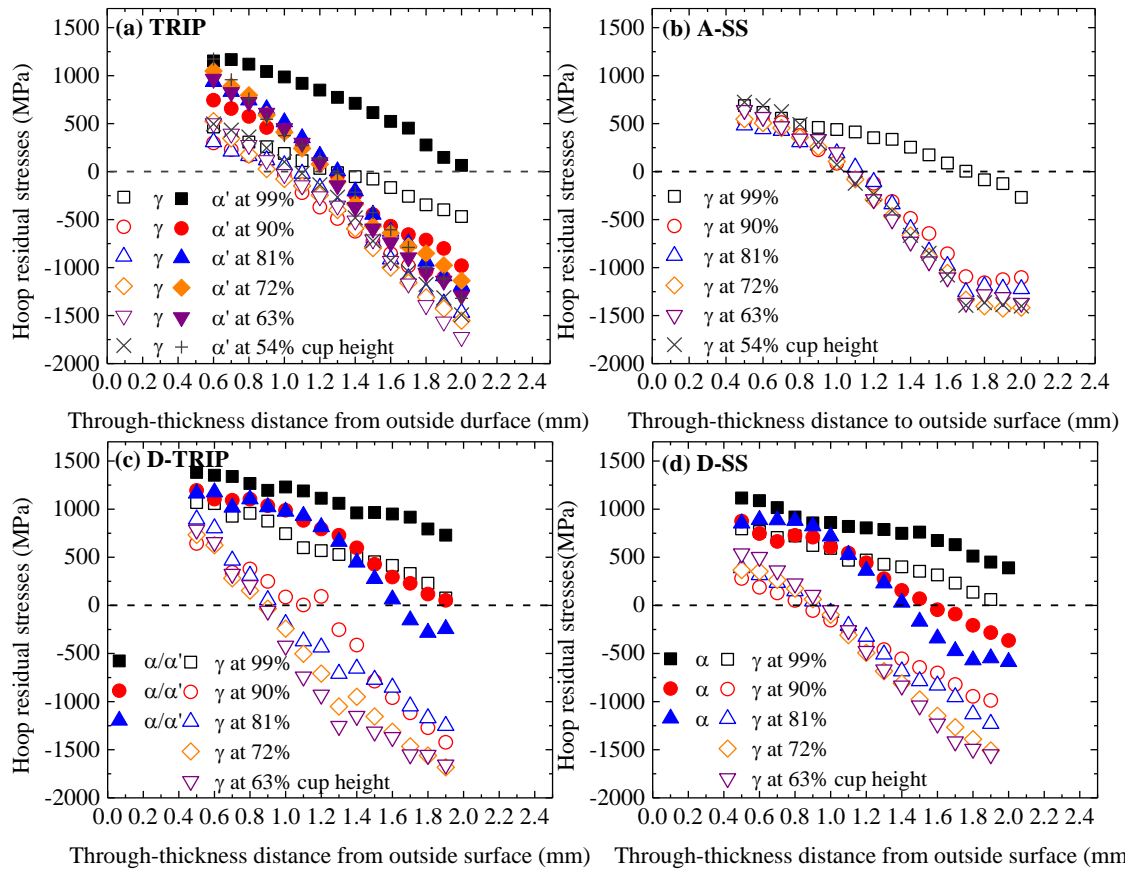


Figure 4.10. Evolutions of phase-specific hoop residual stress measured using S-XRD. (a) Hoop residual stress evolutions of the austenite and strain-induced  $\alpha'$ -martensite phases as a function of deep-drawn cup wall height and thickness in deep-drawn TRIP alloy, (b) hoop residual stress evolutions of the austenite phase as a function of deep-drawn cup wall height and thickness in deep-drawn A-SS alloy, (c) hoop residual stress evolutions of the austenite phase and bcc phases consisting of ferrite and strain-induced  $\alpha'$ -martensite phases as a function of deep-drawn cup wall height and thickness in deep-drawn D-TRIP alloy, and (d) hoop residual stress evolutions of the austenite and ferrite phases as a function of deep-drawn cup wall height and thickness in deep-drawn D-SS alloy.

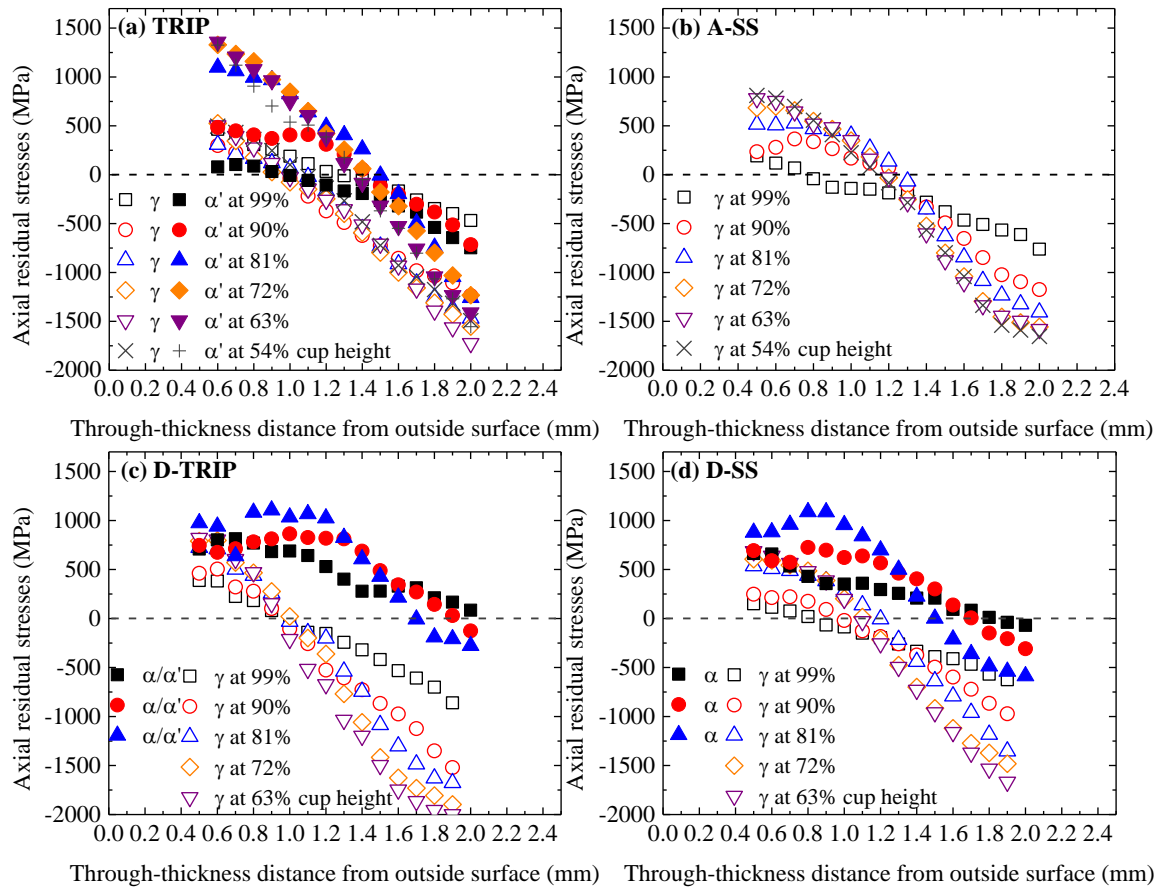


Figure 4.11. Evolutions of phase-specific axial residual stress measured using S-XRD. (a) Axial residual stress evolutions of the austenite and strain-induced  $\alpha'$ -martensite phases as a function of deep-drawn cup wall height and thickness in deep-drawn TRIP alloy, (b) axial residual stress evolutions of the austenite phase as a function of deep-drawn cup wall height and thickness in deep-drawn A-SS alloy, (c) axial residual stress evolutions of the austenite phase and bcc phases consisting of ferrite and strain-induced  $\alpha'$ -martensite phases as a function of deep-drawn cup wall height and thickness in deep-drawn D-TRIP alloy, and (d) axial residual stress evolutions of the austenite and ferrite phases as a function of deep-drawn cup wall height and thickness in deep-drawn D-SS alloy.

partitioned among constituent phases as shown in Figure 4.10c, d. The results in deep-drawn D-SS alloys show that ferrite phase has higher hoop residual stresses compared to austenite phase and the tensile hoop residual stresses concentrate in ferrite phase at outside surface of tip of deep-drawn cup wall. Comparison of hoop residual stresses for deep-drawn D-TRIP and D-SS alloys shows that bcc phases in deep-drawn D-TRIP alloy show higher hoop residual stresses than ferrite phase at corresponding locations in deep-drawn D-SS alloy, while the austenite phase for both deep-drawn D-TRIP and A-SS alloys shows similar hoop residual stresses. It suggests that martensitic phase transformation has significant effect on the hoop residual stresses in ferrite phase rather than that in austenite phase in deep-drawn D-TRIP alloy.

The phase-specific axial residual stresses measured in deep-drawn SS alloys as shown in Figure 4.11 show similar trend as the phase-specific hoop residual stresses. The axial residual stresses decrease from outside surface to inside surface of deep-drawn SS alloys. However, the deep-drawn A-SS alloy, in Figure 4.11b, shows largest tensile axial residual stress presented approximately at outside surface in the middle height of deep-drawn cup wall, suggesting that the macroscopic axial residual stresses are most severe in the middle deep-drawn cup height. Comparison of axial residual stress for deep-drawn TRIP and A-SS alloys also shows the partition in axial residual stresses for austenite phase and strain-induced  $\alpha'$ -martensite phase in deep-drawn TRIP alloy. The strain-induced  $\alpha'$ -martensite phase, in Figure 4.11a, shows higher axial residual stresses than

austenite phase and the tensile axial residual stresses concentrate in the middle height of deep-drawn TRIP alloy, which is consistent with analysis of macroscopic axial residual stress in deep-drawn A-SS alloy. It should be noted that the change in axial residual stresses measured at tip of deep-drawn cup wall for austenite phase and strain-induced  $\alpha'$ -martensite phase is not significant in TRIP alloy. Moreover, the phase-specific axial residual stresses at tip of deep-drawn cup wall are almost identical as the macroscopic axial residual stresses at corresponding locations, suggesting that the effect of martensitic phase transformation on the axial residual stress partitioning is not significant in TRIP alloy during deep-drawing process. On the other hand, the axial residual stress partitioning among constituent phases was observed in deep-drawn D-TRIP and D-SS alloys, as shown Figure 4.11c, d, and a large portion of axial residual stresses is partitioned into bcc phases, while austenite phase has a small amount of axial residual stresses. The axial residual stresses in bcc phases measured in deep-drawn D-TRIP and D-SS alloys do not concentrate at tip of deep-drawn cup wall. Comparison of axial residual stress for deep-drawn D-TRIP and D-SS alloys does not show significant difference of axial residual stress in bcc phases, while the difference of axial residual stress in fcc austenite phase was observed, specially at outside and inside surfaces of deep-drawn cup walls. It suggests that effect of martensitic phase transformation on axial residual stresses in bcc ferrite phase is not significant in D-TRIP alloy during deep-drawing process.

## 4.4 Discussion

### ***4.4.1 Effect of martensitic phase transformation and constituent phases on phase-specific stress concentration in deep-drawn stainless steel alloys***

It is evident that martensitic phase transformation occurs in TRIP and D-TRIP alloys during deep-drawing process based on the analysis of synchrotron x-ray diffraction patterns, in Figure 4.5. The metastable austenite phase in TRIP alloy partially transfers into  $\epsilon$ -martensite and  $\alpha'$ -martensite phases during deep-drawing process, leading to the microstructure consisting of retained austenite phase,  $\epsilon$ -martensite phase, and  $\alpha'$ -martensite phase. On the other hand, D-TRIP alloy initially consists of metastable austenite phase and ferrite phase, and when this alloy is processed by deep drawing operation, the microstructure of deep-drawn D-TRIP alloy has retained austenite phase, ferrite phase, and  $\alpha'$ -martensite phase due to martensitic phase transformation during deep-drawing process. In the literatures [17, 26, 95, 96], martensite phases resulted from martensitic phase transformation can influence the phase-specific stresses during deformation and lead to the stress concentration in phase scale in TRIP steel alloys. However, it has been reported that the strain-induced  $\epsilon$ -martensite phase would not sustain the substantial load as it is processed during deformation, while the strain-induced  $\alpha'$ -martensite phase has significant effect on the load partitioning between austenite phase and  $\alpha'$ -martensite phase [17]. In the current study, the analysis of diffraction pattern as shown in Figure 4.5a shows that the amount of strain-induced  $\epsilon$ -martensite phase, which is believed to form at shear band intersections and

provide nucleation sites for  $\alpha'$ -martensite phase [25], is limited in deep-drawn TRIP alloy because of limit intensities in peaks in strain-induced  $\epsilon$ -martensite phase. Therefore, the effect of strain-induced  $\epsilon$ -martensite phase on phase-specific stress partitioning is not considered as a key factor responsible for the residual stress concentration in deep-drawn TRIP alloy. As shown in Figure 4.10a and Figure 4.11a, the deep-drawn TRIP alloy exhibits the residual stress partitioning behavior, which is mainly caused by strain-induced  $\alpha'$ -martensite phase. The results show that residual stresses concentrate in the strain-induced  $\alpha'$ -martensite phase other than austenite phase at same position in deep-drawn TRIP alloy based on the analysis of synchrotron x-ray diffraction data. Comparison of hoop and axial residual stresses in austenite phase for deep-drawn TRIP and A-SS alloys shows a decrease of hoop and axial residual stresses in deep-drawn TRIP alloy compared to in deep-drawn A-SS alloy at same position. It indicates that the applied stresses could transfer from austenite phase to strain-induced  $\alpha'$ -martensite phase during deep-drawing process, resulting in the decrease of residual stresses in austenite phase in deep-drawn TRIP alloy, but the residual stress concentration in strain-induced  $\alpha'$ -martensite phase. Furthermore, the macroscopic hoop and axial residual stresses located at outside surface of tip of deep-drawn cup wall are tensile stresses as illustrated in Figure 4.10b and Figure 4.11b, resulting from the complex strain path imported by deep-drawing process. Hence, it is likely that the martensitic phase transformation associated with deep-drawing processing play significant role on stress distribution in deep-drawn TRIP

alloy in terms of macroscopic stress and phase-specific stress, leading to the tensile stresses concentrate in the strain-induced  $\alpha'$ -martensite phase at outside surface. It should be noted that the cracks observed in deep-drawn TRIP alloy initiated from outside surface of tip and were all vertically propagating, indicating that stress concentration in hoop direction at tip of deep-drawn cup wall could be the critical factor contributing to the cracking phenomenon. In such case, as shown in Figure 4.10a, the strain-induced  $\alpha'$ -martensite phase located at outside of tip of deep-drawn TRIP cup wall has the highest tensile residual stress, which would result in the cracking phenomenon. In addition, the austenite phase shows the corresponding decrease of hoop residual stress in deep-drawn TRIP alloy as compared to that in deep-drawn A-SS alloy, indicating that the role of ductile austenite phase on the resistance to cracking is significantly suppressed by the stress partitioning among constituent phases caused by the martensitic phase transformation in TRIP alloy. It is believed that this suppression in austenite phase would be another contribution lowering the resistance to cracking in deep-drawn TRIP alloy.

On the other hand, for the deep-drawn D-TRIP alloy, when the D-TRIP alloy is processed by deep-drawing operation, the phase-specific stress partitioning behavior can be caused not only by strain-induced  $\alpha'$ -martensite phase but also by the ferrite phase. Figure 4.10d and Figure 4.11d also illustrate the effect of ferrite phase on changes in phase-specific residual stress in deep-drawn D-SS alloy, resulting in the increase in residual stress in ferrite phase. However, the hoop

and axial residual stresses in austenite phase do not significantly decrease in deep-drawn D-SS alloy when we compare the residual stresses in austenite phase at hoop and axial directions for deep-drawn D-SS and A-SS alloys. Moreover, based on the consideration for cracking phenomenon as describe earlier, the critical hoop residual stress shows even higher value in austenite phase located at outside surface of tip of deep-drawn D-SS cup wall than that of deep-drawn A-SS cup wall, showing that the austenite phase in deep-drawn TRIP alloy has a considerable portion of residual stresses. Those results indicate that the contribution of austenite phase on resistance to cracking in deep-drawn D-SS alloy is not significantly suppressed by the stress partitioning between austenite phase and ferrite phase. It is believed to be caused by the unique micromechanical mechanism regarding to the stress partitioning between austenite phase and ferrite phase [35, 36]. According to our prior study of lattice strain evolution during tensile loading using in-situ neutron diffraction in Chapter 3 and literature [36], the applied stresses initially transferred from soft austenite phase to hard ferrite phase when plastic flow initiates in D-SS alloy, and as increasing of applied stress, the hard ferrite phase firstly yields, resulting in the load transferring back to hardened austenite phase. As a result, the hardening austenite phase continues to deform to sustain the increase of applied stress as increasing strains. Furthermore, the changes in stress in austenite phase also strongly affect the martensitic phase transformation kinetics, which, in turn, would interact with constituent phases to change the stress partitioning behavior in D-TRIP alloy during deep-drawing



process [26]. In such case, the austenite phase in D-TRIP alloy is expected to deform with the reduction of stress due to the ferrite phase maintains a portion of applied stress during deep-drawing process, resulting in the decrease of phase transformation rate and strain-induced  $\alpha'$ -martensite phase fraction, in Figure 4.6. Also, it has been reported that the fracture behavior is significantly correlated to the strain-induced  $\alpha'$ -martensite phase fraction as the higher amount of strain-induced  $\alpha'$ -martensite phase would have strong potential to develop the network consisting of brittle  $\alpha'$ -martensite phase providing the propagation of cracks [20]. Therefore, the lower amount of strain-induced  $\alpha'$ -martensite phase generated in deep-drawn D-TRIP alloy, as shown in Figure 4.6, is believed to contribute on the good resistance to cracking. Furthermore, as compared of hoop residual stress for deep-drawn D-TRIP and D-SS alloys, the hoop residual stresses in bcc phases was observed to be higher in deep-drawn D-TRIP alloy. It is believed to be caused by the strain-induced  $\alpha'$ -martensite phase ascribing to the effect of martensitic phase transformation on the stress partitioning behavior, as bcc peaks in synchrotron x-ray diffraction patterns, in Figure 4.5c, were generated from ferrite phase and strain-induced  $\alpha'$ -martensite phase. In such case, the residual stresses in bcc phases in deep-drawn D-TRIP alloy would be particularly partitioned between bcc ferrite phase and strain-induced bcc  $\alpha'$ -martensite phase. As a result, such local stress partitioning between bcc phases in deep-drawn D-TRIP alloy could allow the ductile ferrite phase to maintain a portion of tensile residual stresses and thereby provide contributions on decreasing the tensile stress

concentration in strain-induced  $\alpha'$ -martensite phase. Therefore, although the strain-induced  $\alpha'$ -martensite phase shows hoop residual stress concentration at outside surface of tip of deep-drawn D-TRIP alloy, the changes in martensitic phase transformation kinetics and stress partitioning behavior affected by ferrite phase could lead to decrease the amount of strain-induced  $\alpha'$ -martensite phase and release the tensile stress concentration in strain-induced  $\alpha'$ -martensite phase, resulting in the good resistance to cracking in D-TRIP alloy.

#### ***4.4.2 Texture evolution and its effect on the martensitic phase transformation and plastic anisotropy in deep-drawn stainless steel alloys***

It has been presented in Figure 4.4 that the cracking phenomenon in deep-drawn TRIP alloy shows changes in propagation rate varying from RD to TD, demonstrating the orientation-dependent behavior in the cracking phenomenon. As discussed earlier in section 4.4.1, it is believed that the amount of strain-induced  $\alpha'$ -martensite phase distributing nonuniformly from RD to TD, in Figure 4.6, could be closely related to the orientation-dependent behavior of cracking in deep-drawn TRIP alloy. It also has been confirmed that the changes in cracking rate and strain-induced  $\alpha'$ -martensite phase fraction in deep-drawn TRIP alloy show the same trend when we compare results of Figure 4.4 and Figure 4.6. It has been well known that the changes in martensitic phase transformation kinetics following crystallographic variant selection are also controlled by the texture in parent austenite phase, thus resulting in the difference in amount of strain-induced  $\alpha'$ -martensite phase [37]. Furthermore, according to the literature [123], the

circumferential compression with straining direction paralleling to hoop direction is predominately acting on the sheet flange during deep-drawing process. Thus, as shown in Figure 4.7, the  $\langle 110 \rangle$  fibers paralleling to hoop direction in austenite phase, such as A  $\{011\}\langle 111 \rangle$  and Rotated-Goss  $\{110\}\langle 011 \rangle$  components, has been developed in all deep-drawn stainless steel alloys. It also illustrates that the constrained effect of ferrite phase on the development in texture in austenite phase is not significant during deep-drawing process in D-TRIP and D-SS alloys. In the current study, the crystallographic texture analysis for austenite phase shows that the textures in austenite phase have weaker  $\langle 100 \rangle$  components paralleling to the hoop direction in deep-drawn TRIP and D-TRIP alloys as compared to that in deep-drawn A-SS and D-SS alloys. In order to clearly analyze the effect of martensitic phase transformation on texture evolution in austenite phase and in corresponding strain-induced  $\alpha'$ -martensite phase, the inverse pole figures along with the hoop direction in strain-induced  $\alpha'$ -martensite phase and austenite phase at RD in deep-drawn TRIP alloy are presented in Figure 4.12. Figure 4.12a shows that texture in strain-induced  $\alpha'$ -martensite phase shows higher texture intensity in  $\langle 100 \rangle$  component while lower texture intensity in  $\langle 111 \rangle$  component, which, however, does not show an agreement with the typical texture of bcc steel alloy subjected to uniaxial compression [118]. Accordingly, the texture in austenite phase does not show the  $\langle 100 \rangle$  component in inverse pole figure, in Figure 4.12b, which again is consistent with the comparison of pole figures in austenite phase for deep-drawn TRIP and A-SS alloys. According to the Bain model used for studying the

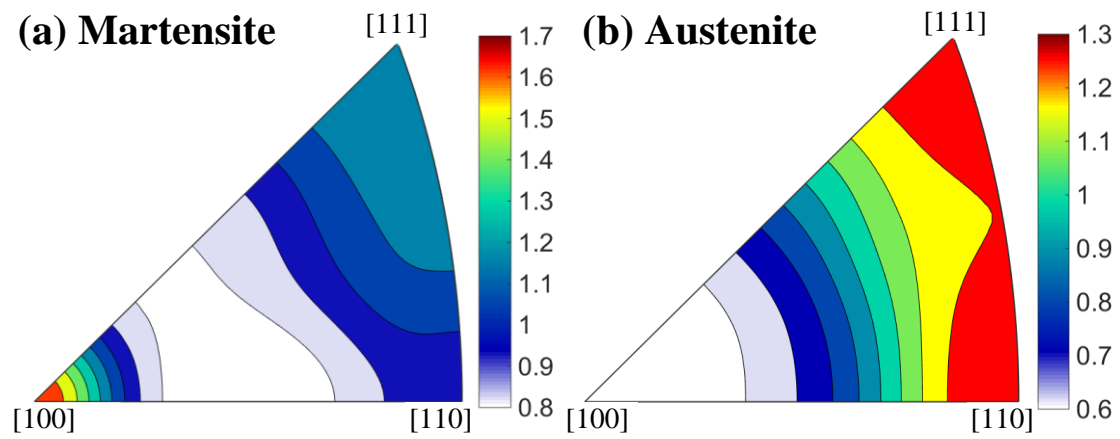


Figure 4.12. Inverse pole figures along the hoop direction in deep-drawn TRIP alloy (DR = 2.0) showing the deformation textures in the strain-induced  $\alpha'$ -martensite phase and the austenite phase.

crystallographic orientation correlation between austenite phase and strain-induced  $\alpha'$ -martensite phase [124], it is likely that the martensitic phase transformation in TRIP and D-TRIP alloys prefers to take place in the (100) austenite grains when the hoop direction is parallel to the normal of (100) plane in austenite grains during deep-drawing process, resulting in the increase in texture intensity of  $\langle 100 \rangle$  component in strain-induced  $\alpha'$ -martensite phase while accordingly decreasing that in austenite phase. In this case, therefore, the initial texture intensities of (100) austenite grains that would be the resource promoting the martensitic phase transformation can be used to estimate the relative amount of strain-induced  $\alpha'$ -martensite phase distributing from RD to TD in deep-drawn TRIP and D-TRIP alloys. Thus, the comparison of amount of strain-induced  $\alpha'$ -martensite phase in deep-drawn cups and initial texture intensity in (100) austenite grains along hoop direction in alloy plates are presented from RD to TD in Figure 4.13. This comparison shows that the changes in strain-induced  $\alpha'$ -martensite phase fraction and (100) texture intensity in austenite phase have same trend in TRIP alloy, indicating the significant contribution of initial texture in austenite phase on the change in amount of strain-induced  $\alpha'$ -martensite phase fraction in deep-drawn TRIP alloy, and thus orientation-dependent cracking behavior. Nevertheless, the initial texture intensity in (100) austenite phase increases from RD to TD in D-TRIP alloy, which shows the different trend as the change in the amount of strain-induced  $\alpha'$ -martensite phase. It indicates that the anisotropic behavior in terms of strain-induced  $\alpha'$ -martensite phase fraction in deep-drawn D-

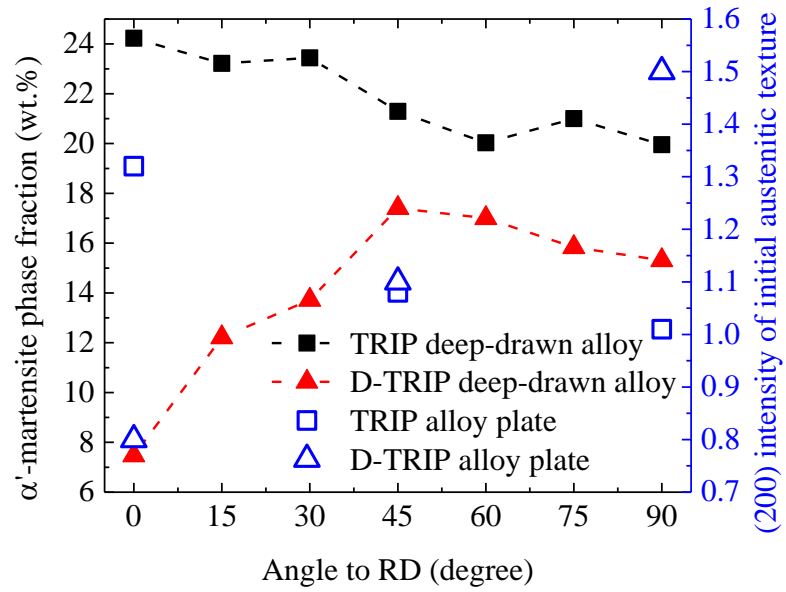


Figure 4.13. A comparison between the strain-induced  $\alpha'$ -martensite phase fraction measured in deep-drawn TRIP and D-TRIP alloys and the initial (200) texture intensity in austenite phase in the as-received TRIP and D-TRIP alloy plates.

TRIP alloy could be not only affected by initial texture in austenite phase. In the literature [35], it has been reported that the initial texture in ferrite phase plays a significant role in the plastic anisotropy in cold-rolled duplex stainless steel alloys due to the lamellar ferrite phase develops the strong initial texture. In the current study, it was presented in Figure 4.9 that the texture intensity in ferrite phase varies significantly from RD to TD in deep-drawn D-TRIP alloy, which could have a strong contribution on the plastic anisotropy. In this case, therefore, the applied stresses influenced by the plastic anisotropy in D-TRIP alloy could vary in ferrite phase and correspondingly in austenite phase from RD to TD during deep-drawing process, resulting in the changes in martensitic phase transformation kinetics. For example, according to Moverare et al. [103], the cold-rolled duplex stainless steel alloy exhibits the lower tensile strength when the straining direction is along with the  $45^\circ$  with respect to RD. Also, our prior study in Chapter 3 showed that the stresses in ferrite phase decrease when the specimen is stretching along  $45^\circ$  respect with RD due to corresponding ferrite grains show higher Schmid factors. This corresponds to an increase in stresses in austenite phase at  $45^\circ$  respect with RD, leading to the increase in amount of strain-induced  $\alpha'$ -martensite phase at this direction. Therefore, in the current study, the underestimation in the strain-induced  $\alpha'$ -martensite phase fraction using the initial texture intensity in (100) austenite grains in deep-drawn D-TRIP alloy could be compensated by the plastic anisotropy mainly caused by the texture in ferrite phase. As discussed earlier in this section, it is expected that the crystallographic textures in austenite phase as well as ferrite

phase have the contribution on the inhomogeneous distribution in strain-induced  $\alpha'$ -martensite phase fraction in deep-drawn D-TRIP alloy. Also, this current study illustrates that the deep-drawn D-TRIP alloy would show the cracking phenomenon as the drawing ratio increases due to the hoop residual stress concentration in strain-induced  $\alpha'$ -martensite phase, and the crack is believed to initiate at  $45^\circ$  respect to RD because of the higher amount of strain-induced  $\alpha'$ -martensite phase.

## 4.5 Conclusions

In this chapter, the correlation of phase-specific residual stress partitioning behavior, martensitic phase transformation, constituent phases, and crystallographic texture was systematically studied to understand the mechanisms responsible for the cracking behavior and formability of TRIP-assisted stainless steel (SS) alloys during deep-drawing process at ambient temperature. Four stainless steel alloys, i.e. (1) a TRIP SS (TRIP alloy), (2) a stable austenitic SS (A-SS alloy) (stable counterpart of (1)), (3) a lean duplex TRIP SS (D-TRIP alloy), and (4) a lean duplex stable SS (D-SS alloy) (stable counterpart of (3)), were processed using deep-drawing operation. The microstructure and texture developed in deep-drawn SS alloys were characterized using high-energy synchrotron x-ray diffraction (S-XRD) technique. Furthermore, the phase-specific residual stresses in deep-drawn SS alloys were mapped using S-XRD as a function of deep-drawn cup wall height and thickness. The conclusions are as follows:



1. The cracking phenomenon was observed in the deep-drawn TRIP alloy with 1.9, 2.0, and 2.1 drawing ratios whereas the deep-drawn D-TRIP alloy showed a good resistance to cracking. It was also shown that the deep-drawn TRIP alloy with 2.1 drawing ratio has a change in cracking rate from rolling direction to transverse direction, suggesting an orientation-dependent cracking behavior.

2. The analysis of synchrotron x-ray diffraction patterns showed that the martensitic phase transformation happened in TRIP and D-TRIP alloys during deep-drawing process, resulting in the microstructure consisting of retained austenite phase and strain-induced  $\epsilon$ - and  $\alpha'$ -martensite phase in deep-drawn TRIP alloy while the microstructure consisting of initial ferrite phase, retained austenite phase, and strain-induced  $\alpha'$ -martensite phase in deep-drawn D-TRIP alloy. The deep-drawn TRIP alloy had the higher average amount of strain-induced  $\alpha'$ -martensite phase at outside surface of tip of deep-drawn cup wall compared to deep-drawn D-TRIP alloy. Comparison of the strain-induced  $\alpha'$ -martensite phase fraction for deep-drawn TRIP and D-TRIP alloys showed different trends from rolling direction to transverse direction.

3. The phase-specific stress partitioning behavior revealed that the hoop residual stresses concentrated in strain-induced  $\alpha'$ -martensite phase in deep-drawn TRIP and D-TRIP alloys. For the deep-drawn TRIP alloy, the effect of ductile austenite phase on the resistance to cracking is significantly reduced as the decrease in hoop residual stress in austenite phase in deep-drawn TRIP alloy compared to that in deep-drawn A-SS alloy. Thus, the phase-specific stress partitioning behavior

caused by martensitic phase transformation could be responsible to the cracking phenomenon in deep-drawn TRIP alloy. However, for the deep-drawn D-TRIP alloy, the hoop residual stresses in bcc phases were partitioned between ductile ferrite phase and strain-induced  $\alpha'$ -martensite phase and it could result in the reduction in hoop stress concentration in strain-induced  $\alpha'$ -martensite phase. Moreover, the stress partitioning between austenite phase, ferrite phase, and strain-induced  $\alpha'$ -martensite phase did not prohibit the contribution of ductile austenite phase on the resistance to cracking in deep-drawn D-TRIP alloy. Therefore, the phase-specific stress partitioning behavior and its effect on the stress concentration are corresponded to the difference in formability for TRIP and D-TRIP alloys in terms of cracking phenomenon.

4. The texture in austenite phase showed  $\langle 100 \rangle$  fiber along the hoop direction and the texture in ferrite and strain-induced  $\alpha'$ -martensite phases had  $\langle 111 \rangle$  and  $\langle 100 \rangle$  fibers along the hoop direction in all deep-drawn SS alloys due to the sheet flange was predominately subjected to circumferential compression along hoop direction. As compared of texture component in austenite phase for deep-drawn TRIP and D-TRIP alloys and their stable counterparts, it was shown that the martensitic phase transformation was favored to occur on (100) austenite grains along the hoop direction. Thus, the initial texture in austenite phase that is strongly related to martensitic phase transformation kinetics resulted the changes in the amount of strain-induced  $\alpha'$ -martensite phase in deep-drawn TRIP and D-TRIP alloys. It corresponds to the orientation-dependent cracking behavior in deep-

drawn TRIP alloy. Furthermore, the changes in texture intensity in ferrite phase from rolling direction to transverse direction illustrated the effect of texture in ferrite phase on the plastic anisotropy in D-TRIP alloy. Thus, the texture in ferrite phase could be considered to another factor contributing on the inhomogeneous distribution in the amount of strain-induced  $\alpha'$ -martensite phase in deep-drawn D-TRIP alloy.

Overall, the martensitic phase transformation results in significant stress concentration in strain-induced  $\alpha'$ -martensite phase due to the phase-specific stress partitioning between constituent phases in TRIP alloy, making it susceptible to the cracking phenomenon during deep-drawing process at ambient temperature. However, the phase-specific stress partitioning behavior optimized by the ferrite phase in D-TRIP alloy could reduce the stress concentration in strain-induced  $\alpha'$ -martensite phase, leading to a good resistance to cracking. Furthermore, the textures in austenite phase and ferrite phase are responsible for the change in martensitic phase transformation kinetics, resulting in the inhomogeneous distribution of strain-induced  $\alpha'$ -martensite phase fraction in deep-drawn TRIP and D-TRIP alloys and the orientation-dependent cracking behavior in deep-drawn TRIP alloy. Therefore, this work provides the possibilities to improve the formability of high-strength TRIP-assisted steel alloys by controlling the constituent phases and their texture.

## CHAPTER 5 Summary and Conclusions

In the current study, the interplay of martensitic phase transformation, constituent phases, and crystallographic texture during uniaxial tension and deep-drawing process and its effect on the cracking phenomenon of TRIP-assisted steel alloys were studied through connecting microstructure to the phase-specific stress partitioning behavior. Four stainless steel (SS) alloys were studied during tensile loading and deep-drawing process at ambient temperature: (1) a TRIP SS, (2) a stable austenitic SS (stable counterpart of (1)), (3) a lean duplex TRIP SS, and (4) a lean duplex stable SS (stable counterpart of (3)). The microstructure and texture evolutions in tensile specimens and deep-drawn cups were studied using high-energy synchrotron x-ray diffraction. The in-situ neutron diffraction was also used to understand the phase-specific stress partitioning behavior by analyzing the lattice strain evolution during uniaxial tensile loading. Furthermore, the phase-specific residual stresses in deep-drawn cups were measured using high-energy synchrotron x-ray diffraction as a function of cup wall height and thickness. Detailed conclusions are as follows:

1. In the study of SS alloy plates, the TRIP alloy exhibits higher tensile strength and ductility as compared to D-TRIP alloy. The plastic anisotropy is more pronounced in D-TRIP alloy compared to the TRIP alloy based on the analysis of the Lankford coefficient. In the study of deep-drawn SS alloy cups, the cracking phenomenon was only observed in deep-drawn TRIP alloy, suggesting that the D-TRIP alloy has a better resistance to cracking and formability during deep-drawing

process compared to the TRIP alloy. It is also shown that the cracking behavior in deep-drawn TRIP alloy is orientation-dependent because of the changes in cracking rate from RD to TD.

2. The analysis of synchrotron x-ray diffraction patterns shows that the TRIP alloy develops higher average amount of strain-induced  $\alpha'$ -martensite phase compared to D-TRIP alloy during tensile loading and deep-drawing process. Furthermore, although the strain-induced  $\alpha'$ -martensite phase fraction does not show significant anisotropic behavior in the TRIP and D-TRIP alloys during tensile loading, it is more pronounced in the deep-drawn cups of TRIP and D-TRIP alloys. The amount of strain-induced  $\alpha'$ -martensite phase decrease almost linearly from RD to TD in deep-drawn TRIP alloy, while it increases from RD to  $45^\circ$  and then slightly decrease from  $45^\circ$  to TD in the deep-drawn D-TRIP alloy.

3. The stress partitioning behavior was investigated during uniaxial tension and deep-drawing process. The results show that the effect of strain-induced  $\varepsilon$ -martensite phase on stress partitioning in the TRIP SS is not significant. On the other hand, the strain-induced  $\alpha'$ -martensite phase plays an important role in the stress partitioning during plastic deformation in that the applied stress is transferred into strain-induced  $\alpha'$ -martensite phase, resulting in the residual stress concentration in this martensite phase in both the TRIP and D-TRIP SS alloys. However it is found that the residual stress in strain-induced  $\alpha'$ -martensite phase in the D-TRIP alloy is reduced as compared to the TRIP alloy, which is ascribed to the local force balance between ferrite phase and strain-induced  $\alpha'$ -martensite

phase in the D-TRIP alloy, resulting from the load sharing of the ferrite phase. Moreover, the phase-specific stress partitioning between austenite phase, ferrite phase, and strain-induced  $\alpha'$ -martensite phase does not prohibit the contribution of ductile austenite phase on the resistance to cracking in D-TRIP alloy as the stress in austenite phase in D-TRIP alloy is comparable to that in the single-phase A-SS alloy. The stress partitioning behavior modified by ferrite phase could also result in the decrease of stress in austenite phase in D-TRIP alloy, leading to a lower strain-induced  $\alpha'$ -martensite phase fraction, which could further contribute to the improved resistance to cracking in the D-TRIP alloy.

4. The effect of crystallographic texture on the plastic anisotropy and martensitic phase transformation kinetics was studied during tensile loading and deep-drawing process. The analysis on texture evolution shows that the effect of texture in austenite phase on the plastic anisotropy is limited due to the comparable textures and their intensities for both TRIP and D-TRIP alloys. However, comparison of texture in the austenite phase in deep-drawn TRIP and D-TRIP alloys shows that martensitic phase transformation is favored to occur on (100) austenite grains along hoop direction, which is consistent with the description in Bain model. Thus, the initial texture in austenite phase, specially the (100) texture intensity, could affect the martensitic phase transformation, and it is responsible for the changes in strain-induced  $\alpha'$ -martensite phase distributing in deep-drawn cup wall tip from RD to TD in both TRIP and D-TRIP alloys. On the other hand, the significant difference in texture intensity in ferrite phase from RD to TD in D-TRIP alloy

indicates that the initial texture in ferrite phase is responsible for the plastic anisotropy, which could be another factor contributing to the inhomogeneous distribution of strain-induced  $\alpha'$ -martensite phase fraction in deep-drawn D-TRIP alloy. As a result, the inhomogeneous distribution of strain-induced  $\alpha'$ -martensite phase fraction could correspond to the orientation-dependent cracking behavior, which shows the same trend as the changes in strain-induced  $\alpha'$ -martensite phase fraction from RD to TD in the deep-drawn TRIP alloy.

## LIST OF REFERENCES

- [1] A. Ghosh, The influence of strain hardening and strain-rate sensitivity on sheet metal forming, (1977).
- [2] A. Korbel, P. Martin, Microstructural events of macroscopic strain localization in prestrained tensile specimens, *Acta Metallurgica* 36(9) (1988) 2575-2586.
- [3] F. Ozturk, D. Lee, Experimental and numerical analysis of out-of-plane formability test, *Journal of Materials Processing Technology* 170(1-2) (2005) 247-253.
- [4] J. Poirier, Shear localization and shear instability in materials in the ductile field, *Journal of Structural Geology* 2(1-2) (1980) 135-142.
- [5] R. Stringfellow, D. Parks, G.B. Olson, A constitutive model for transformation plasticity accompanying strain-induced martensitic transformations in metastable austenitic steels, *Acta metallurgica et materialia* 40(7) (1992) 1703-1716.
- [6] S.P. Keeler, Determination of forming limits in automotive stampings, SAE Technical Paper, 1965.
- [7] G.M. Goodwin, Application of strain analysis to sheet metal forming problems in the press shop, *SAE Transactions* (1968) 380-387.
- [8] S.S. Hecker, Simple technique for determining forming limit curves, *Sheet Metal Industries* 52(11) (1975) 671-676.
- [9] M. Azrin, W.A. Backofen, The deformation and failure of a biaxially stretched sheet, *Metallurgical Transactions* 1(10) (1970) 2857-2865.



- [10] R.W. Imlay, Correlation of the Jurassic formations of North America, exclusive of Canada, Geological Society of America Bulletin 63(9) (1952) 953-992.
- [11] T.B. Stoughton, A general forming limit criterion for sheet metal forming, International Journal of Mechanical Sciences 42(1) (2000) 1-27.
- [12] S. Kim, H. Huh, H. Bok, M. Moon, Forming limit diagram of auto-body steel sheets for high-speed sheet metal forming, Journal of Materials Processing Technology 211(5) (2011) 851-862.
- [13] K. Bandyopadhyay, S. Basak, S. Panda, P. Saha, Use of stress based forming limit diagram to predict formability in two-stage forming of tailor welded blanks, Materials & Design 67 (2015) 558-570.
- [14] N. Park, H. Huh, S.J. Lim, Y. Lou, Y.S. Kang, M.H. Seo, Fracture-based forming limit criteria for anisotropic materials in sheet metal forming, International Journal of Plasticity 96 (2017) 1-35.
- [15] A.K. Srivastava, G. Jha, N. Gope, S. Singh, Effect of heat treatment on microstructure and mechanical properties of cold rolled C–Mn–Si TRIP-aided steel, Materials Characterization 57(2) (2006) 127-135.
- [16] E. Cakmak, H. Choo, K. An, Y. Ren, A synchrotron X-ray diffraction study on the phase transformation kinetics and texture evolution of a TRIP steel subjected to torsional loading, Acta Materialia 60(19) (2012) 6703-6713.

- [17] K. Tao, H. Choo, H. Li, B. Clausen, J.-E. Jin, Y.-K. Lee, Transformation-induced plasticity in an ultrafine-grained steel: An in situ neutron diffraction study, *Applied Physics Letters* 90(10) (2007) 101911.
- [18] K. Tao, D.W. Brown, S.C. Vogel, H. Choo, Texture evolution during strain-induced martensitic phase transformation in 304L stainless steel at a cryogenic temperature, *Metallurgical and Materials Transactions A* 37(12) (2006) 3469-3475.
- [19] E. Cakmak, S.C. Vogel, H. Choo, Effect of martensitic phase transformation on the hardening behavior and texture evolution in a 304L stainless steel under compression at liquid nitrogen temperature, *Materials Science and Engineering: A* 589 (2014) 235-241.
- [20] P. Jacques, Q. Furnemont, T. Pardoen, F. Delannay, On the role of martensitic transformation on damage and cracking resistance in TRIP-assisted multiphase steels, *Acta materialia* 49(1) (2001) 139-152.
- [21] M.R. Berrahmoune, S. Berveiller, K. Inal, E. Patoor, Delayed cracking in 301LN austenitic steel after deep drawing: Martensitic transformation and residual stress analysis, *Materials Science and Engineering a-Structural Materials Properties Microstructure and Processing* 438 (2006) 262-266.
- [22] S. Papula, J. Talonen, H. Hänninen, Effect of residual stress and strain-induced  $\alpha'$ -martensite on delayed cracking of metastable austenitic stainless steels, *Metallurgical and Materials Transactions A* 45(3) (2014) 1238-1246.

- [23] J. Kim, S. Hong, N. Anjabin, B. Park, S. Kim, K.-G. Chin, S. Lee, H. Kim, Dynamic strain aging of twinning-induced plasticity (TWIP) steel in tensile testing and deep drawing, *Materials Science and Engineering: A* 633 (2015) 136-143.
- [24] M. Daymond, C. Tomé, M. Bourke, Measured and predicted intergranular strains in textured austenitic steel, *Acta materialia* 48(2) (2000) 553-564.
- [25] G. Olson, M. Cohen, Kinetics of strain-induced martensitic nucleation, *Metallurgical transactions A* 6(4) (1975) 791.
- [26] X. Wu, M. Yang, F. Yuan, L. Chen, Y. Zhu, Combining gradient structure and TRIP effect to produce austenite stainless steel with high strength and ductility, *Acta Materialia* 112 (2016) 337-346.
- [27] S. Hong, J. Lee, S. Lee, W. Woo, S.-K. Kim, H.S. Kim, Residual stress analysis in deep drawn twinning induced plasticity (TWIP) steels using neutron diffraction method, *Metallurgical and Materials Transactions A* 45(4) (2014) 1953-1961.
- [28] S. Papula, T. Sarikka, S. Anttila, J. Talonen, I. Virkkunen, H. Hänninen, Hydrogen-Induced Delayed Cracking in TRIP-Aided Lean-Alloyed Ferritic-Austenitic Stainless Steels, *Materials* 10(6) (2017) 613.
- [29] A. Zinbi, A. Bouchou, Delayed cracking in 301 austenitic steel after bending process: martensitic transformation and hydrogen embrittlement analysis, *Engineering Failure Analysis* 17(5) (2010) 1028-1037.

- [30] W.-Y. Chu, J. Yao, C.-M. Hsiao, Hydrogen induced slow crack growth in stable austenitic stainless steels, *Metallurgical Transactions A* 15(4) (1984) 729-733.
- [31] C. Briant, Hydrogen assisted cracking of type 304 stainless steel, *Metallurgical and Materials Transactions A* 10(2) (1979) 181-189.
- [32] S.J. Kim, D.W. Yun, D.W. Suh, K.Y. Kim, Electrochemical hydrogen permeation measurement through TRIP steel under loading condition of phase transition, *Electrochemistry Communications* 24 (2012) 112-115.
- [33] X. Guo, J. Post, M. Groen, W. Bleck, Stress Oriented Delayed Cracking Induced by Dynamic Martensitic Transformation in Meta-Stable Austenitic Stainless Steels, *steel research international* 82(1) (2011) 6-13.
- [34] S.H. Jung, T. Lee, S.W. Song, Y.J. Kwon, H.-G. Kang, D. Chae, C.S. Lee, Enhanced Resistance to Delayed Cracking in Deep-drawn Lean Duplex Stainless Steel: the Role of Residual Stress, *KOREAN JOURNAL OF METALS AND MATERIALS* 55(8) (2017) 544-549.
- [35] N. Jia, R.L. Peng, Y. Wang, S. Johansson, P. Liaw, Micromechanical behavior and texture evolution of duplex stainless steel studied by neutron diffraction and self-consistent modeling, *Acta Materialia* 56(4) (2008) 782-793.
- [36] N. Jia, Z. Cong, X. Sun, S. Cheng, Z. Nie, Y. Ren, P. Liaw, Y. Wang, An in situ high-energy X-ray diffraction study of micromechanical behavior of multiple phases in advanced high-strength steels, *Acta Materialia* 57(13) (2009) 3965-3977.

- [37] M. Humbert, B. Petit, B. Bolle, N. Gey, Analysis of the  $\gamma$ - $\epsilon$ - $\alpha'$  variant selection induced by 10% plastic deformation in 304 stainless steel at  $-60^{\circ}\text{C}$ , Materials Science and Engineering: A 454 (2007) 508-517.
- [38] E.C. Bain, W.E. Griffiths, An introduction to the iron-chromium-nickel alloys, Trans. AIME 75(166) (1927) 166-211.
- [39] V. Rivlin, G. Raynor, 1: Critical evaluation of constitution of chromium-iron-nickel system, International metals reviews 25(1) (1980) 21-40.
- [40] P. Marshall, Austenitic stainless steels: microstructure and mechanical properties, Springer Science & Business Media 1984.
- [41] D. Harries, Physical metallurgy of Fe-Cr-Ni austenitic steels, Mechanical behaviour and nuclear applications of stainless steel at elevated temperatures 1982.
- [42] P. Schafmeister, R. Ergang, Das Zustandsschaubild Eisen-Nickel-Zinn, Archiv für das Eisenhüttenwesen 13(2) (1939) 95-103.
- [43] R. Gunn, Duplex stainless steels: microstructure, properties and applications, Woodhead Publishing 1997.
- [44] J. Lai, A study of precipitation in AISI type 316 stainless steel, Materials Science and Engineering 58(2) (1983) 195-209.
- [45] D. Kotecki, T. Siewert, WRC-1992 constitution diagram for stainless steel weld metals: a modification of the WRC-1988 diagram, Welding Journal 71(5) (1992) 171-178.

- [46] F.A. Shunk, M. Hansen, K. Anderko, Constitution of binary alloys, McGraw-Hill 1969.
- [47] H.J. Goldschmid, Interstitial alloys, Springer 2013.
- [48] H. Solomon, L.M. Levinson, Mössbauer effect study of '475 C embrittlement' of duplex and ferritic stainless steels, *Acta Metallurgica* 26(3) (1978) 429-442.
- [49] R. Newman, E. Franz, Growth and repassivation of single corrosion pits in stainless steel, *Corrosion* 40(7) (1984) 325-330.
- [50] K.H. Lo, C.H. Shek, J. Lai, Recent developments in stainless steels, *Materials Science and Engineering: R: Reports* 65(4-6) (2009) 39-104.
- [51] A.M. Ritter, M.F. Henry, W.F. Savage, High temperature phase chemistries and solidification mode prediction in nitrogen-strengthened austenitic stainless steels, *Metallurgical Transactions A* 15(7) (1984) 1339-1351.
- [52] F. Hull, Delta ferrite and martensite formation in stainless steels, *Welding journal* 52(5) (1973) 193.
- [53] M. Onozuka, T. Saida, S. Hirai, M. Kusuhashi, I. Sato, T. Hatakeyama, Low-activation Mn–Cr austenitic stainless steel with further reduced content of long-lived radioactive elements, *Journal of Nuclear Materials* 255(2-3) (1998) 128-138.
- [54] J. Simmons, Overview: high-nitrogen alloying of stainless steels, *Materials Science and Engineering: A* 207(2) (1996) 159-169.

- [55] P. Schaaf, A. Krämer, S. Wiesen, U. Gonser, Mössbauer study of iron carbides: mixed carbides  $M_7C_3$  and  $M_{23}C_6$ , *Acta metallurgica et materialia* 42(9) (1994) 3077-3081.
- [56] Y. Lu, R. Bandy, C. Clayton, R. Newman, Surface enrichment of nitrogen during passivation of a highly resistant stainless steel, *J. Electrochem. Soc.;*(United States) 130(8) (1983).
- [57] T. Ishitsuka, Y. Inoue, H. Ogawa, Effect of silicon on the steam oxidation resistance of a 9% Cr heat resistant steel, *Oxidation of Metals* 61(1-2) (2004) 125-142.
- [58] J. Wegrzyn, A. Klimpel, The effect of alloying elements on sigma phase formation in 18-8 weld metals, *Welding journal* 60(8) (1981) 146.
- [59] Y. Jiangnan, W. Lichang, S. Wenhao, The effect of copper on the anodic dissolution behaviour of austenitic stainless steel in acidic chloride solution, *Corrosion science* 33(6) (1992) 851-859.
- [60] W. White, I. Le May, Metallographic observations on the formation and occurrence of ferrite, sigma phase, and carbides in austenitic stainless steels: Part II: Studies of AISI Type 316 Stainless Steel, *Metallography* 3(1) (1970) 51-60.
- [61] M. Wolf, Estimation method of crack susceptibility for new steel grades, 1 st European Conference on Continuous Casting., 1991, p. 2.

- [62] M. Greeff, M.d. Toit, Looking at the sensitization of 11-12% chromium EN 1.4003 stainless steels during welding, WELDING JOURNAL-NEW YORK-85(11) (2006) 243.
- [63] D.A. Porter, K.E. Easterling, M. Sherif, Phase Transformations in Metals and Alloys, (Revised Reprint), CRC press 2009.
- [64] C. Zener, Elasticity and anelasticity of metals, University of Chicago press 1948.
- [65] J. Brooks, M. Loretto, R. Smallman, Direct observations of martensite nuclei in stainless steel, Acta Metallurgica 27(12) (1979) 1839-1847.
- [66] J. Venable, The martensite transformation in stainless steel, The Philosophical Magazine: A Journal of Theoretical Experimental and Applied Physics 7(73) (1962) 35-44.
- [67] A. Kelly, N. Macmillan, Strong solids 1966, Oxford, Clarendon Press. (1971).
- [68] P. Kelly, The martensite transformation in steels with low stacking fault energy, Acta Metallurgica 13(6) (1965) 635-646.
- [69] M.J. Bierman, Y.A. Lau, A.V. Kvit, A.L. Schmitt, S. Jin, Dislocation-driven nanowire growth and Eshelby twist, Science 320(5879) (2008) 1060-1063.
- [70] A. Kumar, R.K. Khatirkar, D. Chalapathi, G. Kumar, S. Suwas, Microstructure and Texture Development during Cold Rolling in UNS S32205 and UNS S32760 Duplex Stainless Steels, Metallurgical and Materials Transactions a-Physical Metallurgy and Materials Science 48a(5) (2017) 2349-2362.



- [71] J. Talonen, H. Hänninen, Formation of shear bands and strain-induced martensite during plastic deformation of metastable austenitic stainless steels, *Acta materialia* 55(18) (2007) 6108-6118.
- [72] T. Cool, H. Bhadeshia, Prediction of martensite start temperature of power plant steels, *Materials science and technology* 12(1) (1996) 40-44.
- [73] Q. Dai, A. Wang, X. Cheng, Stacking fault energy of cryogenic austenitic steel, *Gangtie Yanjiu Xuebao*(Journal of Iron and Steel Research)(China)(China) 14 (2002) 34-37.
- [74] K.M. Bowkett, D.A. Smith, *Field-ion microscopy*, North-Holland Pub. Co.1970.
- [75] H.N. Han, C.-S. Oh, G. Kim, O. Kwon, Design method for TRIP-aided multiphase steel based on a microstructure-based modelling for transformation-induced plasticity and mechanically induced martensitic transformation, *Materials Science and Engineering: A* 499(1-2) (2009) 462-468.
- [76] S. Ganesh Sundara Raman, K. Padmanabhan, Influence of martensite formation and grain size on room temperature low cycle fatigue behaviour of AISI 304LN austenitic stainless steel, *Materials science and technology* 10(7) (1994) 614-620.
- [77] H.-S. Yang, H. Bhadeshia, Austenite grain size and the martensite-start temperature, *Scripta materialia* 60(7) (2009) 493-495.

- [78] I. Kireeva, Y.I. Chumlyakov, V. Kirillov, I. Karaman, E. Cesari, Orientation and temperature dependence of superelasticity caused by reversible  $\gamma$ - $\alpha'$  martensitic transformations in FeNiCoAlTa single crystals, *Technical Physics Letters* 37(5) (2011) 487-490.
- [79] P. Hedström, T.-S. Han, U. Lienert, J. Almer, M. Odén, Load partitioning between single bulk grains in a two-phase duplex stainless steel during tensile loading, *Acta Materialia* 58(2) (2010) 734-744.
- [80] N. Narita, C. Altstetter, H. Birnbaum, Hydrogen-related phase transformations in austenitic stainless steels, *Metallurgical Transactions A* 13(8) (1982) 1355-1365.
- [81] T. Fukuda, T. Kakeshita, K. Kindo, Effect of high magnetic field and uniaxial stress at cryogenic temperatures on phase stability of some austenitic stainless steels, *Materials Science and Engineering: A* 438 (2006) 212-217.
- [82] N. Deng, Y.P. Korkolis, Elastic anisotropy of dual-phase steels with varying martensite content, *International Journal of Solids and Structures* 141 (2018) 264-278.
- [83] Z. Cong, N. Jia, X. Sun, Y. Ren, J. Almer, Y. Wang, Stress and strain partitioning of ferrite and martensite during deformation, *Metallurgical and Materials Transactions A* 40(6) (2009) 1383-1387.
- [84] T. Angel, Formation of martensite in austenitic stainless steels, *J. Iron Steel Inst.* 177 (1954) 165-174.

- [85] Y. Tian, S. Lin, J.P. Ko, U. Lienert, A. Borgenstam, P. Hedström, Micromechanics and microstructure evolution during in situ uniaxial tensile loading of TRIP-assisted duplex stainless steels, *Materials Science and Engineering: A* 734 (2018) 281-290.
- [86] J. GREWEN, ROLLING AND ANNEALING TEXTURES IN 99.99 PER CENT ALUMINUM. PT. 2. ANNEALING TEXTURES, *METALL* (6) (1965) 604-609.
- [87] M. Atake, M. Barnett, B. Hutchinson, K. Ushioda, Warm deformation and annealing behaviour of iron–silicon–(carbon) steel sheets, *Acta Materialia* 96 (2015) 410-419.
- [88] M. Barnett, Z. Keshavarz, A. Beer, D. Atwell, Influence of grain size on the compressive deformation of wrought Mg–3Al–1Zn, *Acta materialia* 52(17) (2004) 5093-5103.
- [89] O. Grässel, L. Krüger, G. Frommeyer, L. Meyer, High strength Fe–Mn–(Al, Si) TRIP/TWIP steels development—properties—application, *International Journal of plasticity* 16(10-11) (2000) 1391-1409.
- [90] S. Papula, J. Talonen, O. Todoshchenko, H. Hänninen, Effect of internal hydrogen on delayed cracking of metastable low-nickel austenitic stainless steels, *Metallurgical and Materials Transactions A* 45(11) (2014) 5270-5279.
- [91] T. Gnaeupel-Herold, H.J. Prask, R.J. Fields, T.J. Foecke, Z.C. Xia, U. Lienert, A synchrotron study of residual stresses in a Al6022 deep drawn cup, *Materials Science and Engineering: A* 366(1) (2004) 104-113.

- [92] J.G. Kim, J.I. Yoon, S.M. Baek, M.H. Seo, W.T. Cho, K.-G. Chin, S. Lee, H.S. Kim, Residual Stress Effect on the Delayed Fracture of Twinning-Induced Plasticity Steels, *Metallurgical and Materials Transactions A* 48(6) (2017) 2692-2696.
- [93] T. Gnaeupel-Herold, T. Foecke, H.J. Prask, R.J. Fields, An investigation of springback stresses in AISI-1010 deep drawn cups, *Materials Science and Engineering: A* 399(1-2) (2005) 26-32.
- [94] N. Jia, R.L. Peng, D.W. Brown, B. Clausen, Y.D. Wang, Tensile Deformation Behavior of Duplex Stainless Steel Studied by In-Situ Time-of-Flight Neutron Diffraction, *Metallurgical and Materials Transactions a-Physical Metallurgy and Materials Science* 39a(13) (2008) 3134-3140.
- [95] Y. Tomota, H. Tokuda, Y. Adachi, M. Wakita, N. Minakawa, A. Moriai, Y. Morii, Tensile behavior of TRIP-aided multi-phase steels studied by in situ neutron diffraction, *Acta Materialia* 52(20) (2004) 5737-5745.
- [96] C. Pu, Y. Gao, Crystal plasticity analysis of stress partitioning mechanisms and their microstructural dependence in advanced steels, *Journal of Applied Mechanics* 82(3) (2015) 031003.
- [97] R. Ray, J. Jonas, Transformation textures in steels, *International Materials Reviews* 35(1) (1990) 1-36.
- [98] P. Chapellier, R. Ray, J. Jonas, Prediction of transformation textures in steels, *Acta Metallurgica et Materialia* 38(8) (1990) 1475-1490.

- [99] N. Wittridge, J. Jonas, J. Root, A dislocation-based model for variant selection during the  $\gamma$ -to- $\alpha'$  transformation, *Metallurgical and Materials Transactions A* 32(4) (2001) 889.
- [100] Y. Wang, R.L. Peng, X.-L. Wang, R. McGreevy, Grain-orientation-dependent residual stress and the effect of annealing in cold-rolled stainless steel, *Acta Materialia* 50(7) (2002) 1717-1734.
- [101] W. Hutchinson, K. Ushioda, G. Runnsjö, Anisotropy of tensile behaviour in a duplex stainless steel sheet, *Materials Science and technology* 1(9) (1985) 728-736.
- [102] J. Song, P. Bate, Plastic anisotropy in a superplastic duplex stainless steel, *Acta materialia* 45(7) (1997) 2747-2757.
- [103] J.J. Moverare, M. Oden, Influence of elastic and plastic anisotropy on the flow behavior in a duplex stainless steel, *Metallurgical and Materials Transactions A* 33(1) (2002) 57-71.
- [104] A. Hammersley, FIT2D: an introduction and overview, European Synchrotron Radiation Facility Internal Report ESRF97HA02T 68 (1997) 58.
- [105] L. Lutterotti, S. Matthies, H.-R. Wenk, A. Schultz, J. Richardson Jr, Combined texture and structure analysis of deformed limestone from time-of-flight neutron diffraction spectra, *Journal of Applied Physics* 81(2) (1997) 594-600.

- [106] H. Wenk, K. Pawlik, J. Pospiech, J. Kallend, Deconvolution of superposed pole figures by discrete ODF methods: comparison of ADC and WIMV for quartz and calcite with trigonal crystal and triclinic specimen symmetry, *Texture, Stress, and Microstructure* 22(4) (1994) 233-260.
- [107] F. Bachmann, R. Hielscher, H. Schaeben, Texture analysis with MTEX—free and open source software toolbox, *Solid State Phenomena, Trans Tech Publ*, 2010, pp. 63-68.
- [108] K. An, X. Wang, A. Stoica, *Vulcan Data Reduction and Interactive Visualization Software (VDRIVE)*, 2010.
- [109] E. Oliver, P. Withers, M. Daymond, S. Ueta, T. Mori, Neutron-diffraction study of stress-induced martensitic transformation in TRIP steel, *Applied Physics A* 74(1) (2002) s1143-s1145.
- [110] J. Foct, N. Akdut, Cleavage-like fracture of austenite in duplex stainless steel, *Scripta Metallurgica et Materialia;(United States)* 29(2) (1993).
- [111] S. Harjo, Y. Tomota, P. Lukáš, D. Neov, M. Vrana, P. Mikula, M. Ono, In situ neutron diffraction study of  $\alpha$ - $\gamma$  Fe–Cr–Ni alloys under tensile deformation, *Acta materialia* 49(13) (2001) 2471-2479.
- [112] E. Werner, Solid solution and grain size hardening of nitrogen-alloyed austenitic steels, *Materials Science and Engineering: A* 101 (1988) 93-98.
- [113] E. Kröner, Berechnung der elastischen Konstanten des Vielkristalls aus den Konstanten des Einkristalls, *Zeitschrift für Physik* 151(4) (1958) 504-518.

- [114] M.T. Hutchings, P.J. Withers, T.M. Holden, T. Lorentzen, Introduction to the characterization of residual stress by neutron diffraction, CRC press 2005.
- [115] Z. Wang, A.D. Stoica, D. Ma, A.M. Beese, Diffraction and single-crystal elastic constants of Inconel 625 at room and elevated temperatures determined by neutron diffraction, *Materials Science and Engineering: A* 674 (2016) 406-412.
- [116] R. Smallman, D. Green, The dependence of rolling texture on stacking fault energy, *Acta Metallurgica* 12(2) (1964) 145-154.
- [117] W. Charnock, J. Nutting, The effect of carbon and nickel upon the stacking-fault energy of iron, *Metal Science Journal* 1(1) (1967) 123-127.
- [118] L. Toth, J. Jonas, D. Daniel, R. Ray, Development of ferrite rolling textures in low-and extra low-carbon steels, *Metallurgical Transactions A* 21(11) (1990) 2985-3000.
- [119] C. Xie, E. Nakamachi, The effect of crystallographic textures on the formability of high-strength steel sheets, *Journal of Materials Processing Technology* 122(1) (2002) 104-111.
- [120] K. Yoshida, Y. Tadano, M. Kuroda, Improvement in formability of aluminum alloy sheet by enhancing geometrical hardening, *Computational Materials Science* 46(2) (2009) 459-468.
- [121] E. Jimenez-Melero, N. Van Dijk, L. Zhao, J. Sietsma, J. Wright, S. Van der Zwaag, In situ synchrotron study on the interplay between martensite formation, texture evolution and load partitioning in low-alloyed TRIP steels, *Materials Science and Engineering: A* 528(21) (2011) 6407-6416.

- [122] B.H. Toby, R.B. Von Dreele, GSAS-II: the genesis of a modern open-source all purpose crystallography software package, *Journal of Applied Crystallography* 46(2) (2013) 544-549.
- [123] D. Daniel, J. Savoie, J. Jonas, Textures induced by tension and deep drawing in low carbon and extra low carbon steel sheets, *Acta metallurgica et materialia* 41(6) (1993) 1905-1920.
- [124] E.C. Bain, N. Dunkirk, The nature of martensite, *trans. AIME* 70(1) (1924) 25-47.



## **VITA**

Peijun Hou was born in Dalian, China, on January 30, 1986. He received a Bachelor of Science degree from the Department of Civil Engineering at Dalian University of Technology in China in 2009. From 2011 to 2014, he enrolled in the master program at the Department of Engineering Mechanics at Dalian University of Technology in Dalian, China, and he earned his Master of Science degree in 2014. In August 2014, he joined Professor Hahn Choo's group in the Department of Materials Science and Engineering at the University of Tennessee, Knoxville.